COUPLING FLUORESCENT MOLECULES TO NANOPHOTONIC STRUCTURES

A DISSERTATION

SUBMITTED TO THE DEPARTMENT OF APPLIED PHYSICS

AND THE COMMITTEE ON GRADUATE STUDIES

OF STANFORD UNIVERSITY

IN PARTIAL FULFILLMENT OF THE REQUIREMENTS

FOR THE DEGREE OF

DOCTOR OF PHILOSOPHY

Anika Amir Kinkhabwala

June 2010

I certify that I have read this dissertation and that, in my opinion, it is fully adequate in scope and quality as a dissertation for the degree of Doctor of Philosophy.

William Moerner, Primary Adviser

I certify that I have read this dissertation and that, in my opinion, it is fully adequate in scope and quality as a dissertation for the degree of Doctor of Philosophy.

Mark Brongersma

I certify that I have read this dissertation and that, in my opinion, it is fully adequate in scope and quality as a dissertation for the degree of Doctor of Philosophy.

Gordon Kino

Approved for the Stanford University Committee on Graduate Studies.

Patricia J. Gumport, Vice Provost Graduate Education

This signature page was generated electronically upon submission of this dissertation in electronic format. An original signed hard copy of the signature page is on file in University Archives.

Abstract

Fluorescence imaging and spectroscopy is an important tool in many areas of research. Biology has particularly benefitted from fluorescence techniques, since a single molecule's position, local environment, and even activity can be studied in real time by tagging it with a fluorescent label. It is, therefore, important to be able to understand and manipulate fluorescence. One way to control fluorescence is to shape the local electromagnetic fields that excite the fluorescent molecule. This thesis studies the interaction between fluorescent molecules and two nanophotonic structures that highly modify local electromagnetic fields: the bowtie nanoantenna and the photonic crystal cavity.

The study of plasmons, or coherent excitations of free electrons in a metal, has led to the fabrication of antennas at optical frequencies. In particular, gold bowtie nanoantennas have been shown to concentrate light from the diffraction limit at 800 nm (~300 nm) down to ~20 nm, while also enhancing the local electric field intensity by a factor of 1,000. This huge change in the local field greatly alters the absorption and fluorescence emission of nearby molecules. This thesis will show that the fluorescence from an initially-poor single-molecule emitter can be enhanced by a factor of 1,300, allowing for the measurement of one highly enhanced molecule over a background of 1,000 unenhanced molecules. By extending this experiment to

molecules in solution, dynamics of single molecules in concentrated solutions can also be measured.

While bowtie nanoantennas act to concentrate light, light does not remain in the structure for long. The photonic crystal cavity can be used to trap and store light, which has interesting implications for molecular emitters located nearby. This thesis will show that molecules can be lithographically positioned onto a photonic crystal cavity and that the molecule's fluorescence emission is coupled to the cavity modes.

Acknowledgements

The research in this thesis was aided by a great many people. First and foremost, I must acknowledge my advisor Prof. W. E. Moerner. W. E. has not only made funding possible to support me throughout my graduate career, but has more importantly been a steady guide in my research efforts. My projects needed a long time to mature and he was always there to encourage me and provide helpful ideas at the most frustrating times. In addition, he has been an excellent role model as a scientist – someone who always makes sure the science is correct and complete as possible before publishing it. I'd also like to thank the rest of my reading committee. First, Prof. Gordon Kino who actually originally began the bowtie project in the infrared region of the spectrum and was a very helpful collaborator early in my graduate career. Prof. Mark Brongersma, the final reader on my committee, is an expert in the area of plasmonics and taught an excellent class early in my career as a graduate student. This class fostered my early love of plasmonics.

My graduate career began in the Moerner lab under the guidance of Dr. Dave Fromm, who taught me the basics of plasmonics and optical microscopy, knowledge that significantly aided my early development as a scientist. Dr. Jim Schuck, a postdoc when I joined the lab, also guided me and has even been a helpful resource after finishing his work in the Moerner lab and moving on to LBNL. The last member of the early bowtie team was Arvind Sundaramurthy, who taught me a great

deal about nanofabrication of bowtie nanoantennas. Frank Jäckel later joined the bowtie team and I very much appreciated his help and guidance through the middle portion of my graduate career.

I have had a number of collaborators throughout my time at Stanford. The most important collaborators for the work contained in this thesis are Dr. Zongfu Yu of Prof. Shanhui Fan's lab, Kelley Rivoire of Prof. Jelena Vuckovic's lab, and Dr. Yuri Avlasevich of Prof. Klaus Müllen's lab. Zongfu is an amazing theory collaborator for the bowtie work and has helped immensely in understanding the effects I measured experimentally. Dr. Avlasevich was kind enough to share the DNQDI and TPQDI molecules which made much of this work possible. Finally, Kelley Rivoire is an expert in photonic crystal cavities and it was a pleasure to work with her to attempt to couple fluorescence molecules to the cavities she fabricated.

Above are mentioned my primary collaborators, but I learned just as much from the other lab members, of which there have been many. I would like to thank Jaesuk Hwang, Kallie Willets, Stephanie Nishimura, Kit Werley, Hanshin Hwang, Adam Cohen, Marcelle Koenig, Andrea Kurtz, So Yeon Kim, Jian Cui, Nicole Tselentis, Magnus Hsu, Nick Conley, Julie Biteen, Sam Lord, Randy Goldsmith, Alex Fuerstenberg, Majid Badieirostami, Steven Lee, Jianwei Liu, Hsiao-lu Lee, Whitney Duim, Lana Lau, Yan Jiang, Mike Thompson, Sam Bockenhauer, Quan Wang, Marissa Lee, Matt Lew, and Yao Yue for making my time in the Moerner lab full of ideas and enjoyable.

I have so far only listed the people who have contributed to the science in this thesis, but there are a great many more who have supported me outside of work. I came to Stanford with very few connections and have since found a home in the Stanford community, primarily due to the warmth and love from the friends I have made here, of which there are too many to name here. I thank everyone who has helped make my time here educational, as well as fun.

In closing, I'd like to thank my family: Amir, Linda, Yusuf, Ali, Amina, and Yunus Kinkhabwala, for their steady support throughout my entire life. They encouraged me to study science and math at an early age, which has stuck with me to this day. Finally, I'd like to thank my partner for the last 5.5 years, David Press, who has always been there to provide love and support whenever I needed it.

Contents

List of Figures

Chapter 1 - Introduction

1.1 Overview

Richard Feynmann stated in 1959 that "There's Plenty of Room at the Bottom", predicting the recent explosion in nanotechnology research. Nanotechnology is the study of materials systems at nanometer-scale dimensions. At first glance, just making an object small may not seem interesting, but a material often behaves differently on nanoscale dimensions than in bulk, which has led to many interesting problems as well as new opportunities in miniaturization. While nanotechnology has touched many areas of research, this thesis concerns nano-optics, the study of light on the nanoscale, by using two devices to control local electromagnetic fields: the bowtie nanoantenna and the photonic crystal cavity. In particular, these two structures will be used to modify and control optical emission from nanoscale emitters.

1.2 Optical Plasmonic Nanoantennas

1.2.1 Motivation

Antennas are inescapable today. They are used to receive and transmit radio and microwave range electromagnetic waves in devices such as cell phones, televisions, laptops, and radios. These antennas are capable of capturing and concentrating these fields efficiently to subwavelength dimensions and usually converting them to currents in an external circuit, but in this thesis, the concern is not

with the external circuit, but only with the local concentration of the electromagnetic field. Notably, scaling radio-wave antennas to optical frequencies proved to be a challenge. Optical frequency antennas are interesting because light cannot be focused to an infinitesimally small point with normal lenses, instead it is limited by diffraction to

$$d = \frac{\lambda}{2NA} \qquad [1.1]$$

where λ is the wavelength of light and NA is the numerical aperture of the optics used. For visible wavelengths the diffraction limit is ~200-300 nm, much larger than many objects of interest, such as single molecules, which are typically just a few nm in size (Figure 1-1). An antenna can help concentrate light to a smaller area and decrease the mismatch in size between light and the nanoscale emitter.

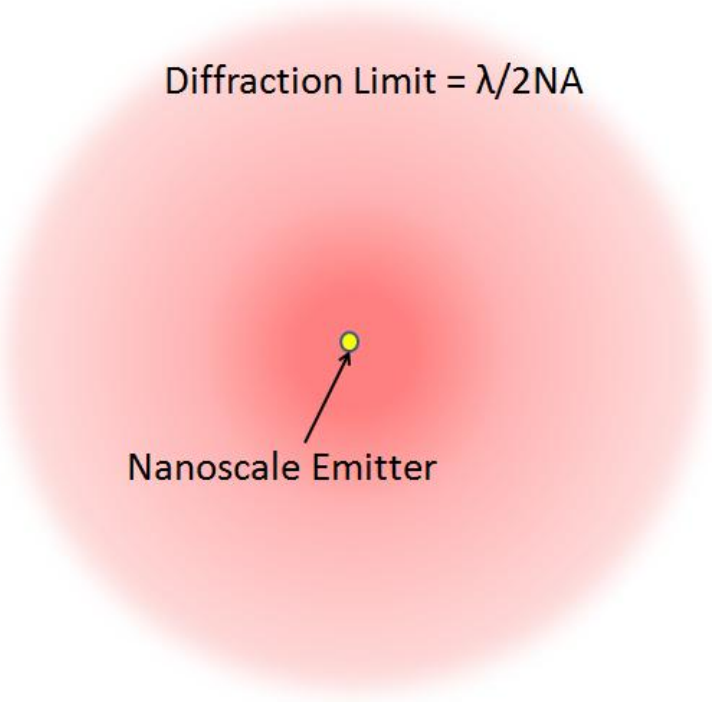

Figure 1-1: Size mismatch between the diffraction limit and a nanoscale emitter.

1.2.2 The Drude Model

At radio frequencies, the free electrons within an antenna oscillate with the AC electromagnetic field of the passing wave. At high frequencies, such as optical frequencies, this simple model of free electrons moving instantaneously in response to an electromagnetic field fails. The Drude model[1] is a slightly more complicated model of electromagnetic fields in bulk metals. In this model, the metal is composed of fixed positively charged nuclei surrounded by free, unbound conduction electrons[2]. This model predicts that when a metal is excited by an electromagnetic field, then the field in the metal must satisfy the wave equation:

$$-\Delta^2 \boldsymbol{E} = \frac{\omega^2}{c^2}\epsilon(\omega)\boldsymbol{E} \qquad [1.2]$$

where $\boldsymbol{E}$ is the electric field, c is the speed of light, ω is the frequency, and $\epsilon(\omega)$ is the complex dielectric constant[2]. At high frequencies, $\epsilon(\omega)$ is given by:

$$\epsilon(\omega) = 1 - \frac{\omega_p^2}{\omega^2} \qquad [1.4]$$

$$\omega_p = \sqrt{\frac{4\pi n e^2}{m}} \qquad [1.5]$$

where ω_p is the plasma frequency, n is the electron density, e is the charge of an electron and m is the mass of an electron. When $\omega = \omega_p$, plasmons, or coherent collective oscillations of the free electrons in the metal, can be excited in the metal.

1.2.3 Surface Plasmon Polaritons

In real materials, the penetration depth, or skin depth, of a metal when excited by visible or near-IR light is a few tens of nm. This means that only electrons near the

surface of a metal are excited, as shown in Figure 1-2. The condition necessary to excite a surface plasmon polariton (SPP) at the interface is found by applying appropriate boundary conditions for a metal/dielectric interface to Maxwell's equations, yielding the following dispersion relation:

$$k = \frac{\omega}{c}\sqrt{\left(\frac{\epsilon_d \epsilon_m}{\epsilon_d + \epsilon_m}\right)} \qquad [1.5]$$

where k is the wavenumber, while ϵ_d and ϵ_m are the permittivities of the dielectric and metal respectively[3]. Notice that since ϵ_d is real and positive, for k to be real (and thus yield a propagating wave), the real part of ϵ_m must be negative and larger than ϵ_d. This condition is satisfied at visible wavelengths for the metals silver and aluminum and in the near-IR for gold and copper[4].

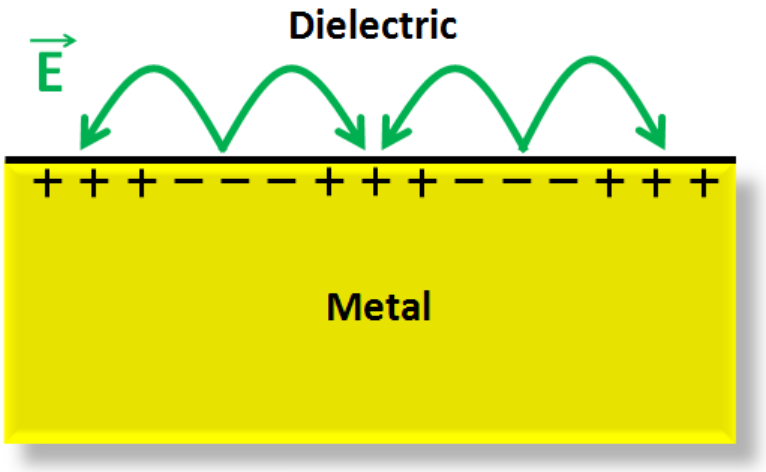

Figure 1-2: Surface plasmon polariton excited at a metal/dielectric interface.

1.2.4 Localized Surface Plasmon Resonance

Now consider the case of exciting a plasmon in a nanoscale object such as a small metal sphere or colloidial particle. In such a confined system, the plasmon cannot propagate and is instead referred to as a localized surface plasmon resonance

(LSPR). Figure 1-3 shows schematically how electrons in a small metal colloid respond to an electromagnetic field at the LSPR. Notice that the electric field pushes the electrons to one side of the particle, leaving behind positively-charged holes on the other side. By separating and localizing the electrons and holes on opposite ends of the nanoparticle, there is a local buildup of electric field, which produces an optical antenna. For a metal sphere of diameter<<λ, the LSPR resonance is located at (ENTER EQUATION), and differently-shaped small objects have different resonance conditions.

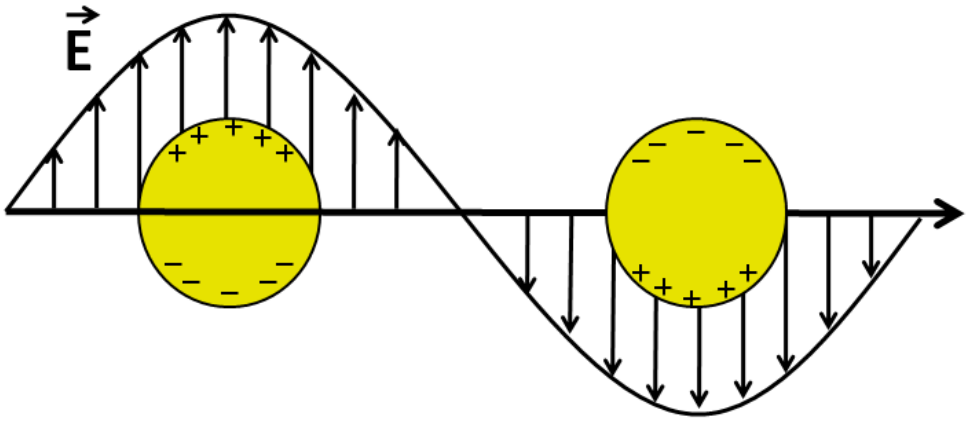

Figure 1-3: Response of free electrons in a metal colloid to an AC electromagnetic field tuned to the particle's plasmon resonance.

1.2.5 Gold Bowtie Nanoantenna Plasmon Resonance

Metallic spheres are often used experimentally because making small metallic particles by colloidial chemistry is are relatively simple, and spherical systems are analytically solvable using Mie theory[5], but they do not give the highest electric field enhancements or tightest field confinement. Many other geometries have been studied

such as metal wires[6-9], strips[10, 11], cones[12, 13], and bowties[14-21] for a diverse set of applications including, but not limited to, photodetectors[22], plasmonic lasers[23], solar cells[24], apertureless near-field microscopy[25], and photolithography[15] as summarized in the excellent review of Ref.[26]. The bowtie shape was first studied at mid-infrared wavelengths in the laboratory of Gordon Kino and was shown to produce efficient antenna effects[27]. This work was then scaled to fabricate nanoscale antennas in the near-IR[17], consisting of two 80 nm triangles separated by as small a distance as possible, typically ~10 nm (SEM in Figure 1-4). When this subwavelength object is excited resonantly, electrons in both triangles of this antenna move in the direction of the electric field, causing a concentration of negative charge in the tip of one triangle and a concentration of positive charge in the tip of the other triangle (Figure **1**-**5**a), a field configuration which switches for every half-cycle of the applied electromagnetic wave. This configuration leads to a very strong buildup of field in the gap, as seen in the finite-difference time-domain simulation in Figure **1**-**5**b.

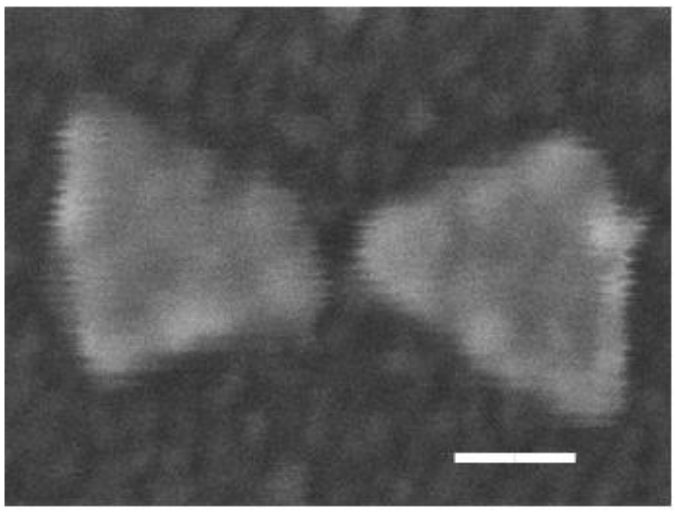

Figure 1-4: SEM (scanning electron microscopy) image of a gold bowtie nanoantenna fabricated with electron beam (E-beam) lithography. Scale bar = 40 nm.

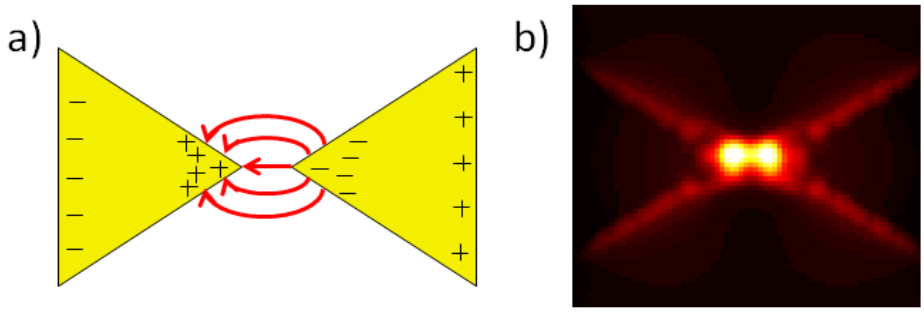

Figure 1-5: a) Schematic of electron and hole concentration due to excitation of the bowtie at its plasmon resonance. b) Map of $|E|^2$ for gold bowtie nanoantenna pumped at 856nm from Ref [28].

By measuring the scattering of light (experimental details discussed in Chapter 2) by these structures, the plasmon resonance frequency can be experimentally determined. It was found that small gap bowties (~10nm) have resonances around 820nm (Figure 1-6a)[17]. As the gap size increases, the resonance first blue shifts, due to larger overall antenna size, before eventually red shifting toward the single triangle resonance[17]. These results illustrating the coupling between the two plasmons of the two triangle to produce a plasmon resonance for the overall bowtie agree well with finite-difference time-domain (FDTD) simulations of the plasmon resonance[28].

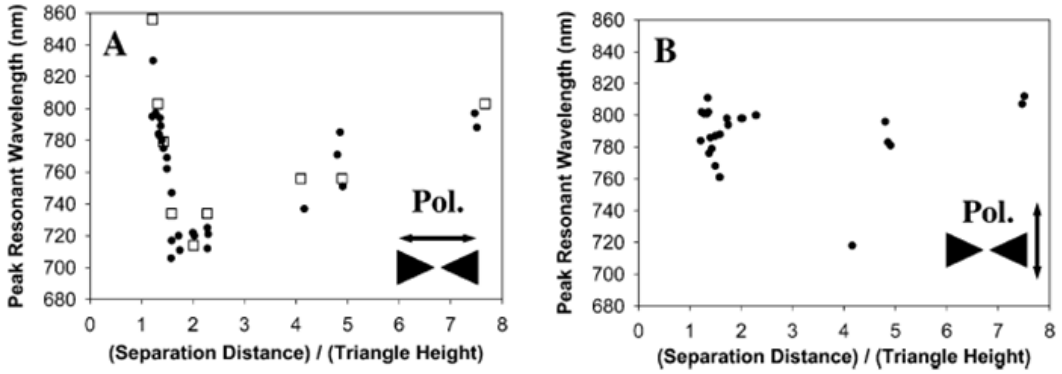

Figure 1-6: a) Peak scattering wavelength versus bowtie gap size (measured as gap size/triangle height) for long axis excitation polarization direction. b) Peak scattering wavelength versus bowtie gap size for short axis excitation polarization direction. Figure from Ref [17].

1.2.6 Measurement of Enhanced Fields of Gold Bowtie Nanoantenna

To finish characterizing the bowtie nanoantenna, the enhanced fields when pumped at resonance were experimentally measured[16]. Gold has an intrinsic two-photon photoluminescence (TPPL) that arises from transitions within the conduction band (d band to sp band)[16, 29-31]. TPPL is proportional to the fourth power of the excitation electric field strength. The ratio of the gold bowtie's TPPL to a smooth gold film's TPPL is then a measure of the enhanced fields of the bowtie nanoantenna. In Ref.[16], the bowtie nanoantenna was pumped with a pulsed Ti:Sapphire laser tuned to 830 nm, resulting in TPPL emission. TPPL emission from 460 nm to 700 nm was collected and compared to the emission from a smooth gold film of the same thickness in order to measure the local enhancement of fields due to the bowtie nanoantenna as a function of gap size (Figure 1-7). It was found that as the gap of the bowtie gets smaller, the electric field intensity ($|E|^2$) can reach values > 10^3 times larger than the

incident field intensity. The two triangles of the bowtie require close proximity (< 50nm) to be coupled, so the field intensity quickly drops as the bowtie's gap size increases, until reaching the field intensity expected for a single triangle beyond 50nm gap sizes.

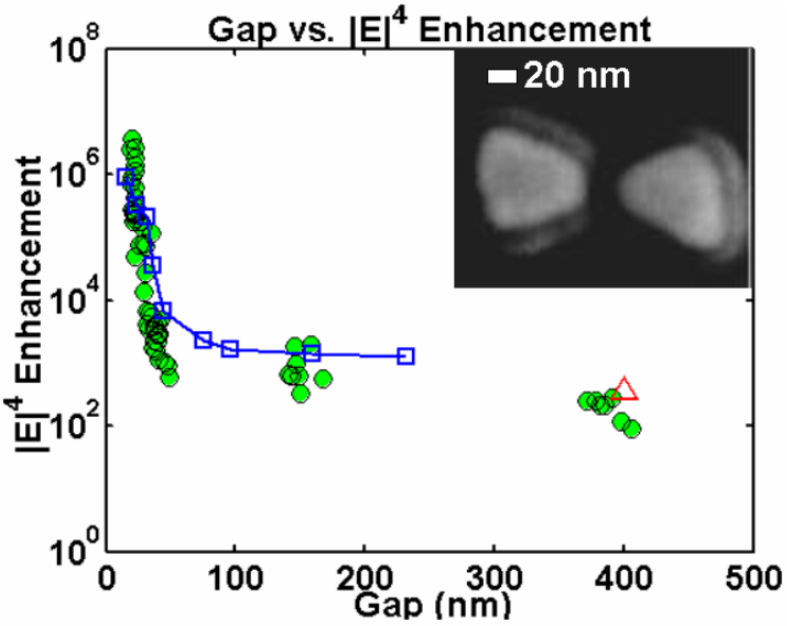

Figure 1-7: Measurement of enhanced $|E|^4$ fields near a gold bowtie nanoantenna as a function of bowtie gap size using TPPL. Figure from Ref. [16].

The previous work in the Moerner Lab described above characterized the bowtie nanoantenna by measuring its plasmon resonance, enhancement of local field strength, and SERS effects. One goal of this thesis was to understand how these highly enhanced and confined fields affected a single-molecule's fluorescence (Chapter 3-4).

1.3 Photonic Crystals

1.3.1 Motivation

The bowtie nanoantenna highly confines and enhances local field strengths, but it is not the only nanophotonic structure capable of altering local electromagnetic fields. Multi-dimensional photonic crystals first introduced by Eli Yablonovitch[32] and Sanjeev John[33] in 1987, are also able to trap and manipulate light. Photonic crystals are formed by a periodic array of material regions with different dielectric constants in either one, two, or three dimensions. The periodicity is often on the order of the light's wavelength. Distributed scattering of light from the periodic interfaces leads to the formation of dispersive energy bands, sometimes with energy band gaps. Light within the energy gap experiences constructive interference on reflection and destructive interference on transmission, and is therefore unable to propagate in the photonic crystal material. The photonic crystal thus acts as a highly reflective mirror to frequencies within the energy gap. One can then engineer optical waveguides and high-Q cavities by creating defects in the periodic photonic crystal lattice.

1.3.2 Planar Photonic Crystal Cavities

Planar photonic crystal cavities are fabricated out of thin membranes of semiconductor, where the semiconductor is used as a (high index) dielectric in the wavelength regime of the semiconducting gap. A hexagonal closed packed array of air holes is etched into this film as in Figure 1-8a. Three holes in the middle of the photonic crystal are not etched – this defect produces the cavity region. When a photon enters the cavity region, it is trapped in three dimensions. In the Z-dimension,

light is confined due to total internal reflection off of the top and bottom surfaces of the thin membrane. In the X and Y dimensions (photonic crystal plane), light is trapped due to Distributed Bragg Reflection (DBR) because the light energy falls within the energy band gap of the photonic crystal.

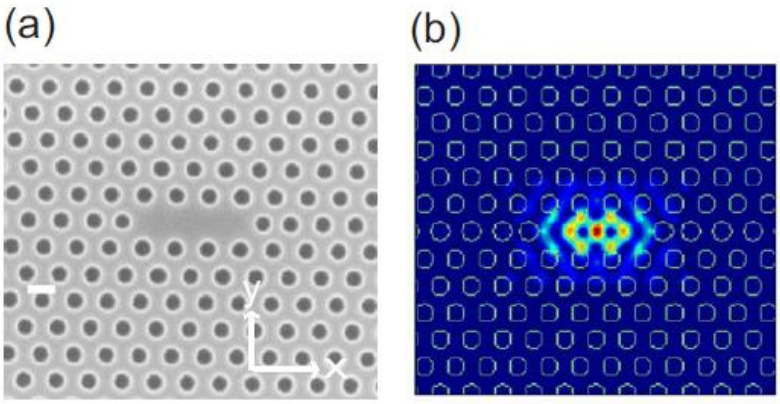

Figure 1-8 a) Scanning electron microscope (SEM) image of a photonic crystal cavity. b) Electric field profile of photonic crystal cavity excited at resonance for the fundamental cavity mode . (After Ref [34]).

The quality (or Q) factor is proportional to how long light is trapped inside the cavity before escaping and is simply:

$$Q = \frac{f_0}{\Delta f} \qquad [1.6]$$

where f_0 and Δf are the frequency center position and width of the resonance. The Q for GaP photonic crystal cavities discussed in this thesis can be as high as 10,000[34]. Quality factors up to 2.5 x 10^6 are achievable in silicon[35], but these cavities have resonances further in the infrared.

In Chapter 6 of this thesis, fluorescent molecules are coupled to a photonic crystal cavity using a lithographic approach and optical experiments demonstrate successful coupling between the molecules and photonic crystal cavity modes.

1.4 Fluorescence

1.4.1 Motivation

Bowtie nanoantennas and photonic crystal cavities are interesting structures because they both alter local electromagnetic fields. This thesis measures the effect these structures have on molecular fluorescence, an effect that depends heavily on local electromagnetic fields. Fluorescence is a photophysical process whereby light of one wavelength excites a molecule, which in turn emits light of a lower energy, or longer wavelength. Fluorescent dyes have been commonly used as markers in biology – a molecule/protein/area of interest in a cell is covalently linked to a fluorescent molecule and the fluorescent molecule's intensity can report upon the location and environment of the target.

1.4.2 Fundamentals

The simplest model to describe emission of light by a molecule is the two-level system, with each of the two primary electronic states are decorated with a progression of vibrational modes. Fluorescence consists of the absorption of a photon by a molecule followed by the emission of a lower energy photon (red-shifted wavelength) as seen in the Jablonksi diagram in Figure 1-9a. On the excitation side, a laser is chosen whose energy is equivalent to or greater than the direct ground state (S_0) to excited state (S_1) allowed dipole transition (blue arrow). The singlet state (S) refers to

the fact that all of the electrons in this state are paired with another electron of anti-parallel spin. A transition between two singlet states is an optically allowed transition, because it does not require a spin flip to occur. Figure 1-9b shows schematically the absorption (blue) and emission (red) spectra from the molecule TPQDI (see Chapter 3 for more details on this dye.) The excitation laser can be chosen at any wavelength where there is absorption by the molecule. Once the molecule is in the excited state, internal conversion, or fast, non-radiative vibrational relaxations, (black wavy arrow) occur in a few ps and the molecule relaxes to the lowest level of the electronic excited state. At this point, the molecule typically remains in the excited state for ~ few ns before relaxing to the ground state. This relaxation can either be radiative (red arrow), where the molecule emits a lower energy photon, or non-radiative (black arrow), where the molecule does not emit a photon but simply gives off the energy as heat and moves through other levels to relax to the ground state (internal conversion or intersystem crossing for instance). The width of the emission and the peaks in the spectrum in Figure **1-9**b are due to the number of different vibrational levels available for the molecule to relax down to the ground state at room temperature.

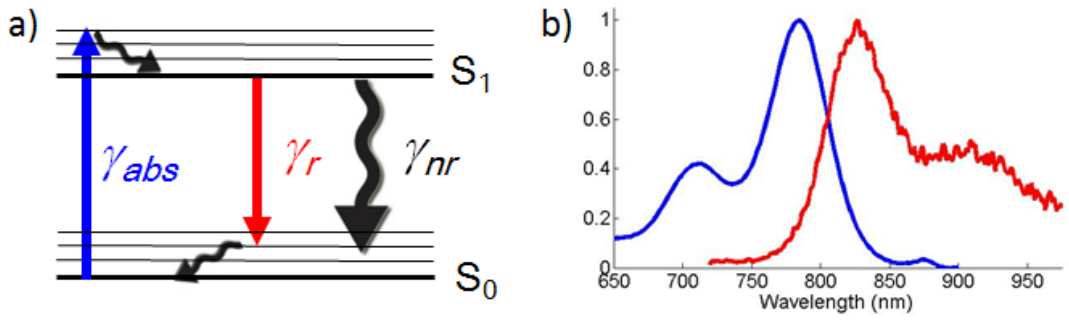

Figure 1-9: a) Simplified Jablonksi diagram for a typical fluorescence transition. The emitter is pumped out of the ground state (S_0) and into vibrational sidebands of the electronic excited state (S_1) with rate γ_{abs} (blue arrow). Internal conversion (fast, non-radiative transitions) allows the molecule to relax into the lowest level of the excited state. At this point, the molecule relaxes back to the ground state either radiatively with rate γ_r (red arrow) or non-radiatively with rate γ_{nr} (black wavy arrow). Another internal conversion step (black wavy arrow) allows the molecule to relax to the lowest ground state level. b) Absorption (blue) and fluorescence emission (red) spectra from the molecule TPQDI.

1.4.3 Single-Molecule Fluorescence

Over 20 years ago, it was discovered that a single molecule could be optically detected, first based on a measuring a single-molecule's absorption of light[36], and then demonstrated by measuring absorption by recording a single-molecule's fluorescence emission[37] at low temperature. Room temperature detection of single-molecule fluorescence[38] quickly followed and the field of single-molecule spectroscopy and imaging rapidly grew, in particular in the biological community. Now, instead of performing bulk experiments and only measuring average behavior, it is possible to measure the behavior of every target molecule and understand heterogeneity in behavior.

In order to detect a single-molecule's fluorescence, a very good fluorophore is necessary. A good fluorophore has several properties. First, it absorbs light well, which corresponds to a high absorption cross-section. Second, a good fluorophore tends to emit radiatively instead of non-radiatively, which is reflected in the fluorescence quantum efficiency (QE). The QE is the probability that a molecule will emit a fluorescence photon per photon absorbed and is given by:

$$\eta = \frac{\gamma_r}{\gamma_r + \gamma_{nr}} \qquad [1.7]$$

where η is the QE, while γ_r and γ_{nr} are the radiative and non-radiative decay rates, respectively. If the QE is 100%, then the molecule always emits a photon and never decays non-radiatively, making it an ideal fluorophore for most applications. Finally, a good fluorophore must be stable and capable of emitting many photons before photobleaching. Photobeaching refers to any change in the molecule that occurs during illumination, typically involving a chemical reaction that alters the molecule's identity, causing it to no longer fluoresce. One common pathway for a molecule to photobleach can occur when the molecule enters a triplet state, a forbidden transition from the singlet state that occurs with low probability. The triplet state represents an intermediate from which the molecule can return to the singlet ground state eventually. However, the triplet state is long-lived and so there is time for the molecule to react with triplet oxygen and cause the molecule to no longer fluoresce (photooxidation). This pathway is just an example; the exact photobleaching mechanism for any particular molecule would have to be studied in detail and is not the subject of this work. A good fluorophore will emit ~10^6 photons before eventual degradation[39].

1.5 Fluorescence Correlation Spectroscopy

1.5.1 Motivation

Using fluorescence correlation spectroscopy (FCS) to measure dynamics from a fluctuating fluorescence signal was first described in 1972[40], before the invention of single-molecule spectroscopy. It was eventually realized that the ability to measure

FCS allowed for very dilute solutions to be studied and fluorescence dynamics from a collection of many single-molecule intensity bursts to be analyzed[41, 42]. In this technique, a laser is tightly focused into a dilute solution of molecules (Figure 1-10). A confocal fluorescence microscope then measures the bright flashes of fluorescence from small numbers or single molecules passing through the focused laser spot. When these flashes of fluorescence are analyzed, any process that changes the fluorescence on time scales from nanoseconds to the transit time of a few milliseconds can be measured. The typical analysis involves autocorrelation of the emission signal, which extracts information from huge numbers of passages of molecules through the focal volume. Examples of processes that affect fluorescence on these time scales are photon antibunching, dark state bottlenecks, photobleaching, conformational dynamics, FRET, and diffusion. FCS has been used to measure these processes in a number of free dye and biological systems; see Ref.[43, 44] for reviews of key work in this field.

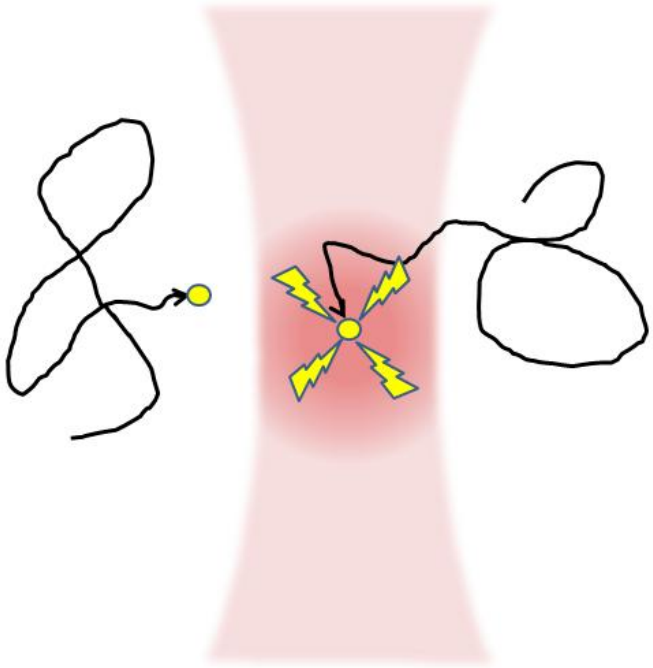

Figure 1-10: Experimental schematic for a typical FCS experiment. A laser is focused tightly such that when fluorescent molecules (yellow circles with trajectories in black) in solution wander through the focus of the laser, bright flashes of light are detected.

1.5.2 Fundamentals

When performing an FCS experiment, either the autocorrelation is measured with a special-purpose hardware autocorrelator, or each photon's arrival time is measured precisely and then the autocorrelation $G(\tau)$ of the time trace is computed in software using:

$$G(\tau) = \frac{\langle \delta I(t) \delta I(t+\tau) \rangle}{\langle I(t) \rangle^2} \qquad [1.8]$$

where I(t) is the intensity (rate of photon emission) at time t. This autocorrelation function will reflect any dynamics in the dye that produce a change in the fluorescence emission before the molecule diffuses out of the focal volume (typically a few

milliseconds). For a confocal microscope, an ellipsoidal Gaussian excitation volume can be assumed and G(τ) for just simple diffusion is given by:

$$G(\tau) = \frac{1}{N} \frac{1}{\left(1+{}^{\tau}/_{\tau_D}\right)\sqrt{\left(1-a^{-2}\left({}^{\tau}/_{\tau_D}\right)\right)}} \qquad [1.9]$$

where N is the average number of molecules in the observation volume, a is a geometrical factor dependent upon the shape of the excitation volume, τ is the time lag, and τ_D is the diffusion time[41]. The factor a is typically calibrated for a specific microscope using a dye with known properties, so that the only free parameters are N and τ_D. Notice that if the concentration of the solution (N) is known, then τ_D can be measured, or conversely if τ_D is known, then N can be measured. Clearly the contrast is highest for small values of N.

1.5.3 Zero-Mode Waveguides for High Concentration FCS

FCS is usually performed at low concentrations (~0.01-1 nM), because in order to measure the largest fluctuations in the fluorescence there needs to be on average less than one molecule in the illumination volume at any one time. However, many biological studies, such as DNA replication [45], must occur at high concentrations. One solution to this problem is to use a zero-mode waveguide[45] to confine the illumination volume much further than is possible with normal diffraction-limited confocal microscopy. Zero-mode waveguides are simply holes in metal films that are smaller than the diffraction limit. Electromagnetic waves cannot propagate through subwavelength holes, so there is only a weak penetration of evanescent waves into these apertures, restricting illumination to a few 10's of nm from the substrate. A typical geometry consists of a thin (100 nm) aluminum film with 80nm diameter holes

on a transparent substrate[45], such as in Figure 1-11. The fact that illumination is now evanescently coupled means that excitation in confined in the propagation direction. The production of fluorescence is also confined in the other two dimensions due to the metallic hole excluding molecules from the excitation region, leaving a very small total excitation volume, which allows for single-molecule FCS or single-molecule direct observations to be performed at much higher fluorophore concentrations in solution above the waveguide (~10 μM)[45]. This scheme has been extended to implement real-time single-molecule sequencing of DNA[46], as well as real-time translation of RNA into protein[47] and is also being commercialized by the company Pacific Biosciences. Chapter 4 concerns an extension of this concept to instead use bowtie nanoantennas for single-molecule FCS at high fluorophore concentrations.

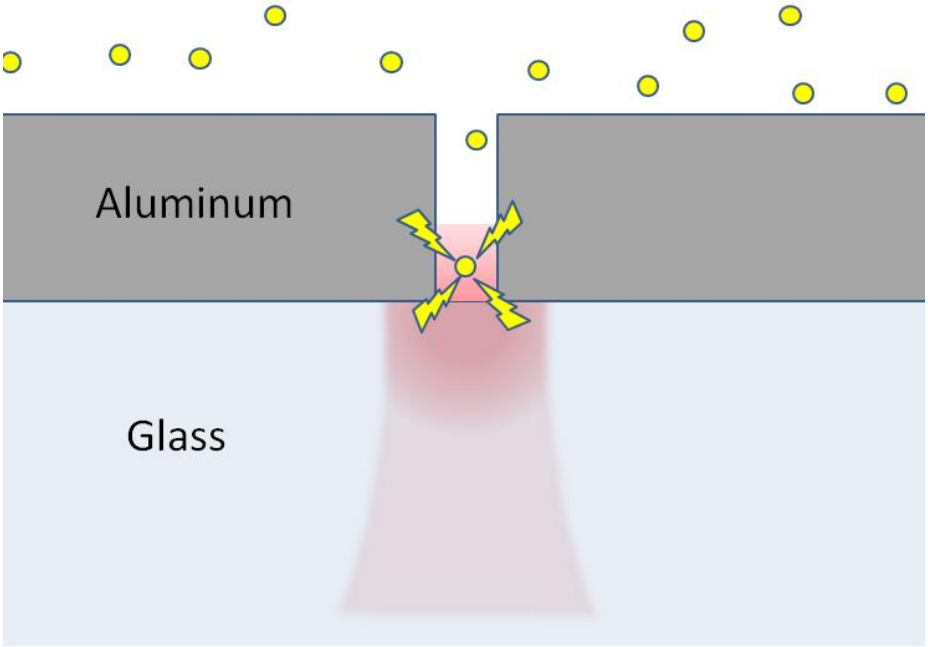

Figure 1-11: Zero-mode waveguide geometry for high-concentration FCS. Yellow circles are molecules that occasionally enter the hole in the aluminum and emit fluorescence into the collection optics.

1.5.4 Conclusions

This chapter has outlined a number of different research concepts, from dielectric photonic crystal cavities, to plasmonic optical antennas, to fluorescence. This thesis combines these areas to show that photonic crystal cavities and gold bowtie nanoantennas can be used in powerful ways to modify one of the most important diagnostic tools available to biologists today, namely fluorescence. Chapter 2 describes the optical and nanofabrication techniques used throughout the thesis. In chapter 3, bowtie nanoantennas are used to enhance a single-molecule fluorescence by a factor of 1,300 and electromagnetic simulation are used to understand this enhancement. Chapter 4 extends the work of chapter 3 to include molecules in solution so that dynamics in the fluorescence signal can be measured. Chapter 5 describes attempts to fabricate a bowtie nanoantenna onto an AFM tip, so that the bowtie could eventually be positioned relative to a molecule. In Chapter 6, fluorescent molecules are lithographically patterned onto photonic crystal cavities and the coupling between the molecules and cavity is measured. Finally, Appendices A, B, and C provide specific details on operating the Raith150 E-beam lithography tool, the FEI Strata Focused Ion Beam tool, and aligning the home-built confocal microscope used in this thesis. Where collaborators are involved, they are mentioned at the start of each chapter.

References

1. Drude, P. Zur Elektronentheorie der Metalle. *Annalen der Physik* **306**, 566 (1900).

2. Ashcroft, N. W. & Mermin, N. D. in *Solid State Physics* (ed Crane, D. G.) 826 (Harcourt College Publishers, New York, NY, 1976).

3. Raether, H. in *Surface Plasmons on Smooth and Rough Surfaces and on Grating* (Springer-Verlag, Berlin, 1988).

4. Mohammadi, A., Sandoghdar, V. & Agio, M. Gold, Copper, Silver, and Aluminum Nanoantennas to Enhance Spontaneous Emission. *J. Comput. Theor. Nanosci.* **6**, 2024 (2009).

5. Mie, G. Contributions to the Optics of Turbid Media, Particularly of Colloidal Metal Solutions. *Annalen Der Physik* **25**, 377 (1908).

6. Novotny, L. Effective Wavelength Scaling for Optical Antennas. *Phys. Rev. Lett.* **98**, 266802 (2007).

7. Bryant, G., Garcia de Abajo, F. J. & Aizpurua, J. Mapping the Plasmon Resonances of Metallic Nanoantennas. *Nano Lett.* **8**, 631 (2008).

8. Ditlbacher, H. *et al*. Silver Nanowires as Surface Plasmon Resonators. *Phys. Rev. Lett.* **95**, 257403 (2005).

9. Taminiau, T. H., Stefani, F. D., Segerink, F. B. & van Hulst, N. Optical Antennas Direct Single-Molecule Emission. *Nat. Phot.* **2**, 234-237 (2008).

10. Sondergaard, T. & Bozhevolnyi, S. I. Slow-Plasmon Resonant Nanostructures: Scattering and Field Enhancements. *Phys. Rev. B* **75**, 073402 (2007).

11. Sondergaard, T. & Bozhevolnyi, S. I. Metal Nano-strip Optical Resonators. *Opt. Express* **15**, 4198 (2007).

12. Stockman, M. I. Nanofocusing of Optical Energy in Tapered Plasmonic Waveguides. *Phys. Rev. Lett.* **93**, 137404 (2004).

13. Verhagen, E., Spasenovic, M., Polman, A. & Kuipers, L. Nanowire Plasmon Excitation by Adiabatic Mode Transformation. *Phys. Rev. Lett.* **192**, 203904 (2009).

14. Fromm, D. P. *et al*. Exploring the chemical enhancement for surface-enhanced Raman scattering with Au bowtie nanoantennas. *J. Chem. Phys.* **124**, 061101 (2006).

15. Sundaramurthy, A. *et al*. Toward Nanometer-scale Optical Photolithography: Utilizing the Near-Field of Bowtie Optical Nanoantennas. *Nano Lett.* **6**, 355-360 (2006).

16. Schuck, P. J., Fromm, D. P., Sundaramurthy, A., Kino, G. S. & Moerner, W. E. Improving the mismatch between light and nanoscale objects with gold bowtie nanoantennas. *Phys. Rev. Lett.* **94**, 017402 (2005).

17. Fromm, D. P., Sundaramurthy, A., Schuck, P. J., Kino, G. S. & Moerner, W. E. Gap-dependent optical coupling of single "bowtie" nanoantennas resonant in the visible. *Nano Lett.* **4**, 957-961 (2004).

18. Farahani, J. N. *et al*. Bow-tie optical antenna probes for single-emitter scanning near-field optical microscopy. *Nanotech* **18**, 125506-125510 (2007).

19. Farahani, J. N., Pohl, D. W., Eisler, H. -. & Hecht, B. Single Quantum Dot Coupled to a Scanning Optical Antenna: A Tunable Superemitter. *Phys Rev Lett* **95**, 017402-1-017402-4 (2005).

20. Merlein, J. *et al*. Nanomechanical Control of an Optical Antenna. *Nature Photonics* **2**, 230 (2008).

21. Muhlschlegel, P., Eisler, H. -., Martin, O. J. F., Hecht, B. & Pohl, D. W. Resonant optical antennas. *Science* **308**, 1607-1609 (2005).

22. Tang, L. *et al*. Nanometre-Scale Germanium Photodetector Enhanced by a Near-Infrared Dipole Antenna. *Nature Photonics* **2**, 226 (2008).

23. Oulton, R. F. *et al*. Plasmon Lasers at Deep Subwavelength Scale. *Nature* **461**, 629 (2009).

24. Atwater, H. A. & Polman, A. Plasmonics for Improved Photovoltaic Devices. *Nature Materials* **9**, 205 (2010).

25. Novotny, L. & Stranick, S. J. Near-field Optical Microscopy and Spectroscopy with Pointed Probes. *Ann. Rev. of Phys. Chem.* **57**, 303 (2006).

26. Schuller, J. A. *et al*. Plamonics for Extreme Light Concentration and Manipulation. *Nature Materials* **9**, 193 (2010).

27. Crozier, K. B., Sundaramurthy, A., Kino, G. S. & Quate, C. F. Optical antennas: Resonators for local field enhancement. *J. Appl. Phys.* **94**, 4632-4642 (2003).

28. Sundaramurthy, A. *et al*. Field enhancement and gap-dependent resonance in a system of two opposing tip-to-tip Au nanotriangles. *Phys.Rev.B* **72**, 165409 (2005).

29. Boyd, G. T., Yu, Z. H. & Shen, Y. R. Photoinduced luminescence from the noble metals and its enhancement on roughened surfaces. *Phys.Rev.B* **33**, 7923-7936 (1986).

30. Beversluis, M. R., Bouhelier, A. & Novotny, L. Continuum generation from single gold nanostructures through near-field mediated intraband transitions. *Phys.Rev.B* **68**, 115433 (2003).

31. Bouhelier, A., Beversluis, M. R. & Novotny, L. Characterization of nanoplasmonic structures by locally excited photoluminescence. *Appl. Phys. Lett.* **83**, 5041-5043 (2003).

32. Yablonovitch, E. Inhibited Spontaneous Emission in Solid-State Physics and Electronics. *Phys Rev Lett* **58**, 2059 (1987).

33. John, S. Strong Localization of Photons in Certain Disordered Dielectric Superlattices. *Phys Rev Lett* **58**, 2486 (1987).

34. Rivoire, K. *et al*. Lithographic Position of Fluorescent Molecules on High-Q Photonic Crystal Cavities. *Appl. Phys. Lett.* **95**, 123113 (2009).

35. Takahashi, Y., Hagino, H., Tanaka, Y., Asano, T. & Noda, S. High-Q Photonic Nanocavity with a 2-ns Photon Lifetime. *Conf on asers and Electro-Optics*, QF01 (2008).

36. Moerner, W. E. & Kador, L. Optical detection and spectroscopy of single molecules in a solid. *Phys. Rev. Lett.* **62**, 2535-2538 (1989).

37. Orrit, M. & Bernard, J. Single pentacene molecules detected by fluorescence excitation in a p-terphenyl crystal. *Phys. Rev. Lett.* **65**, 2716-2719 (1990).

38. Betzig, E. & Chichester, R. J. Single Molecules Observed by Near-Field Scanning Optical Microscopy. *Science* **262**, 1422-1425 (1993).

39. Lord, S. J. *et al*. Photophysical Properties of Acene DCDHF Fluorophores: Long-Wavelength Single-Molecule Emitters Designed for Cellular Imaging. *J. Phys. Chem. A* **111**, 8934-8941 (2007).

40. Magde, D., Elson, E. & Webb, W. W. Thermodynamic Flucutations in a Reacting System - Measurement by Fluorescence Correlation Spectroscopy. *Phys. Rev. Lett.* **28**, 705 (1972).

41. Eigen, M. & Rigler, R. Sorting Single Molecules: Application to Diagnostics and Evolutionary Biotechnology. *Proc. Natl. Acad. Sci. U. S. A.* **91**, 5740-5747 (1994).

42. Rigler, R. Fluorescence correlations, single-molecule detection, and large number screening: applications in biotechnology. *J. Biotechnol.* **41**, 177-186 (1995).

43. Hess, S. T., Huang, S., Heikal, A. A. & Webb, W. W. Biological and chemical applications of fluorescence correlation spectroscopy: a review. *Biochemistry* **41**, 697-705 (2002).

44. Rigler, R., Elson, E. & Elson, E. in *Springer Series in Chemical Physics Vol. 65; Fluorescence Correlation Spectroscopy; Springer Series Chem. Phys* (eds Schaefer, F. P., Toennies, J. P. & Zinth, W.) (SpringerRigler, R, Berlin, 2001).

45. Levene, M. J. *et al*. Zero-Mode Waveguides for Single-Molecule Analysis at High Concentrations. *Science* **299**, 682-686 (2003).

46. Eid, J. & et. al. Real-Time DNA Sequencing from Single Polymerase Molecules. *Science* **323**, 133-138 (2009).

47. Uemura, S. *et al*. Real-time tRNA Transit on Single Translating Ribosomes at Codon Resolution. *Nature* **464**, 1012-1017 (2010).

Chapter 2 - Experimental Methods

2.1 Introduction

This chapter contains detailed information for the optical, nanofabrication, and nanocharacterization techniques needed to complete the experiments described in this thesis. While each technique is described in detail, references should be consulted as they give additional information on each technique.

2.2 Confocal Microscopy

2.2.1 Introduction

Confocal microscopy is a highly-sensitive, low background method for recording fluorescence images, particularly in biology[1-3]. In confocal microscopy, a laser is tightly focused to a diffraction-limited spot and raster scanned over a surface (or the sample is moved relative to the fixed laser spot). Fluorescence emission from the sample is focused through a pinhole, located at one of the microscope's conjugate plane's, which prevents emission from above and below the focal plane of the laser from passing through and reaching the detector. The fluorescence is measured from each spot and an image is built from this information pixel-by-pixel. The main advantage to confocal microscopy is Z-sectioning, which allows for fluorescence to be

detected only from a thin z-section of sample, thus allowing sensitive imaging of thick biological samples.

2.2.2 Optical Setup

Detailed information on setting up a confocal imaging pathway can be found in Appendix C, thus only the main ideas behind confocal microscopy will be mentioned here. Figure 2-1 shows a typical setup for the excitation and emission pathways in a confocal imaging setup for single-molecule imaging. For excitation (Figure 2-1a), a collimated laser beam is focused to a diffraction limited spot on the sample using a high numerical aperture (NA) objective. Diffraction limits the size of the focus to $\lambda/(2NA)$ in the X and Y directions, but note that the laser can excite fluorescence in a large range of Z positions.

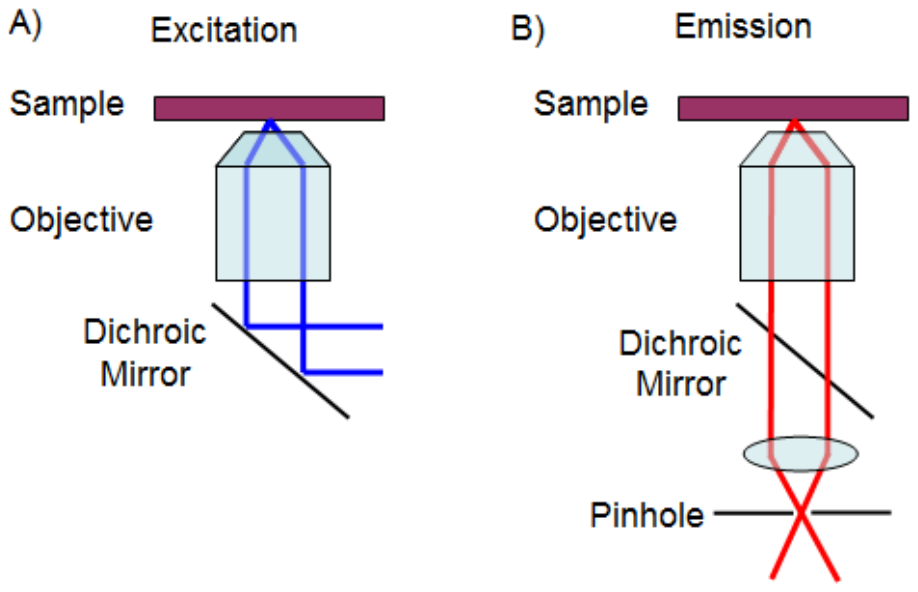

Figure 2-1: a) Schematic of typical excitation pathway for single-molecule confocal microscopy. b) Schematic of emission pathway for confocal microscope, showing the placement of a pinhole at the image plane, which provides Z-sectioning.

Once the sample is excited, fluorescent molecules located anywhere inside the laser's beam path inside the sample will emit light and roughly half of this emission is collected back through the same objective (Figure 2-1B). Note that above and below the focal plane, the optical intensity is lower, but the number of emitting molecules is larger. The fluorescence is collected and eventually focused through a confocal pinhole. The pinhole is the most important part of any confocal setup, because it provides the Z-sectioning capability of the microscope. By placing the pinhole at an image plane in the emission pathway, only emission from molecules located at the Z-focus of the microscope are focused through the pinhole and eventually collected on the detector. In this way, emission from a roughly 1μm Z-slice (depending on the wavelength and size of the pinhole) of the sample is imaged onto the (point) detector, which is usually a photon-counting avalanche photodiode.

In order to build up a full image, the sample is simply raster-scanned over the laser and the signal as a function of position is recorded, thereby building the image pixel-by-pixel.

2.2.3 Technical Issues for Single-Molecule Imaging

Special considerations are necessary when building a confocal microscope for single-molecule imaging and spectroscopy[4]. The main consideration for imaging single-molecules at room temperatures is that they tend to photobleach after emitting

~10^5-10^6 photons[5, 6]. It is, therefore, important to maximize the signal to noise ration (SNR)[4]:

$$SNR = \frac{N_{\text{det}}}{\sqrt{N_{\text{det}} + B + D}} \qquad [2.1]$$

where N_{det} is the number of fluorescence photons collected on the detector, B is the number of background photons from the sample, and D is the number of dark counts produced by the detector, all in a fixed integration time. To maximize the SNR, N_{det} should be as high as possible, which is accomplished by collecting every fluorescence photon possible and minimizing loss in the emission pathway, as well as minimizing B and D, which involves using non-fluorescent substrates, selecting the detector from stray light, and shielding the detector from stray light.

Interfering signals can be produced by many parts of the setup. First of all, the room lights add to this signal, so the first consideration in building any single-molecule microscope is to ensure the emission pathway is well-shielded for room lights. Next, dark counts from the detector, typically a silicon avalanche photodiode (APD), are always present. The dark counts from an APD can be as low as 50 counts/s, but only if the detector is initially very good and if the detector is treated well. The detector should never be turned on unless the user is sure the number of photons it will measure is $<10^6$/s. These are the two sources of D, dark counts.

Additional interfering sources are laser power dependent and contribute to background, B, whose Poisson variance represents a noise contribution. The biggest source of background is often due to improper filtering of the laser. Fluorescence

works by exciting a molecule at one wavelength and collecting light of a longer wavelength, or lower energy, which has been emitted by the molecule. This effect, called the molecular Stokes shift, is a result of excited state relaxation after optical excitation of the molecule[7]. The absorption cross section of a single molecule at room temperature is very low (~1 in every 10^8 photons will be absorbed by a molecule), which means that there is a great deal of excitation laser signal that needs to be removed from the emission pathway. By using a transparent sample such as molecules spun onto a glass coverslip, only ~4% of the excitation laser will reflect off of each glass surface into the emission pathway. This 4% signal is still MUCH greater than the fluorescence signal however, so appropriate choice of emission filters is important. The first filter in the emission pathway (also the last optic in the excitation pathway) is a dichroic mirror (beamsplitter) (Figure 2-1). A dichroic mirror reflects the excitation laser wavelength, while transmitting the longer wavelength fluorescence signal, but it does not attenuate the scattered pump light by OD = 6. So, after the pinhole and collimating lens, typically extra long pass or bandpass emission filters, at least one but sometimes two, are placed to ensure that only fluorescence photons reach the APD. In addition, the laser source should be filtered to ensure that it is only a single frequency – any broadband emission to long wavelengths of the laser emission line represent serious interfering signals because they can mimic fluorescence. Lasers, in particular diodes, often emit multiple frequencies, so a filter should be placed in the excitation path to prevent leakage of any long-wavelength light from the excitation laser directly into the emission pathway.

All the above sources of noise (B and D) can be eliminated or minimized, but shot noise on the detected molecule photons will always be present, due to the particle nature of light. Shot noise shows up as $1/\sqrt{N}$ scaling in Equation 2.1 if B and D are negligible. Since shot noise can never be eliminated, the SNR has a fundamental value dependent upon the number of photons collected.

Despite the limited number of total photons from single molecules and the limitations arising from the various contributions to the SNR, single-molecule imaging and spectroscopy is feasible in a confocal microscope if care is taken when building the optical setup.

2.2.4 Time-Correlated Single Photon Counting

When the laser spot is placed on a single-molecule, confocal microscopy allows for the measurement of the single molecule's excited state lifetime through Time-Correlated Single Photon Counting (TCSPC). Since confocal microscopy is often implemented with a high speed detector like an APD, each photon that is received on the detector can be time-tagged with down to 50ps precision (for example by using a Micro Photon Devices PDM series APD in conjunction with a Picoharp 300). This time-tagging ability is very useful in fluorescence microscopy, because now quantities like the time spent by the molecule in the excited state (excited state lifetime), fluctuations, and antibunching can be directly observed. Figure 2-1 shows how this time-tagging can be used to measure a single-molecule's excited state lifetime using a pulsed excitation laser. By using a pulsed laser, the molecule is excited at regular intervals, so the precise time the molecule is excited is known (blue

lines in Figure 2-2). Signal photons are detected by the APD and the time of photon detection can be referenced to the last measured pulse from the laser – this is called the time delay. Each photon's time delay can be measured and this corresponds to the amount of the time the molecule spent in the excited state before emitting a photon. In Chapter 3, this method is used to produce time-delay histograms for SMs in order to tease out the excited state lifetime of a molecule and show how it is affected by a bowtie nanoantenna.

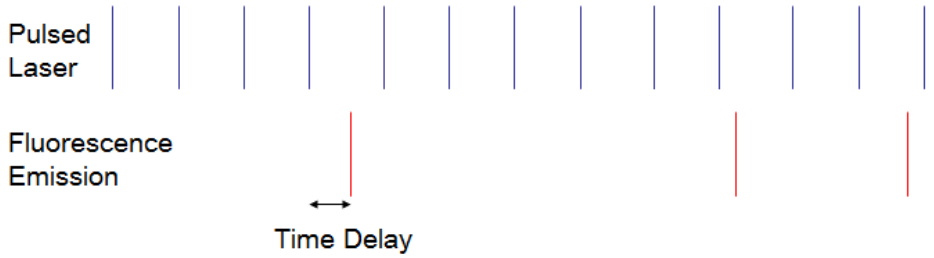

Figure 2-2: Time tagging of photons is accomplished by measuring the time delay between a signal photon and the sync signal of a pulsed laser.

2.3 Scattering Microscopy

2.3.1 Introduction

Measuring the amount and wavelength of light that is scattered by a structure is essential for plasmonics research. Plasmonic structures have resonances whereby they concentrate light, but only at specific wavelengths that are dependent upon the material and shape of the structure. Scattering measurements are often used to directly measure the plasmonic resonance of a nanostructure by illuminating the nanostructure with white (broadband) light. The light scattered by the structure is collected and

dispersed onto a spectrometer (alignment can be found in Appendix C). Since the primary scattering signal is elastic and therefore at the same wavelength as the exciting light, long pass filters cannot be used to discriminate between the two as is done in traditional fluorescence microscopy. Instead, scattering measurements are usually based upon methods which spatially separate the pumping light from the scattered light such as dark-field microscopy or total internal reflection (TIR) microscopy the latter of which is used here. Snell's law governs how light reflects off of a boundary and in particular predicts TIR, since it shows that beyond a critical angle of incidence at a boundary between two materials of different indices, all of the light is reflected:

$$\sin\theta_c = \frac{n_t}{n_i} \qquad [2.2]$$

where n_i and n_t are the indices of refraction for the two materials at the boundary and θ_c is the angle beyond which all light will be reflected back into the first material[8]. The TIR method described below was used for measuring the plasmon resonance for gold bowtie nanoantennas using scattering.

2.3.2 Optical Setup

The optical setup for measuring scattering is relatively simple as seen in Figure 2-3. White light is taken from a tungsten lamp and sent through a polarizer in order to achieve S-polarization of the excitation light, perpendicular to the plane of incidence, i.e., perpendicular to the plane of the figure. The light is also sent through a lens (L1 in Figure 2-3), which focuses the light down to a smaller spot on the sample. This is

not a diffraction-limited focal spot, it just reduces the beam size to approximately 1mm diameter. Note that a large area of the sample is illuminated by the excitation light, so the confocal emission pathway is used to ensure only 1 structure is measured at a time.

The key to this scattering setup is the use of a dove prism that is index matched to the glass substrate upon which the sample is fabricated. When light enters the dove prism, it is directed down onto the sample at an angle that ensures TIR off of the substrate glass-air interface. TIR ensures that the only light that is collected by the objective is light that has been scattered by some structure on the glass-air interface, such as the bowtie in Figure 2-3 (yellow squares viewed from the side). The scattered signal is then collected through a confocal emission beam path (Figure 2-1b). If the signal is sent onto an APD and the sample is scanned, a confocal image of the scattering signal can be formed, so that a particular object of interest can be found, but then the light must be directed onto a spectrometer to measure spectral information about the scattering signal.

Tungsten lamps are black body emitters and thus have a wavelength dependence of their emission. This means that the sample is not uniformly illuminated in frequency space, so a background spectrum must be obtained to normalize the scattering data. Background spectra can often be taken by just measuring light leakage at a bare spot on the sample that is slightly rough (e.g. at a spot with no bowtie) and normalizing the scattering data to the background spectrum.

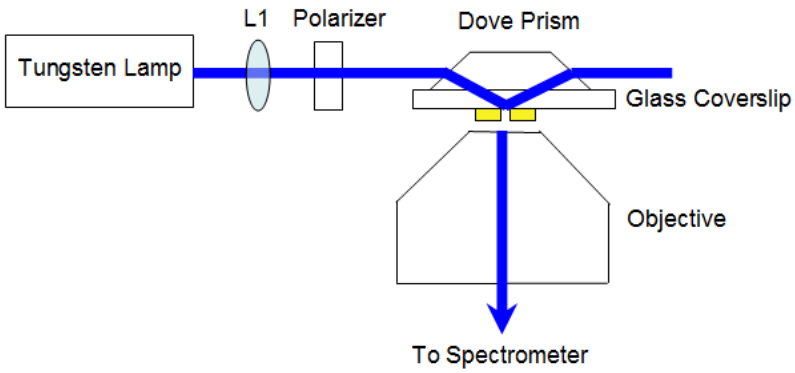

Figure 2-3: Schematic of TIR optical setup used to measure scattering from plasmonic structures.

As seen above, this scattering setup is based upon a traditional fluorescence microscopy pathway. A simple excitation pathway is used above the sample plane to ensure TIR and all that is needed is a confocal microscope with a spectrometer in order to sensitively measure the scattering spectrum from individual plasmonic nanostructures.

2.4 Nanofabrication Techniques

2.4.1 Introduction

Nanotechnology has become a popular field of study partially because of the new techniques available to fabricate and characterize nanostructures. Electron Beam Lithography and Focused Ion Beam Milling will be discussed in this section as well as in Appendices A-B.

2.4.2 Electron Beam Lithography

Electron Beam Lithography (EBL) has been used for over 50 years to fabricate micron and nanometer scale structures[8]. The basic process consists of defining the pattern using a focused electron beam to expose resist, followed by a development step which removes the exposed resist. The patterned resist can then be used as a mask for material deposition or etching. Finally, the resist is removed, leaving behind only the patterned material. This chapter specifically details the steps necessary to make bowtie nanoantennas using EBL on both conducting and insulating substrates in the Stanford Nanofabrication Facility (SNF).

Figure 2-4 shows the process flow for fabricating gold bowtie nanoantennas onto a conductive substrate (Indium Tin Oxide, ITO). In step 1, a square quartz coverslip (Esco) is cleaned by rinsing in acetone then plasma etching in Argon for 5 minutes. Tom Carver in the Ginzton cleanroom facility then deposits a 50 nm thick layer of ITO, usually in batches of 20 coverslips. Next, a 50-60nm thick layer of poly(methyl methacrylate) (PMMA) is spun onto the substrate at SNF using the Laurel spin coater. To spin the resist, ~1 mL of 2% 950k PMMA (Microchem) in anisole is pipetted onto the coverslip surface through a 450nm pore size filter. The Laurel spin coater can be programmed to spin the coverslip at 3 speeds. To achieve 60nm thick PMMA films, 2% PMMA in anisole is first spun for 10s at 300RPM, then 40s at 6,000RPM, and finally 10s at 300RPM. Resist films of varying thickness can be calibrated by first spinning onto Silicon pieces at different speeds and measuring the final thickness using SNF's Nanospec film thickness measurement tool. Once the

resist is spun, the coverslip is placed onto a 180°C hot plate for >2 minutes to bake out the resist and ensure the sample does not outgas under vacuum.

Now that the coverslip is coated in resist, the sample is loaded into SNF's Raith 150 for e-beam exposure (Step 2). An abbreviated set of instructions for defining bowties using the Raith 150 can be found in Appendix A, but this machine requires a week long training course in order to use. In step 2, the sample is loaded into the Raith 150 and the electron beam is aligned, so that it is in focus and stigmated properly. This alignment ensures that the electron beam is focused to the smallest spot possible, allowing the user to define the smallest gap bowties possible (~10nm reproducibility). The resist that is exposed to the electron beam becomes more soluble than the unexposed resist in methyl isobutyl ketone (MIBK), which important for the development step.

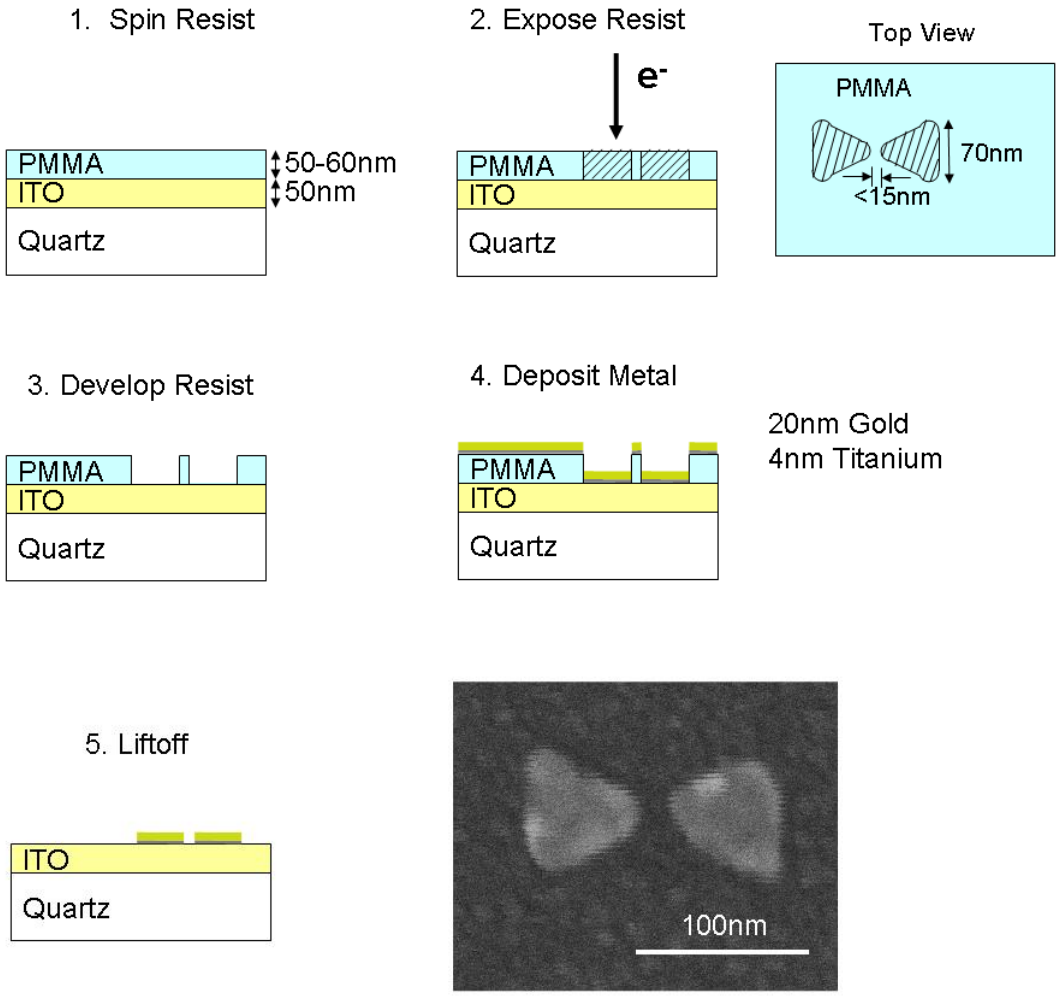

Figure 2-4: Process Flow for E-beam Lithography of Bowtie Nanoantennas onto conductive substrate. 1. Deposit 50nm thick layer of the transparent conductive oxide, Indium Tin Oxide (ITO), onto a quartz coverslip. Spin 50nm of PMMA using Laurel spincoater. 2. Expose bowtie pattern into resist using Raith 150 E-beam writer. 3. Develop exposed resist in 1:3 MIBK/IPA solution for 35s and rinse in IPA for 40s. 4. Deposit 4nm Titanium as a sticking layer and 20nm Gold. 5. Liftoff remaining PMMA by sonicating sample in acetone for a few seconds, leaving behind bowtie nanoantennas.

Step 3 is developing the exposed resist. The sample is removed from the Raith 150 and developed by soaking it in a 1:3 solution of MIBK:IPA for 35s and subsequently soaking in a pure IPA solution for 40s to prevent further development. Since PMMA is a positive resist, this step removes the exposed resist and leaves behind bowtie-shaped holes in the resist. Negative e-beam resists do exist and they become less soluble during the development step, and would leave behind bowtie shaped pillars of resist. Positive resists, in particular PMMA, performs better for smaller feature sizes (<20nm), so is used for all bowtie nanoantenna fabrication.

Once development has finished, the metallization step begins (Step 4). In this step, Tom Carver deposits a 4nm titanium layer followed by a 20nm gold layer. The titanium layer is necessary as a sticking layer between the gold and ITO. In Figure 2-4, it can be seen that the bowties are now adhered to the ITO, but there is still unwanted gold remaining. The final step, liftoff (Step 5), removes this unwanted gold by sonicating the sample in acetone to dissolve the remaining underlying PMMA, removing the leftover Ti/Au layer with it. The sample is sonicated until all the excess gold is removed, which can be seen by eye. Usually this requires only a few seconds, but it can sometimes take a minute to complete.

If it is not possible to fabricate bowtie nanoantennas on a conductive substrate, then a slightly different technique is necessary to perform EBL. As seen in Figure 2-5, the first step now consists of first spinning a 50-60nm thick layer of PMMA, baking, then depositing a 4nm layer of chrome (chromium metal). This thin layer of chrome prevents the sample from charging during the electron beam exposure in step 2. After exposure, the chrome layer is then removed in step 3 using Chrome etchant (Cyantek

CR-14), exposing the PMMA surface. The sample is then developed (Step 4), metal is deposited (Step 5), and finally liftoff (step 6) is performed as described previously. Most importantly, this process does not require ITO deposition, so it can be performed on top of any flat substrate. Note that after fabrication is complete, the sample is insulating, so scanning electron microscopy (SEM) imaging is not possible without depositing another thin metal layer.

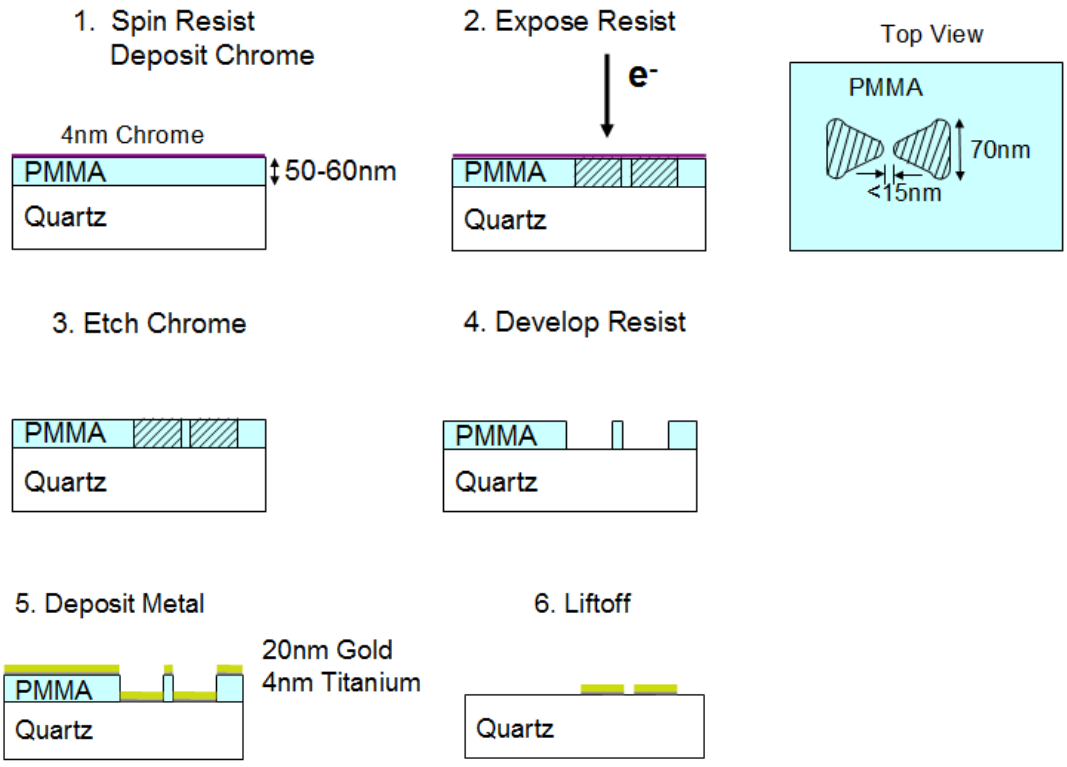

Figure 2-5: Process Flow for E-beam Lithography of Bowtie Nanoantennas onto insulating substrate. 1. Spin 50nm of PMMA using Laurel spincoater. Deposit thin layer (4nm) of Chrome to make sample temporarily conductive. 2. Expose bowtie pattern into resist using Raith 150 E-beam writer. 3. Remove Chome in Chrome etch (Cyantek CR-14). 4. Develop exposed resist in 1:3 MIBK/IPA solution for 35s and rinse in IPA for 40s. 5. Deposit 4nm titanium as a sticking layer and 20nm gold.

6. Liftoff remaining PMMA by sonicating sample in acetone for a few seconds, leaving behind bowtie nanoantennas.

E-beam lithography is a very useful, clean technique for fabricating nanostructures, but it does take time to master fully. Once a process has been developed, such as the bowtie process described above, bowtie nanoantennas can be routinely and precisely fabricated. Focused Ion Beam (FIB) milling will be discussed later and should be considered as an easier approach to fabricating nanostructures when the Ga^{2+} implantation inherent to FIB milling is acceptable.

2.4.3 Float Coating EBL Resist

Float coating[9] is a useful technique for coating uneven substrates (such as AFM tips and photonic crystal cavities described in this thesis) with thin layers of PMMA for EBL, optical experiments, or other purposes. Spin coating is the usual method for coating flat substrates with thin layers of PMMA, but it fails when the surface is uneven (Figure 2-6), due to buildup of resist around uneven features.

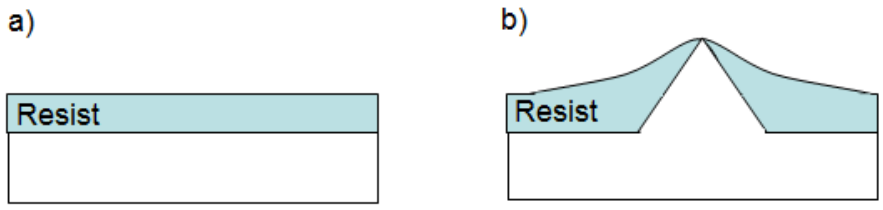

Figure 2-6: A) Spin coating resist onto a flat substrate yields a smooth, even layer. B) Spin coating onto an uneven substrate leads to uneven coverage and buildup of resist at the base of features.

Float coating is outlined in Figure 2-7. The first step is to place the uneven substrate (pictured as an AFM tip) into a Petri dish filled with water on top of a silicon wafer piece. The silicon piece should be significantly lager than the sample, but also smaller than the petri dish, so that when the silicon piece is moved, the sample can be moved within the petri dish. In step 2, 1 drop of a 1% PMMA solution in toluene is dropped onto the surface of the water bath. The drop of polymer solution disperses on the water surface in step 3. The water bath should not be disturbed during this process to ensure the smoothest film possible. Solvent choice is critical – a 1% PMMA in anisole solution was found to ball up and not disperse evenly over the surface, but a 1% PMMA in toluene solution does spread evenly. The molecular weight of the PMMA was not found to significantly affect results. The sample should be left for 5 minutes to let the film form fully and for the toluene to evaporate. Next, the water is pipetted out of the dish to allow the film to fall gently onto the substrate (step 4). The film is usually visible on the surface due to large wrinkles in the surface. In fact, the film is uneven over the entire surface on large spatial scales, but I've found that the film is locally very uniform over 100μm distances. For this reason, the thickness of the final film cannot be controlled well and 10nm-100nm thick films will be deposited with the same solution. If the process is performed several times or on different samples, then eventually an acceptable thickness will be deposited. Finally, in step 5 the substrate is heated at 90°C for 30 minutes in order to bake out the remaining water that could not be pipetted away. Note that this baking step is longer and at a lower temperature than the baking step for spin coating (180°C for 2 minutes). The temperature needs to be lower because the melting point for PMMA is 140-150°C. If

the PMMA-coated uneven substrate is heated above the melting point, then the PMMA may run down the sides of the uneven features. Baking is still important to remove excess water, particularly to protect the EBL machine from outgasing samples, so the longer, lower temperature bake is necessary if EBL is to be performed, but may be skipped for other experiments.

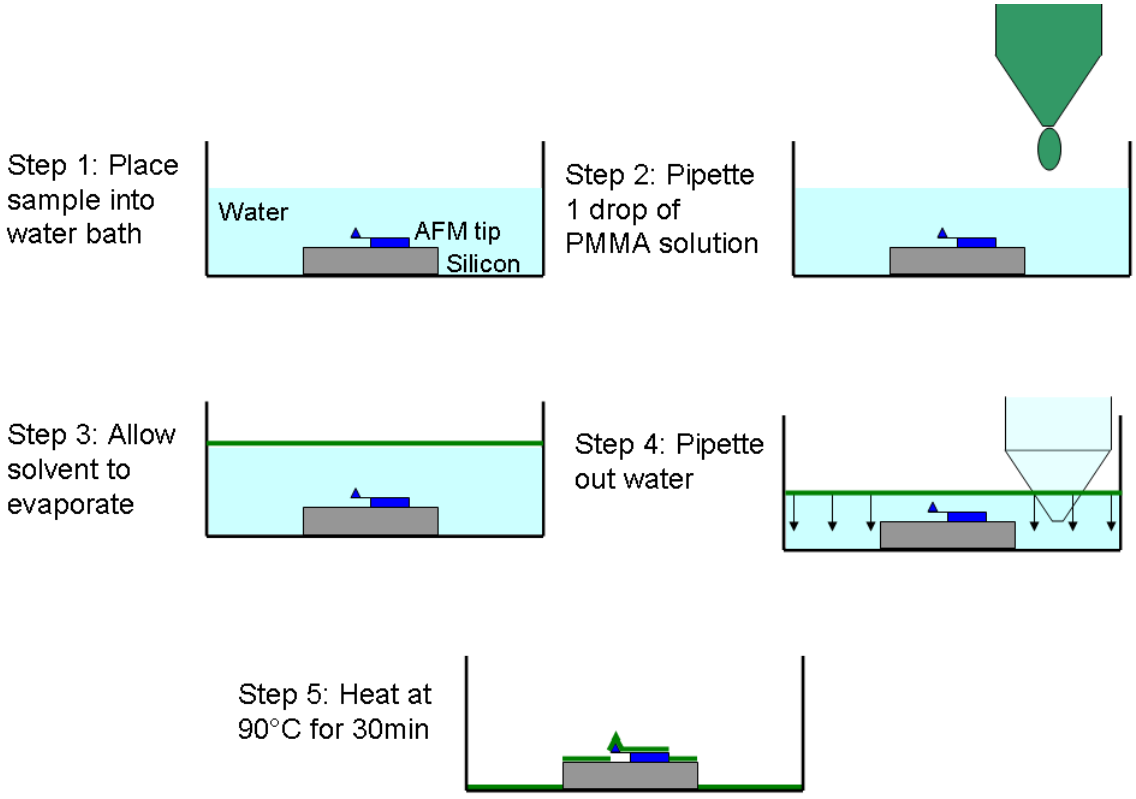

Figure 2-7: Float Coating resist onto uneven substrate (AFM tip). Step 1: Place sample (AFM tip pictured) on top of a silicon piece in a water bath. Step 2: Drop 1 drop of 1% PMMA in toluene onto the water bath using a 100µL pipette tip. Step 3: Allow drop to disperse on top of water bath's surface for 5 minutes, so that thin PMMA film forms and toluene evaporates completely. Step 4: Pipette out water using 1000µL pipette tip. Pipette out water far away from the sample and push the Silicon piece to reposition the sample if necessary. Step 5: Place in 90°C over for 30min to bake out remaining water. Sample is now covered in thin layer of PMMA and can be removed from silicon piece.

2.4.4 Focused Ion Beam Lithography

The Focused Ion Beam (FIB) milling method was first developed in 1975[10, 10]. The FIB machine operates in much the same way as the E-beam lithography systems, but instead of shooting electrons at the surface, it shoots Ga^{2+} ions. In each technique, a focused beam of either ions or electrons is scanned over a sample to form a pattern. In E-beam lithography, the electrons act to expose resist and in this way define a pattern for etching or deposition. FIB lithography differs in that the ions themselves ablate the material so that it can be sculpted in real-time, which eliminates the need for resist. Appendix B is a detailed instruction manual for operating the FEI Strata in the Stanford Nanocharacterization Laboratory (SNL). The following discussion focuses only on strategies necessary for milling very small features.

There are several sample requirements to consider before choosing FIB lithography for a project. First, FIB lithography, as in EBL, requires a conductive sample. This can be achieved for insulating samples by coating the sample with a thin conductive layer, such as a 4nm thick layer of Chrome. After the FIB milling is complete, the chrome can be selectively removed by soaking the sample in Chrome Etchant CR14 for a few seconds. Secondly, the sample should not be magnetic; otherwise the high-resolution SEM mode (UHR mode) of imaging will pull the sample off of the sample holder and potentially scratch the E-beam lens.

If the sample fulfills the above requirements, then the effect of Gallium implantation on the sample's performance must be carefully weighed. FIB

lithography often uses focused Ga^{2+} ions in order to ablate material, but this process also implants significant amounts of Ga^{2+} into the sample surface. There may even be some implantation into the unmilled edges of the nanostructure due to scattering of the Ga^{2+} ions. For this reason, it is not recommended to use excessive FIB lithography for plasmonic antennas. It has been shown that moderate enhancements of fluorescence can be achieved with FIB lithography antennas[11, 12] and that using FIB lithography to mill apertures is also reasonable since such a small dose of Ga^{2+} is necessary[13, 14], but overall, EBL should be used whenever possible.

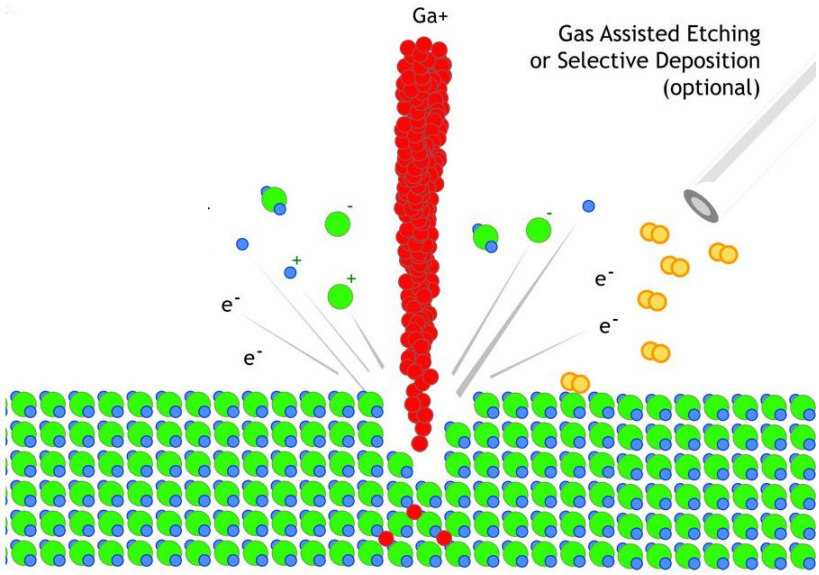

Figure 2-8: Schematic of FIB milling. A beam of ions is focused onto the surface and material is ablated away. Notice that Gallium ions (red circles) become implanted deep within the sample. Alternatively, if a gas is introduced into the system, such as a platinum precursor gas, the ions can act to deposit platinum instead of ablate the surface. This allows for controlled deposition of a metal or dielectric, but there will still be significant gallium implantation. Figure from [8].

2.5 Apertureless Near-Field Optical Microscopy

2.5.1 Introduction

As discussed in Chapter 1, in apertureless near-field optical microscopy (ANSOM), a plasmonic structure, often a metal coated Atomic Force Microscopy (AFM) tip, is optically excited while raster-scanning in direct contact with a sample surface. The plasmonic structure acts to concentrate light beyond the diffraction limit, which ultimately allows for sub-diffraction limited imaging. This section will describe the basics of AFM and ANSOM for use with bowtie nanoantennas fabricated onto AFM tips.

2.5.2 Atomic Force Microscopy

Atomic Force Microscopy (AFM) was invented by Binning, Quate, and Gerber in 1986[15], as a way to study the topography of any surface non-destructively. For a relatively recent technique, AFM has become central to characterizing many nanoscale structures and many modalities have beed discussed, such as working in fluids, sensing magnetic fields, sensing charges, and deposition by dip-pen lithography to name a few. This section only briefly discusses the main aspects of AFM necessary to understand ANSOM.

In the simplest AFM experiment, running in contact mode, a sharp tip is brought into contact with the sample surface (Figure 2-9). The tip is then dragged across the sample surface (either by scanning the tip or the sample) in order to track the topography of the surface. Tip deflections are measured by bouncing a laser off of

the back of the cantilever and onto a quadrant photodiode. By subtracting the signal from the bottom half of the photodiode from the top half, the tip deflection can routinely be measured to nm accuracy in the Z direction. X and Y resolution is dependent on the sharpness of the AFM tip and is often limited to ~10nm. Recently, however, it was shown that AFM is sensitive enough to resolve the atoms of a single pentacene molecule[10], making it a useful Å–level precision tool.

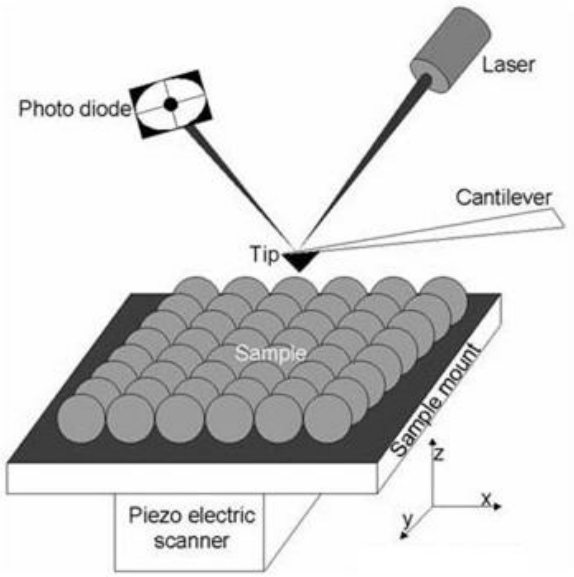

Figure 2-9: Schematic for typical AFM experiment. A cantilever with a sharp AFM tip is scanned over a sample surface. Nanometer-scale tip deflections from the sample surface are measured by reflecting a laser off of the back of the AFM tip and onto a quadrant photodiode, which senses different intensities based on the tip deflection. Figure from Ref. [10].

2.5.3 Apertureless Scanning Near-field Optical Microscope Setup

A typical ANSOM setup has two main components: an AFM head and a confocal optical pathway. I have used a commercial setup called the Topometrix Lumina that combines an inverted optical microscope with an AFM head where the

sample stage can be precisely scanned in X and Y with closed loop ositioning accuracy. This device is no longer sold, as Topometrix was purchased by Thermomicroscopes and then by Veeco. A simplified schematic of the setup is shown in Figure 2-10. For full detail on how to use this setup, see the detailed users' manual. For ANSOM, the main idea is that an AFM tip that has been modified to have a plasmon resonance (either by a metal coating or by lithographically fabricating a plasmonic antenna on top) is put in contact with a transparent substrate containing emitters to be studied (either fluorophores or Raman-active molecules). The tip is then aligned such that it is centered on the diffraction-limited confocal spot of the objective (~400nm in diameter for near-IR light). This alignment between the AFM tip and objective is the most important, and often most difficult, part of ANSOM. Single-molecule emission is collected through the same objective as the excitation light. The majority of the fluorescence signal will originate from the concentrated spot of light. Plasmonic tips have been shown to concentrate the light down to 10nm[10, 10]. By raster-scanning the sample, a near-field image is made of the surface and its resolution is only limited by the concentration of light by the tip (~10nm) not the diffraction limit (~400nm).

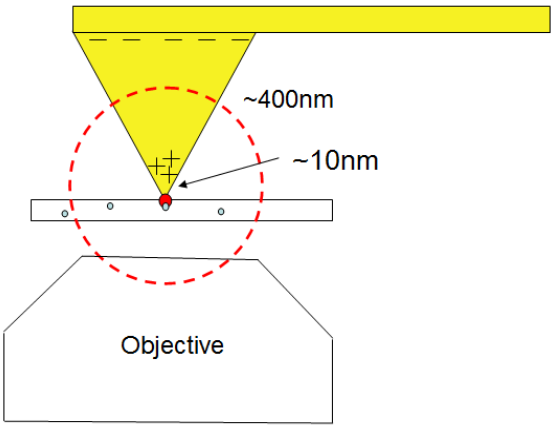

Figure 2-10: Schematic of a typical ANSOM experiment. A metal-coated AFM tip is excited with light. The light is concentrated down to ~10nm due to the plasmon resonance of the structure, which means the resolution of the imaging system is also ~10nm. Emission from the sample is collected back through an objective into a standard confocal emission pathway.

References

1. Davidovits, P., Egger, M. D. Scanning Laser Microscope for Biological Investigations. *App Optics* **10**, 1615 (1971).

2. Pawley, J. B. in *Handbook of Biological Confocal Microscopy* (ed Pawley, J. B.) 988 (Plenum Press, New York, 1995).

3. Corle, T. R. & Kino, G. S. in *Confocal Scanning Optical Microscopy and Related Imaging Systems* (Academic Press, San Diego, 1996).

4. Moerner, W. E. & Fromm, D. P. Methods of Single-Molecule Fluorescence Spectroscopy and Microscopy. *Rev. Sci. Instrum.* **74**, 3597-3619 (2003).

5. Lounis, B. L., Deich, J., Rosell, F. I., Boxer, S. G. & Moerner, W. E. Photophysics of DsRed, a red fluorescent protein, from the ensemble to the single-molecule level. *J. Phys. Chem. B* **105**, 5048-5054 (2001).

6. Soper, S. A., Nutter, H. L., Keller, R. A., Davis, L. M. & Shera, E. B. The Photophysical Constants of Several Fluorescent Dyes Pertaining to Ultrasensitive Fluorescence Spectroscopy. *Photochem. Photobiol.* **57**, 972-977 (1993).

7. Lakowicz, J. R. in *Principles of fluorescence spectroscopy* 954 (Springer Science, New York, 2006).

8. http://www.fibics.com/fib/tutorials/introduction-focused-ion-beam-systems/4/.

9. Zhou, H. *et al*. Lithographically Defined Nano and Micro Sensors using "Float Coating" of Resist and Electron Beam Lithography. *J. Vac. Sci. Technol. B* **18**, 3594 (2000).

10. http://sahussain.wordpress.com/2007/11/03/can-we-see-the-atomic-dimension/.

11. Farahani, J. N. *et al*. Bow-tie optical antenna probes for single-emitter scanning near-field optical microscopy. *Nanotech* **18**, 125506-125510 (2007).

12. Farahani, J. N., Pohl, D. W., Eisler, H. -. & Hecht, B. Single Quantum Dot Coupled to a Scanning Optical Antenna: A Tunable Superemitter. *Phys Rev Lett* **95**, 017402-1-017402-4 (2005).

13. Matteo, J. A. *et al*. Spectral analysis of strongly enhanced visible light transmission through single C-shaped nanoapertures. *Appl. Phys. Lett.* **85**, 648-650 (2004).

14. Taminiau, T. H., Stefani, F. D., Segerink, F. B. & van Hulst, N. Optical Antennas Direct Single-Molecule Emission. *Nat. Phot.* **2**, 234-237 (2008).

15. Binnig, G., Quate, C. F. & Gerber, C. *Phys. Rev. Lett.* **56**, 930 (1986).

Chapter 3 - Large Single-Molecule Fluorescence Enhancements Produced by a Bowtie Nanoantenna

The research reported in this chapter has been previously published in A. Kinkhabwala, Z. Yu, S. Fan, Y. Avlasevich, K. Müllen, and W. E. Moerner, "Large Single-Molecule Fluorescence Enhancements Produced by a Bowtie Nanoantenna," *Nature Photonics* **3**, 654-657 (2009) (published online, October 18, 2009).

3.1 Introduction

Due to the size mismatch between light and nanoscale objects like single molecules, it is important to be able to control light-molecule interactions[1-4]. Plasmonic nanoantennas create highly enhanced local fields when pumped resonantly leading to increased Raman scattering[5], but whether fluorescence enhancement occurs depends upon a variety of factors. While sharp metal tips[6] and colloids[7, 8] can enhance fluorescence, the highly enhanced optical fields of lithographically fabricated bowtie nanoantennas[9] provide a structure that is more controllable and can potentially be integrated. Using gold bowties, we have observed enhancements of a single molecule's fluorescence up to 1340x, an order of magnitude higher than reported previously[7, 8, 10, 11-22]. Electromagnetic simulations reveal that this is due to greatly

enhanced absorption and an increased radiative emission rate, resulting in enhancement of intrinsic quantum efficiency calculated to be a factor of 9 times, despite additional nonradiative Ohmic effects from currents induced in the metal. Bowtie nanoantennas thus show great potential for high-contrast selection of single nanoemitters.

3.2 Experimental Schematic

A single fluorescent molecule (SM) with transition dipole $\vec{\mu}$ acts as a nanoscale optical sensor of the local field $\vec{E}$ near a bowtie nanoantenna because its transition rate is proportional to $|\vec{\mu}\cdot\vec{E}|^2$, while its emission can either couple to the far field via the nanoantenna or quench via Ohmic losses[23, 24]. Low quantum efficiency emitters have been noted to have much higher potential fluorescence brightness enhancements (f_F) than high quantum efficiency emitters, because their intrinsic quantum efficiency has greater potential to be improved by the antenna's presence[25, 26].

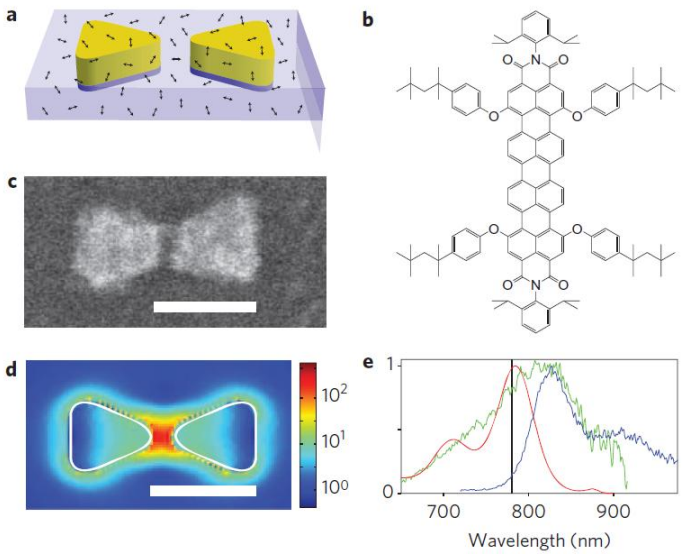

Figure 3-1: Enhanced fluorescence experimental outline (a) Schematic of bowtie nanoantenna (gold) coated with TPQDI molecules (black arrows) in PMMA (light blue) on a transparent substrate. (b) TPQDI molecular structure. (c) SEM of Au bowtie nanoantenna, bar 100 nm. (d) FDTD calculation of local intensity enhancement, bar 100 nm. (e) Red/blue: absorption/emission spectra of TPQDI in toluene. Green: Scattering spectrum from bowtie shown in (c) measured as in Ref.[30]. Black line: laser excitation wavelength. (After Ref. [31])

Bowtie nanoantennas were fabricated in gold using electron-beam lithography (Raith 150) onto 50 nm thick indium tin oxide (ITO) coated quartz coverslips. Experimental measurements of f_F for a SM were performed by coating electron-beam fabricated gold bowtie nanoantennas with the relatively low fluorescence quantum efficiency (η_i~2.5%) but solubilized near-IR dye N,N´-Bis(2,6-diisopropylphenyl)-1,6,11,16-tetra-[4-(1,1,3,3-tetramethylbutyl)phenoxy]quaterrylene-3,4:13,14-bis(dicarboximide) (TPQDI) doped in a thin poly(methyl methacrylate) (PMMA) layer (Figure 3-1a). TPQDI was doped into 1% wt/vol of 75k MW PMMA (Polysciences Inc.) in distilled toluene and spun onto the bowtie sample at 2500x RPM to achieve a

final thickness of 30 nm. In addition to its low quantum efficiency, TPQDI (Figure 3-1b) was chosen for the overlap of its absorption and emission spectra with the measured bowtie plasmon scattering resonance (Figure 3-1e).

3.3 Confocal Imaging of Unenhanced Single Molecules

In order to measure the enhancement of fluorescence from a molecule coupled to a bowtie nanoantenna, the fluorescence expected from an unenhanced molecule must first be determined. A 780 nm diode laser was used to excite fluorescence from TPQDI in a PMMA film in a confocal microscope. Appropriate excitation and emission filters ensured that only TPQDI fluorescence reached the avalanche photodiode (APD) photon-counting Si detector. Figure 3-2a shows a confocal fluorescence scan from a dilute TPQDI concentration (<1 molecule/diffraction-limited spot) in PMMA without bowtie nanoantennas. Essentially all fluorescent molecules irreversibly photobleach after a certain number of excitation cycles due to photodegradation (e.g., photo-oxidation), so each spot in the image was observed until single-step digital photobleaching occurred (Figure 3-2b) to ensure it corresponded to a single unenhanced TPQDI molecule. Each molecule's dipole moment is randomly oriented with respect to the linear excitation field polarization, causing each spot to emit with a different brightness. The brightest molecules have their dipole moments aligned along the excitation polarization. Each SM spot was fit to a 2D Gaussian to find the molecule's spatially integrated detected photons above background, and only molecules that had intensities >60 counts/10 ms when exited with 79 kW/cm^2 were

considered (201 molecules). Figure 3-2c is a histogram of the measured fluorescence from these unenhanced single molecules. To estimate the photon emission rate expected from an unenhanced molecule with its dipole moment aligned along the polarization axis, the emission rates of the brightest 5 were averaged together yielding 190 expected fluorescence photons per 10 ms for 79 kW/cm^2 excitation.

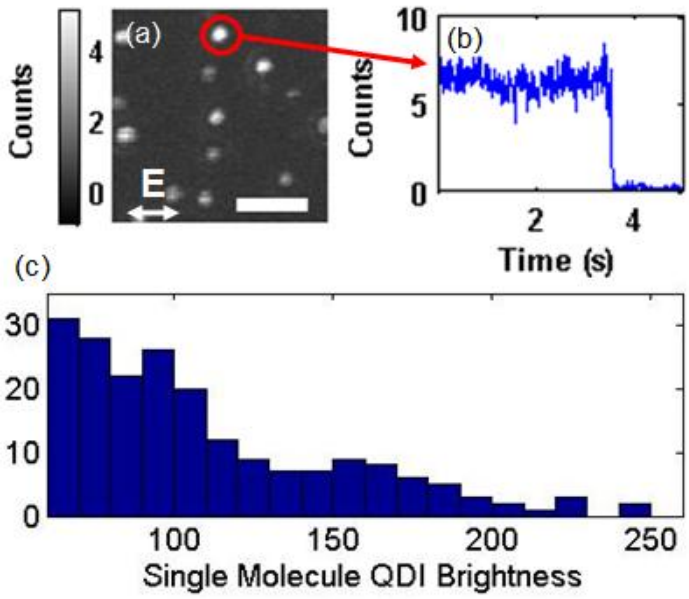

Figure 3-2: Imaging unenhanced single-molecule fluorescence (a) Confocal fluorescence scan of a low concentration (<1 molecule/diffraction limited spot) sample of TPQDI in PMMA without bowtie nanoantennas (scale bar = 4 μm). (b) Fluorescence time trace of a single unenhanced TPQDI molecule aligned along the excitation polarization axis. Data collected with 79 kW/cm^2, then scaled for direct comparison with Figure 3-3b. (c) Histogram of unenhanced single molecule TPQDI brightness values from same low concentration TPQDI doped PMMA sample. Data collected with 79 kW/cm^2 . (After Ref. [31])

3.4 Single-Molecule Fluorescence Measurements on Bowtie Nanoantennas

After fluorescence from unenhanced molecules was characterized, we proceeded to measure fluorescence from molecules enhanced by gold bowtie nanoantennas. Figure 3-3a shows a confocal scan from an array of 16 bowties coated with a high concentration of TPQDI in PMMA (~1,000 molecules/diffraction limited spot or ~3 molecules/(10 nm)^2). This image required a far lower pumping intensity than Fig. 3-2a. In order to see a SM out of the many covering the bowtie, the fluorescence as a function of time is shown in Figure 3-3b. Discrete blinking and eventual photobleaching of 50% of the total signal can be attributed to a single molecule's dynamics and reveal that half of the fluorescence from this particular bowtie is due to a single molecule! In other words, the digital (step-like) sudden drop near 293 s is an unambiguous signature that a single molecule photobleached, and the step size shows its contribution to the total signal, S_{bowtie}. While the exact position and orientation of this molecule is not known, it is highly likely that the molecule is located fairly near the position of maximum field enhancement, i.e., between the two triangle tips, discussed further below. The fluorescence enhancement factor f_F for this SM was determined with the following formula:

$$f_F = \frac{S_{bowtie} \cdot P_{un}}{S_{un,\,max} \cdot P_{bowtie}} \qquad [3.1]$$

where S_{bowtie} and P_{bowtie} are the SM fluorescence signal and laser excitation power used for Figure 3-3a, while $S_{un,max}$ and P_{un} apply to Figure 3-2a. At later times, a different single molecule could often be observed to photobleach, enabling measurement of its

f_F factor, and so on, on the same bowtie. In effect, the single molecules randomly sample the possible enhancements that can occur for various positions and orientations near the bowtie, and the distribution of values will be discussed below.

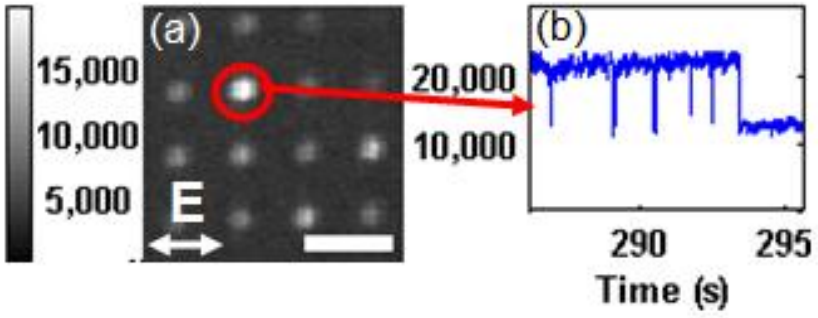

Figure 3-3: Measuring enhanced fluorescence from single molecules on bowtie nanoantennas. (a) Confocal scan of 16 bowties coated with high concentration (~1,000 molecules/diffraction limited spot) TPQDI in PMMA collected with 2.4 kW/cm^2 (scale bar = 4μm). (b) Fluorescence time trace of TPQDI/PMMA coated bowtie nanoantenna shown in Fig. 1c. Blinking dynamics and eventual photobleaching are due to 1 molecule that has been enhanced by a factor of 1340. (After Ref. [31])

As is well-known, the local field enhancement is highly dependent on the bowtie gap size. E-beam lithography produces a distribution of bowtie gap sizes, even when using the same lithographic pattern. After all optical data were obtained, scanning electron microscope (SEM) images were taken to measure the precise gap size of every bowtie. Figure 3-4a shows histograms of the actual bowtie gap sizes for all bowties used in this study and shows that approximately equivalent numbers of 10-25 nm, 40-60 nm, and 65-90 nm gap bowties were used, allowing for a gap dependence of the enhancement to be ascertained.

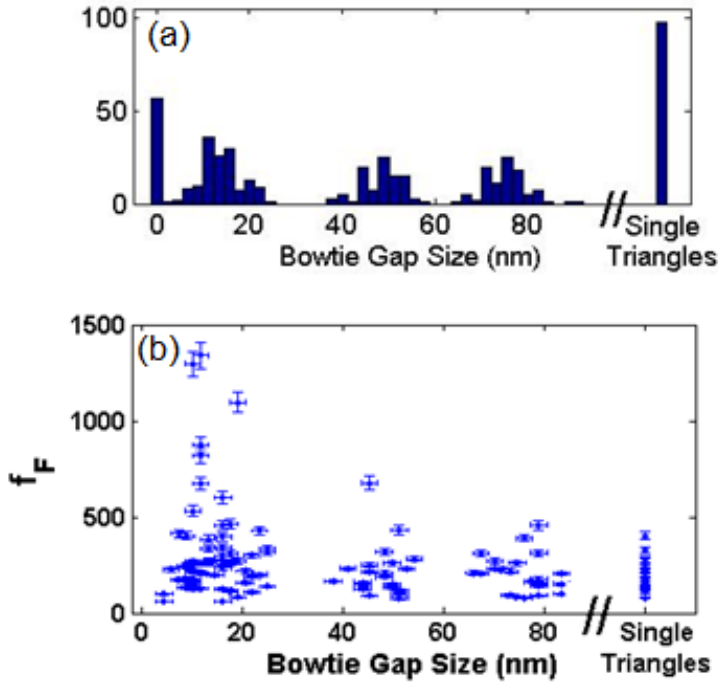

Figure 3-4: Measurement of f_F for SMs as a function of bowtie gap size. a) Histogram of gap sizes of all bowties measured. b) Scatter plot of 129 SM fluorescence brightness enhancements, f_F, as a function of bowtie gap size for all bowties measured in (a). (After Ref. [31])

Confocal scans were taken of each array of similarly sized gap bowties and the 5 brightest spots in any array were measured as a function of time to look for highly enhanced molecules as determined by significant single photobleaching steps. Figure 3-4b is a plot of the f_F values measured for 129 single molecules as a function of bowtie gap size. The smallest gap bowties yielded the highest f_F's, up to a factor of 1340, consistent with smaller gap bowties having higher local field strengths than larger gap bowties and single triangles. Of course, broad distribution of f_F values occurs because not all molecules are optimally located.

3.5 Finite Difference Time Domain Simulations

As shown above, the bowtie nanoantennas enhance single-molecule fluorescence an order of magnitude more than any other reported plasmonic structure to my knowledge. Fluorescence can be enhanced both in both by increases in absorption and in emission, so in order to understand this system, finite difference time domain simulations were used to simulate these enhancements. First, the absorption of light by a molecule is proportional to $|E|^2$, as also shown in Figure **3-5**a. Thus, the enhancement of the absorption of light f_E is simply the change in the squared field strength (or optical intensity) due to the plasmonic antenna:

$$f_E = \frac{\left|E_{metal}\right|^2}{\left|E_{inc}\right|^2} \qquad [3.2]$$

The bowtie nanoantenna has been shown to locally enhance $|E|^2$ up to a factor of 1,000, which corresponds to the maximum expected value for f_E. The change in $|E|^2$ will be calculated below for a molecule located in the precise center of the bowtie's gap, which we believe to be the position of highest enhancement, and for molecules located at different z positions.

The change in emission of a molecule coupled to a nanoantenna is more complicated than the case for the change in excitation. Figure **3-5**a shows that once the molecule is excited from the ground (S_0) to the excited (S_1) state, there are fast, non-radiative vibrational relaxation pathways (black wavy arrow) to the lowest excited state. At this point the molecule effectively waits to relax to the ground state. It can either decay radiatively and emit a photon (red emission pathway, γ_r), or it can decay non-radiatively by creating high-order vibrations or phonons (black emission pathway,

γ_{nr}). When a plasmonic antenna is placed near the emitter, the picture changes (Figure **3-5**b). Now, the radiative pathway is not simply emission into free space, but rather the emitter is coupling to the plasmonic antenna and then the antenna is emitting a photon into free space (γ_r'). Plasmonic antennas, however, are lossy (Ohmic losses) at optical wavelengths, so once the emitter couples to the antenna, the antenna could just lose energy by Joule heating from resistive currents (γ_{nr}'). Finally, the non-radiative pathways intrinsic to the molecule, even without the plasmonic antenna, are still present, so they must also be included (γ_{nr}).

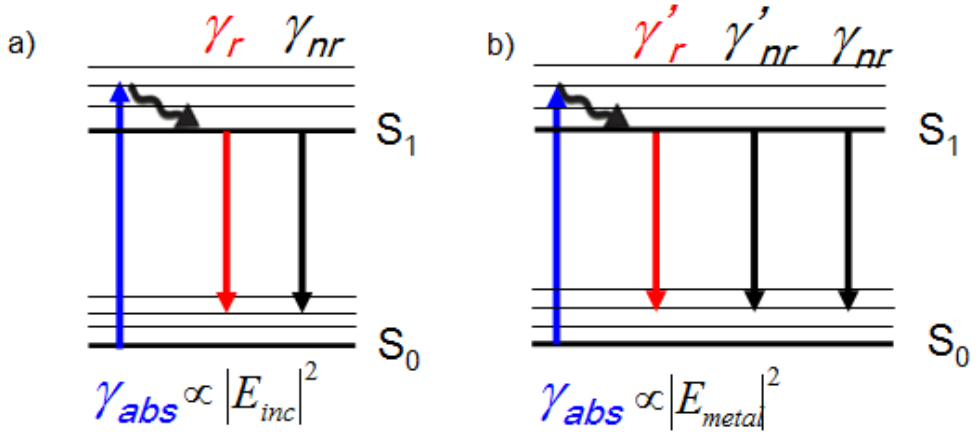

Figure 3-5: Jablonski diagrams for fluorescence transition near and away from a plasmonic antenna. a) Jablonski diagram for a fluorescence transition in a two-level system without a plasmonic antenna. The blue arrow shows absorption of light - rate of absorption of light (γ_{abs}) is proportional to the incident electric field squared ($|E_{inc}|^2$). For emission, the radiative and non-radiative pathways from the excited state must be considered. b) Jablonski diagram for fluorescence transition of a two-level system coupled to a plasmonic antenna. Absorption of light is still proportion to $|E|^2$, but now the electric field is modified by the antenna to become E_{metal}. The emission pathways have also been modified. There are now 3 classes of pathways, one radiative and two non-radiative to consider.

Since the radiative and non-radiative pathways are changing, the quantum efficiency (QE) of the molecule must be calculated. For a molecule in free space, the intrinsic QE is:

$$\eta_i = \frac{\gamma_r}{\gamma_r + \gamma_{nr}} \quad [3.3]$$

while the QE for a molecule coupled to an antenna is:

$$\eta' = \frac{\gamma'_r}{\gamma'_r + \gamma'_{nr} + \gamma_{nr}} \quad [3.4]$$

After some simple algebra, the enhancement (or quenching) of the QE from a single molecule coupled to an antenna becomes:

$$f_\eta = \frac{\eta'}{\eta_i} = \frac{\gamma'_r / \gamma_r}{1 - \eta_i + \eta_i \left(\gamma'_r / \gamma_r + \gamma'_{nr} / \gamma_r \right)} \quad [3.5]$$

It is not immediately obvious whether a molecule's QE will be enhanced or quenched by analyzing this equation alone, so finite difference time domain simulations were used to calculate the changes in the radiative and non-radiative rates of a molecule located in the center of a bowtie's gap in order to use in Equation 3.5.

Simulations of a single molecule coupled to a gold bowtie nanoantenna by Zongfu Yu used a custom three-dimensional finite difference time domain (FDTD) method developed in the Fan laboratory to solve Maxwell's equations. The frequency-dependent refractive index of gold and titanium were modeled by a fit to tabulated experimental data[27] using the method of complex-conjugate pole-residue pairs[28].

To simulate the excitation process, plane waves polarized in the x-direction are incident from SiO_2 side. The optical intensity enhancement factor driving increased absorption rate, f_E, is then obtained by comparing the electric field intensity with and without the metallic bowtie. Figure 3-6a shows the spectrum of f_E at the center of the antenna gap region (10 nm above ITO layer). At a wavelength of 780 nm, the enhancement is $f_E = 181$ in the center of the bowtie gap, while the maximum field enhancement occurs closer to the two gold tips (Figure 3-1d).

For simulation of the emission process, we place a point current source in the gap region. In the presence of the bowtie antenna, the radiated power, P_r, into the far field and the power dissipated in the metal, P_{nr}, are calculated. The enhancement factors are then obtained by normalization with respect to the radiated power P_0 of the same point current source in the absence of the antenna. As a result, for a point current source polarized in the x-direction at the center of the gap emitting at 820 nm, the radiative enhancement factor is

$$f_r \equiv \frac{\gamma'_r}{\gamma_r} = \frac{P_r}{P_0} = 187 \qquad [3.6]$$

and the non-radiative enhancement factor is

$$f_{nr} \equiv \frac{\gamma'_{nr}}{\gamma_r} = \frac{P_{nr}}{P_0} = 577 \qquad [3.7]$$

as seen in Figure 3-6d,e. These two ratios can be used in equation 3.5 in order to estimate the change in QE, f_η, due to the bowtie's presence. Figure 3-7a plots the

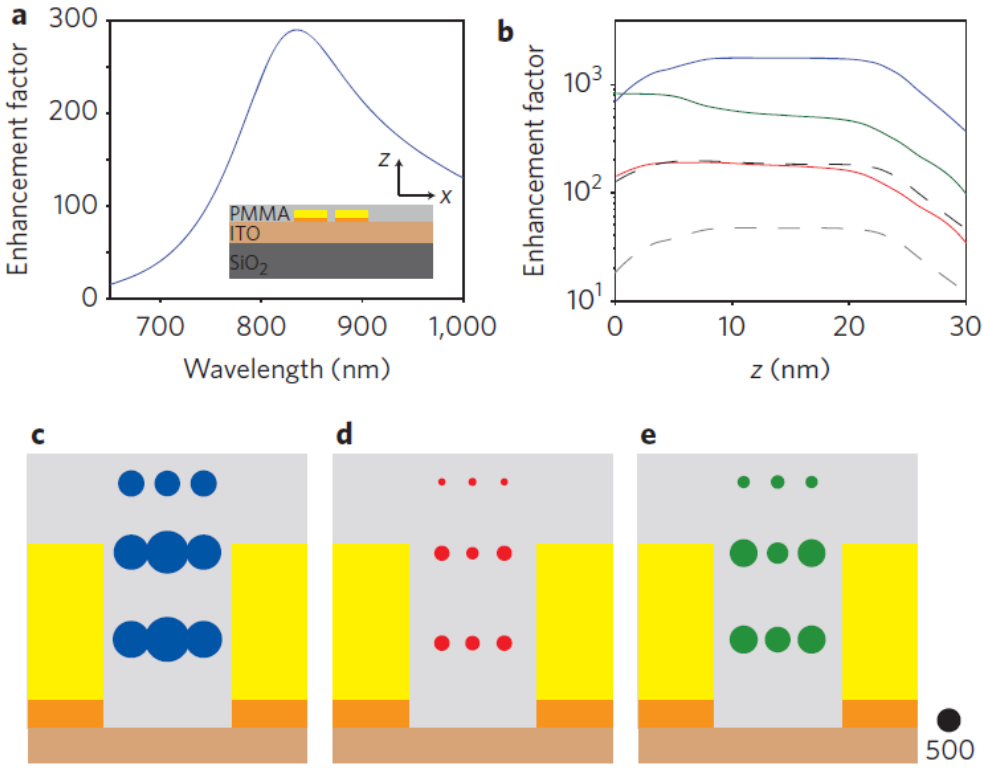

Figure 3-6: Electromagnetic simulations of SM fluorescence near a gold bowtie nanoantenna (a) Spectrum of calculated electric field intensity enhancement *versus* wavelength in the center of a bowtie with 14 nm gap. Inset: the simulated structure (side view) consists of a SiO_2 (refractive index n=1.47) substrate, a 50 nm layer of ITO (n=2), and a 30 nm layer of PMMA (n=1.49). The gold bowtie structure is 20 nm thick on a 4 nm layer of titanium. (b) Radiative (red) and non-radiative (green) enhancement factors along the center of the gap for wavelength 820 nm. *z* measures the distance above the ITO/PMMA interface. Black dashed line shows the enhancement factor for electric field intensity at 780 nm. Blue curve shows the fluorescence enhancement factor for quantum efficiency 2.5% molecules and grey dash line for quantum efficiency 100% molecules. (c-e) Illustration of the simulated structure (side view, section through the two triangle tips) showing regions of fluorescence (Blue), radiative (Red) and non-radiative (Green) enhancement factors for a molecule emitting at 820 nm wavelength. . (After Ref. [31])

bowtie-modified QE versus the intrinsic QE . Notice that if a molecule with η_i=100% is used, then the quantum efficiency is actually quenched to η'=25%, but if a molecule with η_i = 2.5% to 25% in used, then the bowtie modified quantum efficiency is enhanced to the same η' = 25%. The QE enhancement factor is plotted directly in Figure 3-7b. Notice that for molecules with η_i > 25%, the QE is quenched, while for molecules with lower QE, there is significant enhancement. If the intrinsic QE is too low, however, the modified QE may have a large QE enhancement (f_η), but it will have a low final QE (η_i'). The optimal QE to balance these two effects is η_i ~ 2%. This means that the emission from high QE molecules cannot be enhanced, so by choosing a relatively low QE molecule, higher overall fluorescence enhancements can be achieved.

Based on the simulations above one can estimate the total fluorescence enhancement factor (f_F):

$$f_F = f_E f_\eta \qquad [3.9]$$

For a molecule located in the gap of the bowtie, the absorption enhancement is calculated to be f_E = 180. As shown above, the emission or quantum efficiency enhancement depends upon intrinsic quantum efficiency and for TPQDI (η_i = 2.5%) is calculated from Equation 3.5 to be f_η = 9.3. Taking these two factors into account in Equation 3.9 yields a predicted total fluorescence enhancement ratio f_F = 1690.

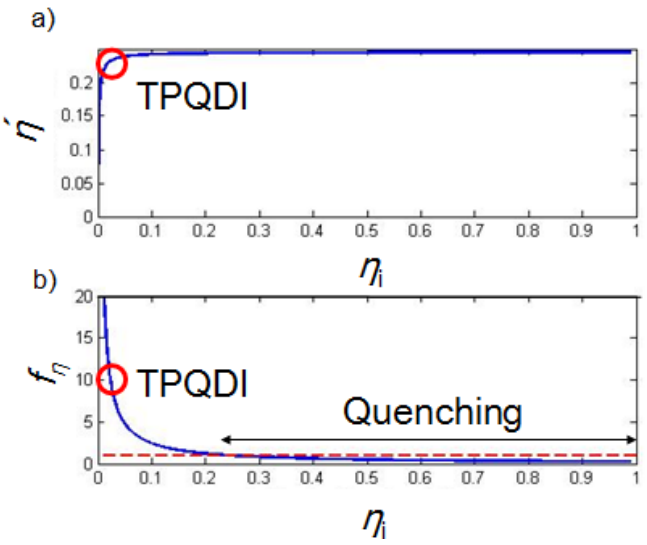

Figure 3-7: Modeled enhancement of QE as a function of intrinsic QE. a) Theoretical predictions based on FDTD simulations for the change in intrinsic quantum efficiency (η_i) when a molecule is placed near a bowtie nanoantenna (η'). The FDTD simulations provide f_r and f_{nr}, and the curves show the values of Eqn. 3.5. b) Same data as in (a), this time plotting enhancement of quantum efficiency against the intrinsic quantum efficiency . In both figures, TPQDI's intrinsic quantum efficiency (η_i = 2.5%) is circled in red. (After Ref. [31])

This number is in good agreement with the maximum experimentally measured enhancement factor of 1340, especially if one takes into account the experimental uncertainty in determining the exact location and orientation of the molecule. Figure 3-6 also shows the enhancement factors at different positions. In the vertical direction (z-direction), the functions are relatively constant in the gap region and fall off quickly above the metal surface (Figure 3-6b). In the gap region, the maximum total fluorescence enhancement occurs at the center (Figure 3-6c), and decreases closer to the metal tips because of lower quantum efficiencies from increased Ohmic losses (cf. Figure 3-6d, radiative, and Figure 3-6e, nonradiative). The same analysis above

indicates that a molecule with a high intrinsic quantum efficiency (e.g. $\eta > 25\%$) in fact would not have any quantum efficiency enhancement by the same antenna and thus will have much lower f_F (cf. blue vs. grey dashed in Figure 3-6b).

3.6 Excited State Lifetime Measurements

The discussions above suggest that the enhancement of quantum efficiency should also produce a change in the SM total decay lifetime, τ_F. To probe the enhanced molecules' excited state lifetimes, a mode-locked Ti:Sapphire laser (pulse length ~200 fs) was tuned to 780 nm and used in conjunction with a fast time resolution APD (MPD PDM-100 series) as well as a time-correlated single-photon counting analyzer (Picoharp 300) to measure total decay lifetime. In order to measure τ_F for a SM on a bowtie despite the presence of background fluorescence from other molecules, a special procedure was implemented. Key to the scheme is the fact that all fluorescence photons from the molecule-coated bowtie were time-tagged. A typical binned time trace of these time-tagged photons is seen in Figure 3-8a. The black line in Figure 3-8a shows the time interval where the enhanced molecule is emitting, while the red line indicates the time interval when the molecule has blinked off. In both time intervals, all other molecules are also emitting, but they are assumed to not change and thus represent a constant background. Time delay histograms are formed based on the fluorescence photons before (black in Figure 3-8b) and after (red in Figure 3-8b) a single-molecule photobleaching step. The algebraic difference in shape of these two time delay histograms is the single molecule's time delay histogram (blue in Figure 3-8c). Notice that this particular single-molecule's time

delay histogram completely overlaps with the instrument response function (IRF, green in Figure 3-8c). This overlap means that the molecule was emitting from the excited state too fast for the APD to resolve its lifetime. If the lifetime is longer than 10 ps, then deconvolution of the measured instrument response function (IRF) allowed extraction of the lifetime from the data.

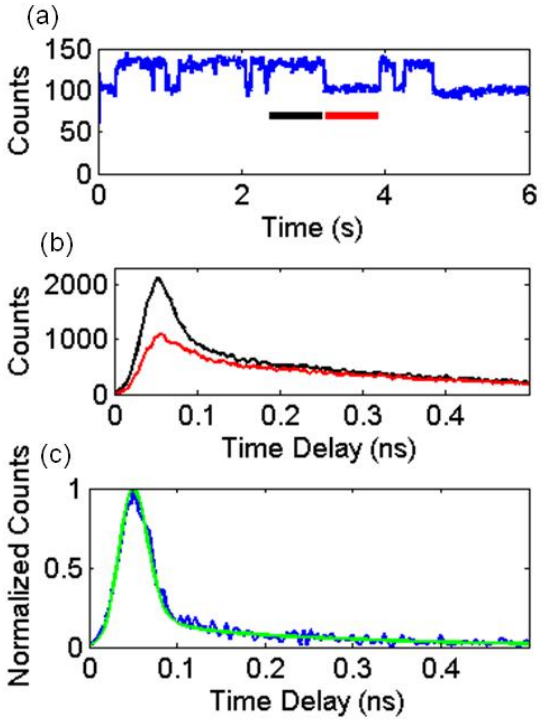

Figure 3-8: Measuring excited state lifetime from a single molecule coupled to bowtie nanoantenna. a) Time trace of fluorescence from a single bowtie nanoantenna. Black and red lines indicate times before and after one molecule photobleaches. b) Time delay histograms from time trace in (a) corresponding the before (black) and after (red) photobleaching step. c) Blue – Normalized single-molecule time delay histogram formed by subtracting the red from the black curves in (b). Green is the instrument response function. The deconvolved lifetime for this curve was less than 10 ps, the minimum value we were able to determine experimentally. (After Ref. [31])

Compared to measurements of f_F, changes in τ_F only monitor changes in nonradiative and radiative processes but not changes in the absorption rate. The

magenta curve in Figure 3-9a shows the fluorescence from bulk TPQDI in PMMA and yields τ_F = 275 ps for molecules not coupled to a bowtie. The green curve in Figure 3-9a corresponds to a SM with τ_F = 78 ps, while the red curve corresponds to a different SM with τ_F < 10ps. The red molecule, therefore, has a > 28x decrease in τ_F, but this is due to changes in both the molecule's radiative and nonradiative rates. Figure 3-9b is a scatter plot of SM decay lifetime versus f_F for 73 molecules. At low f_F, both small and large τ_F were observed in the data (but all much smaller than the uncoupled value in magenta). This result is expected since τ_F depends only upon the radiative and nonradiative rates while f_F depends in addition upon local optical intensity, and many combinations are possible for different molecule positions and orientations. To achieve high f_F, the molecule's absorption and quantum efficiency must be significantly improved, and this occurs only in the gap where both the radiative and nonradiative rates are faster, which yields a greatly shortened lifetime. Therefore, only short lifetimes are to be expected for high f_F molecules, as observed in Figure 3-9b.

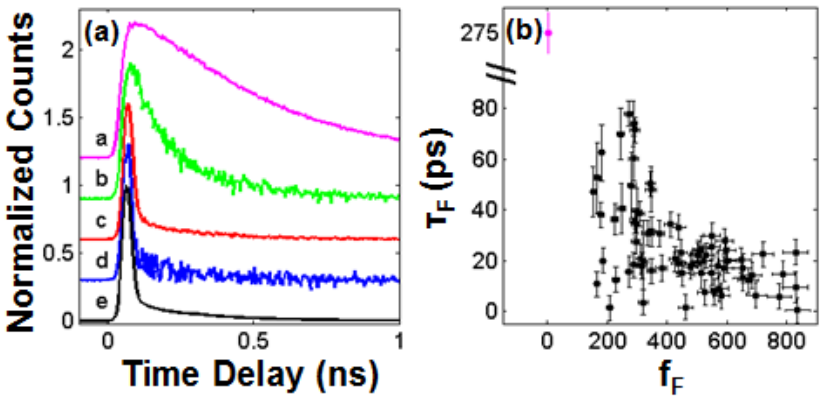

Figure 3-9: Enhanced single-molecule fluroescence time delay histograms. (a) Magenta – bulk TPQDI in PMMA without bowtie nanoantenna. Green – SM on bowtie nanoantenna, f_F = 271, lifetime

78 ps. Red/blue – SM on bowtie nanoantenna, excitation polarization parallel/perpendicular to long axis. Black – instrument response function. (b) Black - Scatter plot of decay lifetime versus brightness enhancement for 73 SM's of TPQDI on bowtie nanoantennas. Magenta – Bulk TPQDI lifetime without bowtie nanoantenna present. (After Ref. [31])

3.7 Excitation Polarization Dependence

Since the absorption and emission enhancements are decoupled, the polarization of the excitation light should affect the fluorescence brightness enhancement, which depends upon the absorption and emission enhancements, but not the SM decay lifetime, which only depends on the emission enhancement. By changing the excitation polarization using an electro-optic modulator every 1.5 s from parallel to perpendicular to the long axis of the bowtie (1 s for parallel, 0.5 s for perpendicular), fluorescence lifetimes of the same molecule as a function of excitation polarization can be measured. Figure 3-10a shows a fluorescence time trace from a bowtie nanoantenna, where red/blue indicated parallel/perpendicular excitation polarizations. At 21.5 s there is a significant photobleaching step in the parallel excitation polarization channel, while a much smaller drop in intensity can also be detected in the other channel. This demonstrates that the total fluorescence enhancement is higher for the parallel orientation, as expected. Since all of the photons are time-tagged, the fluorescence lifetime can be determined for each polarization. In Figure 3-9a, the red/blue curves is the SM time delay histogram for long/short axis excitation polarization, respectively, yielding f_F's of 854/68, while both curves fit to lifetimes shorter than the IRF. As expected, the lifetime for the single molecule measured does not depend on the excitation polarization while the total

fluorescence intensity drops much more sharply for the perpendicular (short axis) polarization. Figure 3-10b shows the same measurement for 20 more single molecules. Red symbols show long axis excitation polarization, while blue indicates short axis excitation polarization. The fluorescence brightness enhancement was measured to change by up to a factor of 16 with different excitation polarization directions, but the lifetime did not change significantly, verifying our general interpretation, even though the various molecules in the group had varying orientations relative to the bowtie long axis.

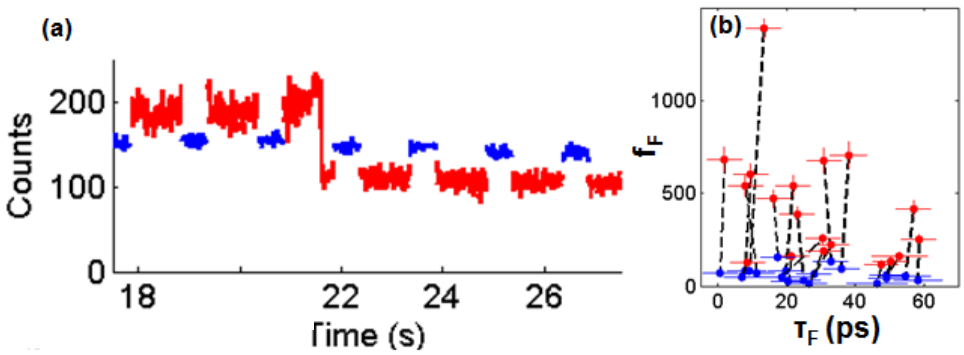

Figure 3-10: Polarization dependence of single-molecule enhanced fluorescence. a) Time trace for a single molecule with changing excitation polarization. The polarization is changed from parallel (red) to perpendicular (blue) orientations with respect to the long axis of the bowtie. Due to differences in dichroic reflectivity, the parallel orientation data were taken at 1.2 kW/cm^2, while the perpendicular data were taken at 5.9 kW/cm^2, but the parallel data is scaled here to 5.9 kW/cm^2 for easy comparison. b) Red/Blue – SM TPQDI excited with light polarized parallel/perpendicular to the long axis of the bowtie. Black dashed lines connect measurements from the same molecule. (After Ref. [31])

3.8 Conclusions

In this work, single molecules of TPQDI were used as probes of f_F near gold bowtie nanoantennas. Using the dominant emission that arises from the most highly

enhanced molecule, fluorescence brightness enhancements of up to 1340 were observed, in agreement with electromagnetic calculations of radiative, nonradiative, and electromagnetic intensity enhancements. SM lifetimes show additional information about the decay processes for each molecule, independent of the local optical intensity enhancement. The bowtie nanoantenna provides a useful balance between enhancement and loss for SM emission applications. In particular, emission decay times as short as 10 ps were observed, which means that a high-emission rate room temperature single-photon source[29] can be fabricated using a SM in a bowtie gap.

References:

1. Chance, R. R., Prock, A. & Silbey, R. J. Molecular Fluorescence and Energy Transfer Near Interfaces. *Adv. Chem. Phys.* 37, 1-65 (1978).
2. Muhlschlegel, P., Eisler, H., Martin, O. J. F., Hecht, B. & Pohl, D. W. Resonant optical antennas. *Science* 308, 1607-1609 (2005).
3. Fischer, H. & Martin, O. J. P. Engineering the Optical Response of Plasmonic Nanoantennas. *Opt Exp* 16, 9144-9154 (2008).
4. Grober, R. D., Schoelkopf, R. J. & Prober, D. Optical Antenna: Towards a Unity Efficiency Near-Field Optical Probe. *Appl. Phys. Lett.* 70, 1354-1356 (1997).
5. Willets, K. A. & Van Duyne, R. P. Localized Surface Plasmon Resonance Spectroscopy and Sensing. *Annu. Rev. Phys. Chem.* 58, 267-297 (2007).
6. Hamann, H. F., Kuno, M., Gallagher, A. & Nesbitt, D. J. Molecular fluorescence in the vicinity of a nanoscopic probe. *J. Chem. Phys.* 114, 8596-8609 (2001).
7. Anger, P., Bharadwaj, P. & Novotny, L. Enhancement and Quenching of Single-Molecule Fluorescence. *Phys. Rev. Lett.* 96, 113002 (2006).

8. Kuhn, S., Hakanson, U., Rogobete, L. & Sandoghdar, V. Enhancement of Single-Molecule Fluorescence Using a Gold Nanoparticle as an Optical Nanoantenna. *Phys. Rev. Lett.* 97, 017402 (2006).
9. Schuck, P. J., Fromm, D. P., Sundaramurthy, A., Kino, G. S. & Moerner, W. E. Improving the mismatch between light and nanoscale objects with gold bowtie nanoantennas. *Phys. Rev. Lett.* 94, 017402 (2005).
10. Farahani, J. N., Pohl, D. W., Eisler, H. -. & Hecht, B. Single Quantum Dot Coupled to a Scanning Optical Antenna: A Tunable Superemitter. *Phys Rev Lett* 95, 017402 (2005).
11. Farahani, J. N. *et al*. Bow-tie optical antenna probes for single-emitter scanning near-field optical microscopy. *Nanotech* 18, 125506-125510 (2007).
12. Tam, F., Goodrich, G. P., Johnson, B. R. & Halas, N. J. Plasmonic enhancement of molecular fluorescence. *Nano Lett.* 7, 496-501 (2007).
13. Taminiau, T. H., Stefani, F. D., Segerink, F. B. & van Hulst, N. Optical Antennas Direct Single-Molecule Emission. *Nat. Phot.* 2, 234-237 (2008).
14. Zhang, J., Fu, Y., Chowdhury, M. H. & Lakowicz, J. R. Metal-enhanced single-molecule fluorescence on silver particle monomer and dimer: Coupling effect between metal particles. *Nano Lett.* 7, 2101-2107 (2007).
15. Bakker, R. M. *et al*. Enhanced localized fluorescence in plasmonic nanoantennae. *Appl. Phys. Lett.* 92, 043101 (2008).
16. Muskens, O. L., Giannini, V., Sanchez-Gil, J. A. & Gomez Rivas, J. Strong Enhancement of the Radiative Decay Rate of Emitters by Single Plasmonic Nanoantennas. *Nanolett* 7, 2871-2875 (2007).
17. Brolo, A. G. *et al*. Surface plasmon-quantum dot coupling from arrays of nanoholes. *J. Phys. Chem. B* 110, 8307-8313 (2006).
18. Gerard, D. *et al*. Nanoaperture-enhanced fluorescence: Towards higher detection rates with plasmonic metals. *Phys. Rev. B* 77, 045413 (2008).
19. Ringler, M. *et al*. Shaping emission spectra of fluorescent molecules with single plasmonic nanoresonators. *Phys. Rev. Lett.* 100, 203002 (2008).

20. Bek, A. *et al*. Fluorescence Enhancement in Hot Spots of AFM-Designed Gold Nanoparticle Sandwiches. *Nano Lett* 8, 485-490 (2008).
21. Song, J. H., Atay, T., Shi, S. F., Urabe, H. & Nurmikko, A. V. Large enhancement of fluorescence efficiency from CdSe/ZnS quantum dots induced by resonant coupling to spatially controlled surface plasmons. *Nano Lett.* 5, 1557-1561 (2005).
22. Chen, Y., Munechika, K. & Ginger, D. Dependence of Fluorescence Intensity on the Spectral Overlap between Fluorophores and Plasmon Resonant Single Silver Nanoparticles. *Nano Lett* 7, 690-696 (2007).
23. Ruppin, R. Decay of an excited molecule near a small metal sphere. *J. Chem. Phys.* 76, 1681-1683 (1982).
24. Rogobete, L., Kaminski, F., Agio, M. & Sandoghdar, V. Design of plasmonic nanoantennae for enhancing spontaneous emission. *Opt Lett* 32, 1623-1625 (2007).
25. Khurgin, J. B., Sun, G. & Soref, R. A. Practical limits of absorption enhancement near metal nanoparticles. *Appl. Phys. Lett.* 94, 071103 (2009).
26. Sun, G., Khurgin, J. B. & Soref, R. A. Practical enhancement of photoluminescence by metal nanoparticles. *Appl. Phys. Lett.* 94, 101103 (2009).
27. Palik, E. D. in *Handbook of Optical Constants* (Academic Press, Orlando, 1985).
28. Han, M., Dutton, R. W. & Fan, S. Model dispersive media in finite-difference time-domain method with complex-conjugate pole-residue pairs. *IEEE Microw. Wirel. Comp. Lett.* 16, 119-121 (2006).
29. Lounis, B. & Moerner, W. E. Single Photons on Demand from a Single Molecule at Room Temperature. *Nature* 407, 491-493 (2000).
30. Fromm, D. P., Sundaramurthy, A., Schuck, P. J., Kino, G. S. & Moerner, W. E. Gap-dependent optical coupling of single "bowtie" nanoantennas resonant in the visible. *Nano Lett.* 4, 957-961 (2004).
31. A. Kinkhabwala, Z. Yu, S. Fan, Y. Avlasevich, K. Müllen, and W. E. Moerner, "Large Single-Molecule Fluorescence Enhancements Produced by a Bowtie Nanoantenna," *Nature Photonics* **3**, 654-657 (2009) (published online, October 18, 2009).

Chapter 4 – Fluorescence Correlation Spectroscopy at High Concentrations using Gold Bowtie Nanoantennas

4.1 Introduction

As shown in Chapter 3, gold bowtie nanoantennas are able to enhance a single-molecule's fluorescence by factors up to 1300[1]. So far, this property has only been demonstrated for molecules fixed in position and orientation in a thin polymer film. The goal of this chapter is to extend the polymer work to molecules in solution by immersing bowtie nanoantennas in a liquid containing a high concentration of fluorescent dye molecules and studying dynamics in the fluorescence signal from these molecules (Figure 4-1a). Importantly, I observed that fluorescence enhancement from single molecules transiently sticking to the ITO surface near the bowtie nanoantenna could be measured over the background of nearby molecules in solution within the laser pumping volume. This experiment shows that the bowtie produces extreme contrast enhancements and thus opens the way to future experiments where the sticky surface of our experiments is replaced with a surface of enzyme molecules or proteins with an affinity for fluorescent dyes. In this way, when biomolecules attached to the surface in the enhanced region of the bowtie nanoantenna incorporate

or bind fluorescently labeled substrate or ligand molecules, flashes of fluorescence will be measured until the fluorophore either photobleaches, is released by the enzyme or unbinds from the biomolecule. This experiment is analogous to experiments described in Chapter 1 using zero-mode waveguides to measure individual biological events such as DNA replication[2, 3] and RNA translation[4].

4.2 Experimental Schematic

The two fluorescent molecules used in this study are indocyanine green (Sigma-Aldrich), ICG, shown in Figure 4-1c, and IR800cw carboxylate (Li-cor), IR800cw, shown in Figure 4-1d. The absorption and emission spectra of the two dyes, shown in Figure 4-1b, overlap well with the plasmon resonance from a 10 nm gap Au bowtie nanoantenna, so the bowtie could potentially enhance absorption and emission from both molecules. From Table 1, the QE of ICG in water is 2.4%, but increases to 14% in ethanol. Considering the work in Chapter 3, this suggests that ICG will have higher fluorescence enhancement in water than in ethanol, but moderate fluorescence enhancement should still be expected in ethanol. Similarly, since the QE of IR800cw in ethanol is 28%, it should have an even lower maximum fluorescence enhancement.

Bowtie nanoantennas are fabricated on ITO coated glass substrates using E-beam lithography as described in Chapter 2. In order to immerse the bowties in concentrated solutions of dye molecules, a simple fluid cell is constructed from 2 coverslips, one with the fabricated bowtie nanoantennas on the surface and the other unstructured, and an o-ring sandwiched in between the coverslips. The coverslips and

o-ring were first cleaned in water and then ozone-cleaned for 10 minutes, before adding the concentrated dye solutions.

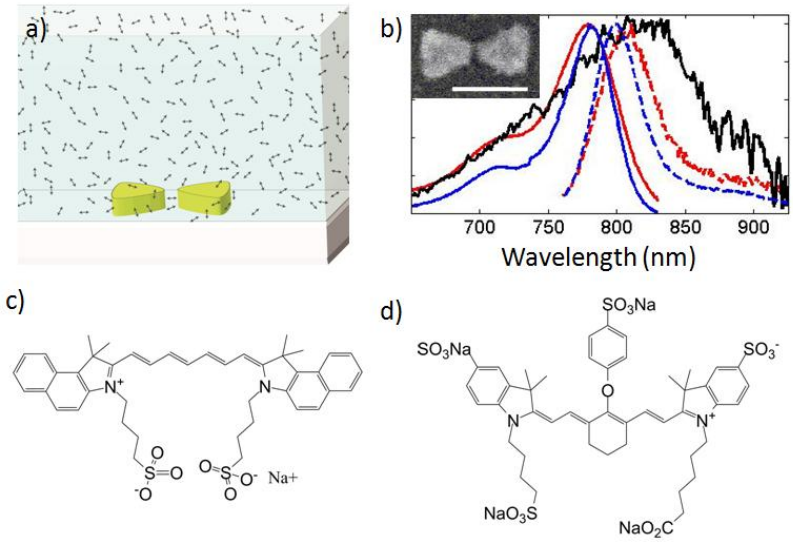

Figure 4-1: a) Bowtie nanoantennas are immersed in concentrated dye solutions for FCS experiments. b) Blue – absorption (solid) and emission (dashed) spectra of IR800cw in ethanol. Red - (solid) and emission (dashed) spectra of ICG in water. Black – plasmon resonance of a 10 nm gap Au bowtie nanoantenna. Measured as in Ref.[5]. Inset: SEM of a typical gold bowtie nanoantenna. Scale bar = 100 nm. c) ICG molecule. d) IR800cw molecule.

Dye	Solvent	Quantum Efficiency
ICG	Water	2.4%
ICG	Ethanol	14%
IR800cw	Water	10%
IR800cw	Ethanol	28%

Table 1: Table of quantum efficiencies (QE) for ICG and IR800cw in water and ethanol. Measurements used IR800 phosphoramidite (LiCor) in methanol, QE = 15%, as a QE reference.

4.3 Bulk Bowtie-Enhanced Fluorescence of Molecules in Solution

Confocal measurements of concentrated dye solutions on bowtie nanoantennas were performed using the confocal microscope described in Chapter 2. Figure 4-2c,f are confocal scans of IR800cw and ICG doped into 2% PVA in water solutions and spun to 30nm thick films on top of the bowtie surface. These images reveal that the bowtie nanoantennas do enhance bulk fluorescence from these two molecules in rigid environments, as was shown in Chapter 3 for TPQDI in PMMA. Therefore, these two molecules are good candidate molecules to look for enhanced fluorescence in solution.

Moving on to solution environments, at 1μM concentration there are only 0.6molecules/$(100nm)^3$ region. The bowtie's enhanced region is only ~$(20nm)^3$, but even so, it is easy to see fluorescence enhancement from bowties immersed in both ICG at 1μM concentration in water (Figure 4-2d) and IR800cw at 100nM concentration in ethanol (Figure 4-2a). It is as if the molecules linger longer in the enhanced region. In fact, the enhancement is actually due to molecules that are stuck to the substrate surface instead of floating in solution, as will be shown below with several key pieces experimental evidence. First, the concentration dependence suggests that the surface is nearly saturated with sticking molecules even at 100 nM concentration. To see this, one finds that fluorescence enhancement from bowties immersed in a 100μM solution of IR800cw in ethanol is only barely detectable. Under the assumption that the surface was already saturated with sticky molecules at 100nM concentration, by increasing the concentration to 100μM, only the background would increase, drowning out the enhanced fluorescence from enhanced molecules stuck to

the surface near the bowtie. Figure 4-2g enforces this point by plotting the amplitude of a Gaussian fit to 25 bowties immersed in various concentrations of IR800cw in ethanol divided by the background signal level (the signal-to-background ratio or S/B) and shows that S/B decreases steadily with increasing IR800cw concentration from 100nM to 100μM. One might wonder if the highly anisotropic and concentrated optical field of the bowtie is producing trapping by gradient forces, but this is not the case since when the optical intensity increases, the lingering time of molecules near the enhanced region drops. Finally, Figure 4-2e is an image of bowties immersed in a 1μM concentration of ICG in ethanol. While bowties submerged in ICG in water easily showed enhanced fluorescence (Figure 4-2d), this image shows that the effect disappears in ethanol. By using separate observations of the photobleaching behavior of molecules in the presence of an ITO-coated surface without bowties, ICG was found to stick to the ITO surface in water but not in ethanol (Figure 4-3), further supporting the conclusion that the enhanced signal is from a concentrated layer of molecules sticking to the ITO.

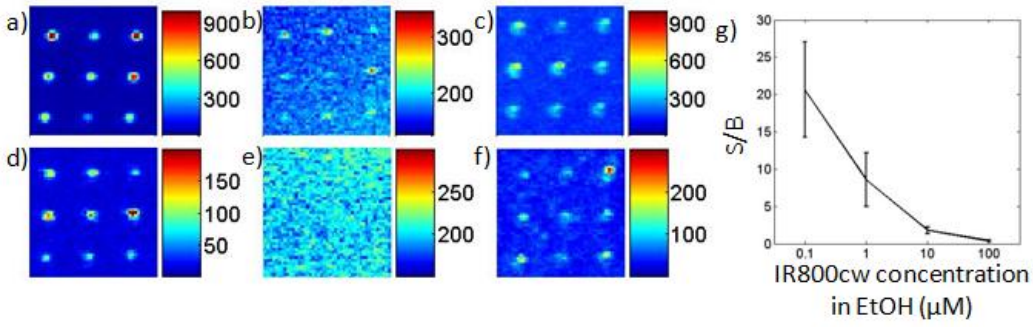

Figure 4-2: Confocal images of an array of bowties in the presence of a) 100nM IR800cw in ethanol, 109W/cm^2 imaging intensity, b) 100μM IR800cw in ethanol, 3W/cm^2 imaging intensity, c) 30nm thick PVA film doped with IR800cw, 36W/cm^2 imaging intensity, d) 1μM ICG in water, 1.2kW/cm^2

imaging intensity, e) 1μM ICG in ethanol, 600W/cm^2 imaging intensity, f) 30nm thick PVA film doped with ICG, 1.2kW/cm^2 imaging intensity. g) Signal to background ratio of bulk enhanced fluorescence from 25 bowtie nanoantennas and different IR800cw concentrations.

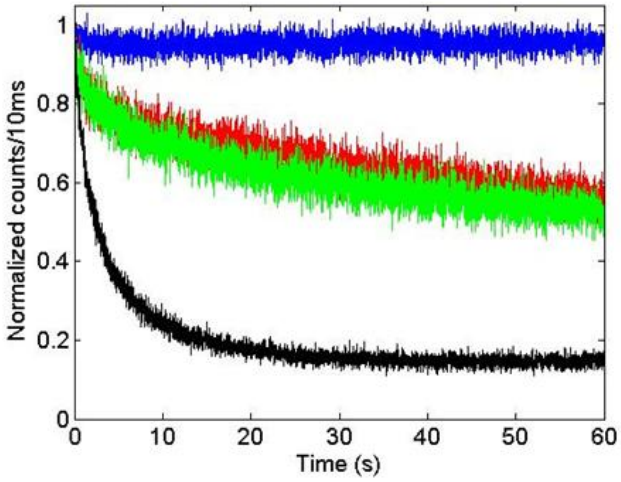

Figure 4-3: Photobleaching curves from cleaned ITO interfaces immersed in different dye solutions without bowties. Blue: 1μM ICG in ethanol. Red: 1μM ICG in water. Black: 1μM IR800cw in ethanol. Green: 1μM IR800cw in water. If photobleaching (drop in signal) is measured beyond the first 10ms bin, then molecules must be sticking to the surface and cannot be replaced, since molecules only remain in the focal volume for no more than 1ms , unless they are stuck to the surface. Therefore, the only solution that did not show sticking is ICG in ethanol.

4.4 Emission Spectra of Bowtie-enhanced Fluorescence

Fluorescence spectra were taken of both bulk and bowtie-enhanced fluorescent molecules with the same imaging power and integration time (Figure 4-4a). This required use of the confocal fluorescence microscope and imaging of the emission from the sample on the entrance slit of a grating spectrometer with a CCD array detector at the exit slit. The optical arrangement has been described in Ref. [6, 7]. The measured spectra are typical for room-temperature fluorescence measurements and do

not show sharp features typically associated with Raman transitions, which rules out SERS effects. As expected, the fluorescence spectra taken in the presence of the bowtie nanoantenna have much higher signal. In Figure 4-4b, the bowtie and no bowtie spectra for IR800cw are normalized in order to show that the shape of the fluorescence spectrum does not markedly change with the presence of the bowtie nanoantenna. In principle, plasmonic antennas can change the fluorescence emission of molecules coupled to them[8-13], but the bowtie's resonance is relatively broad and well matched to the molecules' emission spectra, so this does not occur.

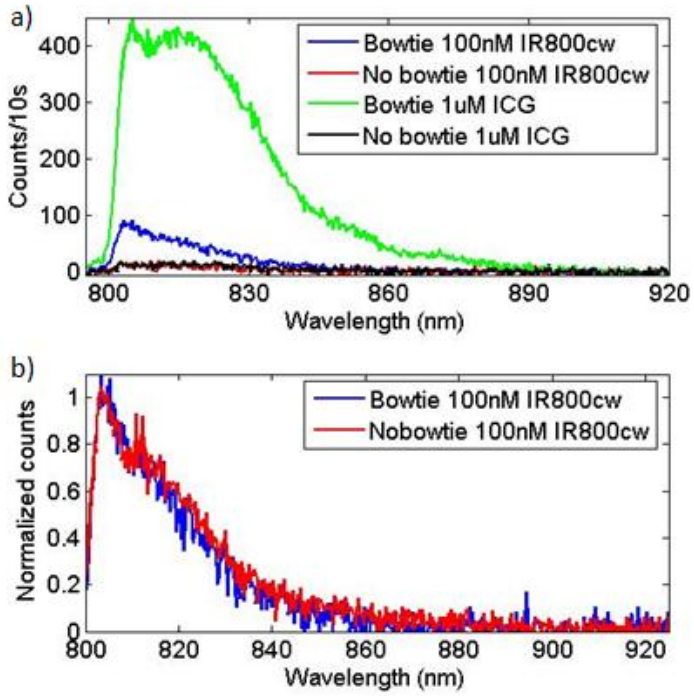

Figure 4-4: a) Spectra integrated over 10s from a 100nM concentration solution of IR800cw in ethanol with (blue) and without (red) a bowtie present, as well as spectra from a 1μM concentration solution of ICG in water with (green) and without (black) a bowtie present. Notice that none of the spectra contain Raman peaks. b) Normalized spectra from 100nM IR800cw with (blue) and without (red) a bowtie present. Notice that the shape of the spectrum does not change depending on the bowtie's presence or

absence. For both figures, the laser filter cuts off emission 800nm and shorter, causing aberrations in this spectral region, particularly at ~810 nm.

4.5 FCS of Low Concentration Dye Solutions

In a fluorescence correlation spectroscopy (FCS) experiment[14-17], the fluorescence emission from a low concentration dye solution irradiated by a focused laser beam is analyzed by calculating the autocorrelation function:

$$G(\tau) = \frac{\langle \delta I_1(t) \rangle \langle \delta I_2(t+\tau) \rangle}{\langle I_1(t) \rangle \langle I_2(t) \rangle} \qquad [4.1]$$

where I(t) is the fluorescence intensity on one of the two detectors at time t. The autocorrelation asks the question: on which time scales does the emission remain constant and which does it fluctuate? The fluctuations can arise from diffusion as molecules move in and out of the focal volume, or from internal dynamics of the emitter arising from triplet states, other dark states, or even the excited state lifetime. This equation assumes that the emission is split between two detectors using a 50/50 beamsplitter as shown in Figure 4-5 to allow correlation information to be extracted at short times below the dead time of the APD detectors[18, 19].

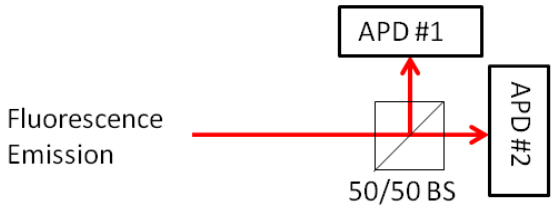

Figure 4-5: In order to measure autocorrelations at short time scales, the fluorescence emission is split onto two detectors using a cube 50/50 beam splitter.

Figure 4-6 plots the measured FCS curve for a 10pM concentration of ICG in ethanol (blue) and for a 10pM concentration of IR800cw in ethanol (red) both in the absence of bowtie nanoantennas. The autocorrelation function in each case was computed from the photon arrival times using a commercial package (Symphotime, Picoquant). These curves have been normalized to the value of G(100 ns). They can be fit with the following standard equation, which includes contributions from diffusion through the focal volume as well as a short-lived dark state and are plotted as black dashed lines in Figure 4-6[20]:

$$G(\tau) = \frac{1}{N}\frac{1}{\left(1+\frac{\tau}{\tau_D}\right)\left(1+\frac{\tau}{\kappa^2\tau_D}\right)}\left[1 - D + De^{\tau/\tau_{dark}}\right] \qquad [4.2]$$

where N relates to the average number of molecules in the focal volume, τ_D is the diffusion time, κ is a shape factor that describes the asymmetry of the ellipsoidal Gaussian focus, D is the amplitude of the dark state contribution, and τ_{dark} is the dark state lifetime. For ICG, τ_D is 608 μs, which corresponds to the amount of time the molecule tends to spend in a diffraction-limited volume of water and τ_{dark} is 4 μs. For IR800cw, τ_D is 274 μs and τ_{dark} is 1 μs.

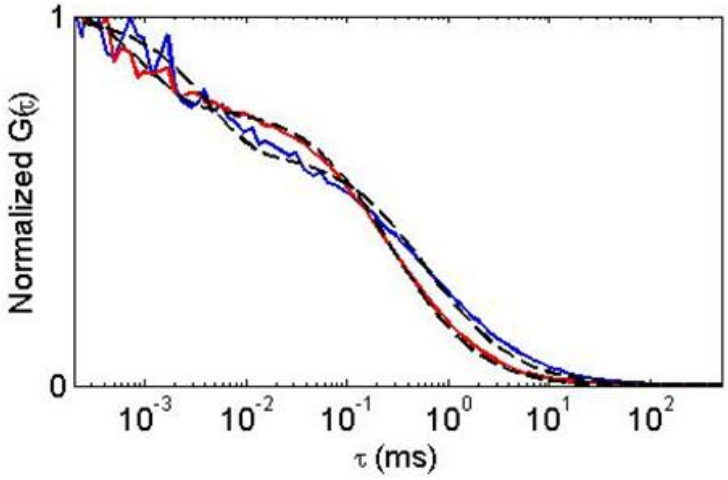

Figure 4-6 FCS of 10pM ICG in water (blue) and 10pM IR800cw in ethanol (red) without bowtie nanoantenna. Fits to Eqn. 4-2 are shown as dashed lines.

4.6 Bowtie-Enhanced FCS

Time traces of the fluorescence emission intensity for single bowties immersed in a 1 μM solution of IR800cw in ethanol and ICG in water are shown in Figure 4-7. In both cases, flashes of fluorescence can be seen whenever a molecule enters the enhanced field region of the bowtie nanoantenna and until the molecule eventually photobleaches. No single-molecule fluorescence flashing events are measured in the absence of the bowtie nanoantennas at 1μM concentrations of either dye, as is expected since with large N the bursts cannot be observed (and the contrast in the autocorrelation disappears, see below). Notice that the contrast between single enhanced molecules and background is much higher for ICG than for IR800cw. This difference supports the conclusion that ICG is a better molecule for bowtie FCS than IR800cw since it has a lower intrinsic QE and hence a higher bowtie-induced fluorescence enhancement.

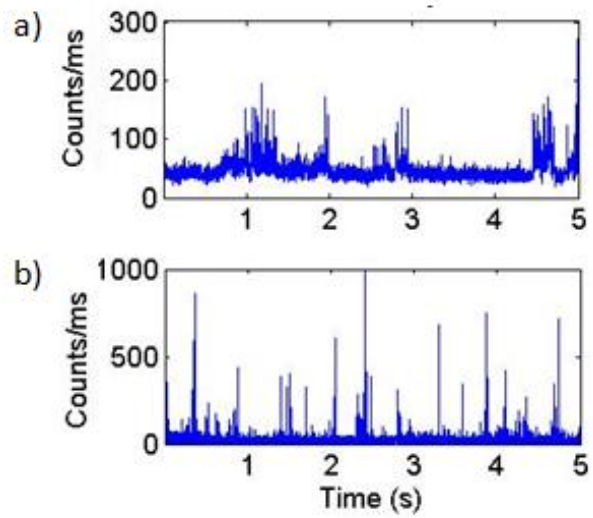

Figure 4-7: a) Fluorescence time trace binned to 1ms for a bowtie immersed in 1μM IR800cw in ethanol using 430W/cm^2 laser intensity. b) Fluorescence time trace binned to 1ms for a bowtie immersed in 1μM ICG in water using 144kW/cm^2 laser intensity. Notice that ICG in water has higher contrast between enhanced molecules compared to background than IR800cw in ethanol.

Figure 4-8b plots the normalized FCS curves collected on a single bowtie immersed in 1 μM ICG in water. All FCS curves were taken from 5 minutes of time-tagged fluorescence data. Notice that at lower excitation intensities, the timescale for the bowtie FCS curve decay is much longer than the FCS curve in the absence of the bowtie nanoantenna (black solid curve). This difference in time scale is consistent with the picture that molecules transiently stick to the surface near the bowtie nanoantenna and then photobleach. The simplest model for photobleaching is that a molecule has a fixed probability of photobleaching during any excitation cycle and this does not change with excitation power. This means that a molecule has a total number of photons that it tends to emit before photobleaching that remains constant for different excitation powers. Therefore, as the excitation intensity is increased, the molecule will emit the same number of photons but in progressively shorter periods of

time, causing the photobleaching time, τ_{photo}, to shorten. This behavior is seen in the bowtie FCS curves in Figure 4-8b. Therefore, the long-time decay in the bowtie FCS curves is not due to diffusion as in Fig. 4-6, but instead the long time decay reports on photobleaching times at different molecule positions and orientations on the surface.

Since an enhanced molecule can be in a number of different positions and orientations and still be measured, then a continuum of different photobleaching times underlies the FCS curve. Photobleaching is often a Poisson process with exponential waiting time, but here a distribution of characteristic times must be present. This type of multi-exponential behavior is commonly modeled with a stretched exponential[21, 22]. Therefore, the bowtie FCS curves were fit with the following equation:

$$G(\tau) = \frac{1}{N} e^{-(\tau / \tau_{photo})^{\beta}} \qquad [4.3]$$

where N relates to the concentration, τ_{photo} is the photobleaching time parameter, and β is the usual stretching parameter. As usual, when $\beta = 1$, the FCS curve is a single exponential, but as β approaches zero, the exponential is stretched and is representative of the sum of more and more exponentials. The fits agree well with the data and are plotted as dashed lines in Figure 4-8b. The extracted fit parameters are plotted in Figure 4-8c-e as a function of pumping intensity with 95% confidence interval bootstrapped errors. In particular, notice that in Figure 4-8d as the excitation power increases, the inverse of τ_{photo} increases, consistent with photobleaching behavior. For the bowtie FCS curves, β values between 0.15 to 0.32 are observed, indicating that the FCS curves are actually sums of a broad continuum of photobleaching times. Further, it is interesting to note that as the excitation intensity

increases, β decreases, which means that at higher excitation intensities there are more underlying exponentials than at lower excitation intensities, a reasonable observation given the fact that more and more non-optimally oriented and located molecules can contribute under these conditions.

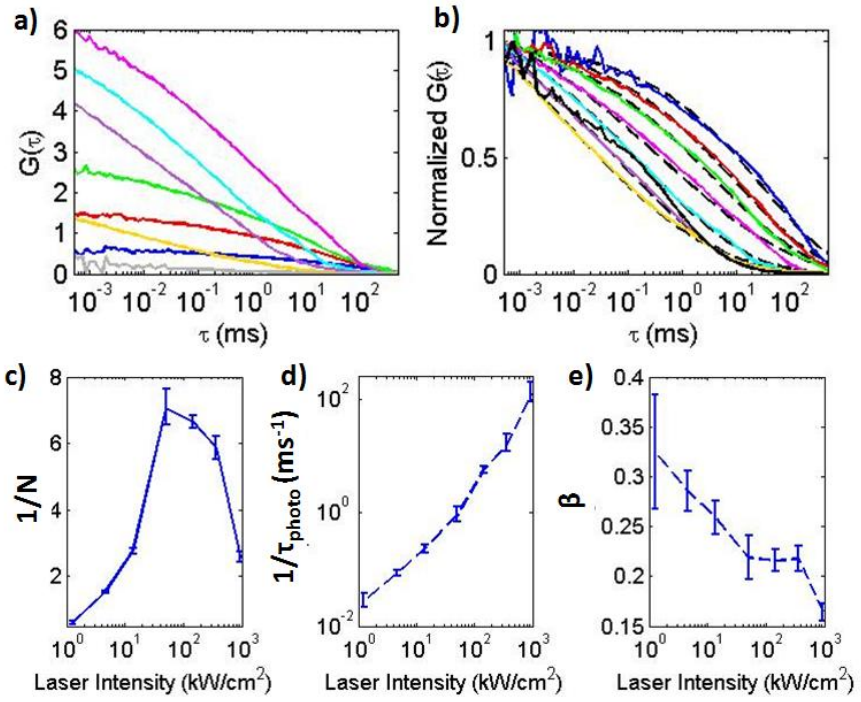

Figure 4-8: a) FCS curves for a bowtie immersed with 1μM ICG in water when illuminated with pump intensity 1.3 kW/cm^2 (blue), 4.6 kW/cm^2 (red), 14kW/cm^2 (green), 50kW/cm^2 (pink), 144kW/cm^2 (cyan), 362kW/cm^2 (purple), and 940kW/cm^2 (yellow). The grey curve indicates the FCS curve for the same 1μM ICG in water solution but without a bowtie nanoantenna at 110kW/cm^2 laser intensity. b) FCS curves from (a) are normalized to their value at τ = 100ns and clearly show that the photobleaching time, $\boldsymbol{\tau_{photo}}$, decreases as the laser intensity increases. Fits to each curve using equation 4.3 are plotted with dashed black lines. The FCS curve for a 10pM solution of ICG in the absence of a bowtie nanoantenna with 2.9MW/cm^2 laser intensity is plotted in solid black. c-e) Fit parameters used for fit curves shown in (b) using equation 4.3.

Turning now to the other fluorophore, IR800cw, even though this molecule is not optimal for bowtie FCS, the FCS curves can still be recorded at low powers as shown in Figure 4-9a,b. The lower S/B ratio makes the FCS curves have lower contrast and thus more challenging to measure. Notice that the absolute G(100ns) for these curves in Figure 4-9a for IR800cw is much lower than in Figure 4-9a for ICG, a consequence of a lower S/B ratio for IR800cw. As was measured for ICG bowtie FCS, the photobleaching time for IR800cw bowtie FCS is found to decrease as the excitation intensity increases.

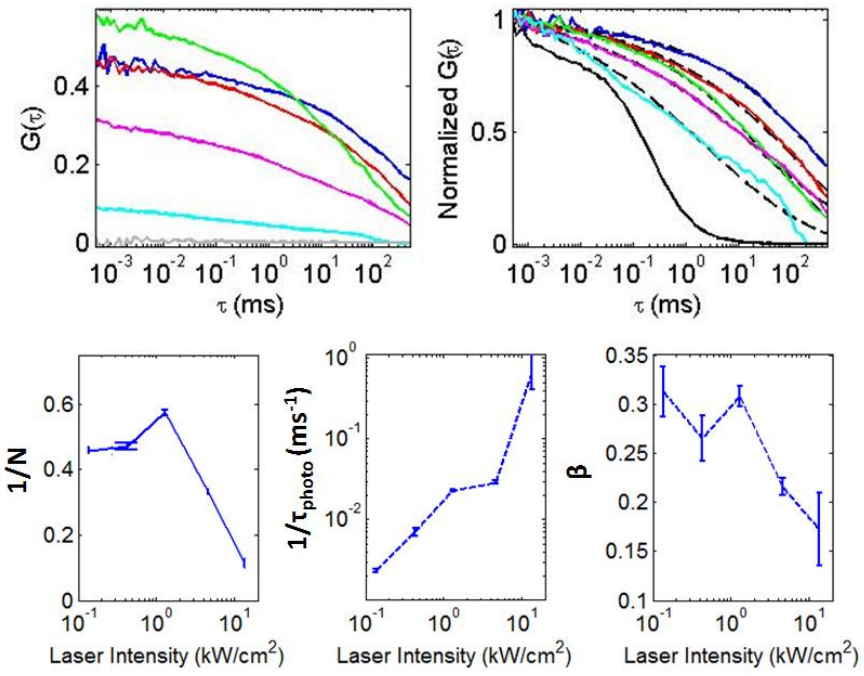

Figure 4-9 a) FCS curves for a bowtie immersed in 100nM IR800cw in ethanol when illuminated with 0.14 kW/cm^2 (blue), 0.47 kW/cm^2 (red), 1.3 kW/cm^2 (green), 4.6 kW/cm^2 (pink), and 13.8 kW/cm^2 (cyan). The grey curve indicates the FCS curve for the same 100nM IR800 in ethanol solution but without a bowtie nanoantenna at 1.3 kW/cm^2 laser intensity. b) FCS curves from (a) are normalized to their value at τ = 100 ns and clearly show that the photobleaching time decreases as the laser intensity increases. Fits to each curve using equation 4.1 are plotted with dashed black lines. The FCS curve for

a 10pM solution of IR800cw in the absence of a bowtie nanoantenna with 1.9MW/cm^2 laser intensity is plotted in solid black. c-e) Fit parameters used for fit curves shown in (b) using equation 4.1.

4.7 Conclusions

Bowtie FCS has been shown as a viable alternative to zero-mode waveguides when studying molecules immobilized on the surface of a substrate at high (μM) concentrations. As a proof-of-principle, bowtie FCS successfully measured the photobleaching (turn-off) times of high (1μM) concentration of ICG in water as a function of laser intensity. While this method is currently limited to molecules that linger in the enhanced region, many experiments of this type are possible. For instance, an enzyme could be attached to the surface near the bowtie and whenever it acts on a fluorescently labeled substrate molecule at μM concentrations, then the molecule will be held near the bowtie for an extended period of time, allowing for easy measurement. In a similar fashion, a biomolecule with a ligand binding site can be attached to the surface, and then fluorescently labeled ligands which bind to the biomolecule can be easily detected, and the unbinding times directly measured.

Acknowledgements: I would like to thank Dr. Zongfu Yu for his help in analyzing the acquired data.

References

1. Kinkhabwala, A. *et al*. Large Single-Molecule Fluorescence Enhancements Produced by a Gold Bowtie Nanoantenna. *Nat. Photonics* **3**, 654 (2009).

2. Eid, J. & et. al. Real-Time DNA Sequencing from Single Polymerase Molecules. *Science* **323**, 133-138 (2009).

3. Levene, M. J. *et al*. Zero-Mode Waveguides for Single-Molecule Analysis at High Concentrations. *Science* **299**, 682-686 (2003).

4. Uemura, S. *et al*. Real-time tRNA Transit on Single Translating Ribosomes at Codon Resolution. *Nature* **464**, 1012-1017 (2010).

5. Fromm, D. P., Sundaramurthy, A., Schuck, P. J., Kino, G. S. & Moerner, W. E. Gap-dependent optical coupling of single "bowtie" nanoantennas resonant in the visible. *Nano Lett.* **4**, 957-961 (2004).

6. Fromm, D. P. *et al*. Exploring the chemical enhancement for surface-enhanced Raman scattering with Au bowtie nanoantennas. *J. Chem. Phys.* **124**, 061101 (2006).

7. Fromm, D. Improving the Size Mismatch Between Light and Single Molecules using Metallic Nanostructures. *Stanford Ph. D. Thesis* (2005).

8. Tam, F., Goodrich, G. P., Johnson, B. R. & Halas, N. J. Plasmonic enhancement of molecular fluorescence. *Nano Lett.* **7**, 496-501 (2007).

9. Bakker, R. M. *et al*. Enhanced localized fluorescence in plasmonic nanoantennae. *Appl. Phys. Lett.* **92**, 043101 (2008).

10. Ringler, M. *et al*. Shaping emission spectra of fluorescent molecules with single plasmonic nanoresonators. *Phys. Rev. Lett.* **100**, 203002 (2008).

11. Biteen, J. S., Lewis, N. S., Atwater, H. A., Mertens, H. & Polman, A. Spectral tuning of plasmon-enhanced silicon quantum dot luminescence. *Appl. Phys. Lett.* **88**, 131109 (2006).

12. Chen, Y., Munechika, K. & Ginger, D. Dependence of Fluorescence Intensity on the Spectral Overlap between Fluorophores and Plasmon Resonant Single Silver Nanoparticles. *Nanolett* **7**, 690-696 (2007).

13. Gerard, D. *et al*. Nanoaperture-enhanced fluorescence: Towards higher detection rates with plasmonic metals. *Phys. Rev. B* **77**, 045413 (2008).

14. Magde, D., Elson, E. & Webb, W. W. Thermodynamic Flucutations in a Reacting System - Measurement by Fluorescence Correlation Spectroscopy. *Phys. Rev. Lett.* **28**, 705 (1972).

15. Eigen, M. & Rigler, R. Sorting Single Molecules: Application to Diagnostics and Evolutionary Biotechnology. *Proc. Natl. Acad. Sci. U. S. A.* **91**, 5740-5747 (1994).

16. Rigler, R. Fluorescence correlations, single-molecule detection, and large number screening: applications in biotechnology. *J. Biotechnol.* **41**, 177-186 (1995).

17. Rigler, R., Elson, E. & Elson, E. in *Springer Series in Chemical Physics Vol. 65; Fluorescence Correlation Spectroscopy; Springer Series Chem. Phys* (eds Schaefer, F. P., Toennies, J. P. & Zinth, W.) (SpringerRigler, R, Berlin, 2001).

18. Widengren, J., Mets, U. & Rigler, R. Fluorescence correlation spectroscopy of triplet states in solution: a theoretical and experimental study. *J. Phys. Chem.* **99**, 13368-13379 (1995).

19. Hess, S. T., Huang, S., Heikal, A. A. & Webb, W. W. Biological and chemical applications of fluorescence correlation spectroscopy: a review. *Biochemistry* **41**, 697-705 (2002).

20. Dittrich, P. & Schwille, P. Photobleaching and stabilization of fluorophores used for single-molecule analysis with one- and two-photon excitation. *App Phys B* **73**, 829 (2001).

21. Burland, D. M., Miller, R. D. & Walsh, C. M. Second-order nonlinearity of poled-polymer systems. *Chem. Rev.* **94**, 31-75 (1994).

22. Edman, L., Mets, U. & Riger, R. Conformational transitions monitored for single molecules in solution. *Proc. Natl. Acad. Sci. U. S. A.* **93**, 6710-6715 (1996).

Chapter 5 - Toward Bowtie Nanoantennas as Apertureless Scanning Near-field Probes

5.1 Introduction

Gold bowtie nanoantennas have been shown to greatly enhance the fluorescence from low QE molecules (Chapter 3), but so far only bowtie nanoantennas fabricated onto glass coverslips have been discussed. These structures could be very useful if instead fabricated onto a scanning tip and used for ANSOM (Chapter 2), forming a bowtie on a tip ("BOAT"). Then, the bowtie could be positioned directly above a molecule using standard AFM technology, instead of relying on randomly distributing molecules around the bowtie. Other scanning plasmonic tips exist – such as metal-coated fibers with sub-diffraction limited apertures[1-3] (NSOM), sharpened metal AFM tips[4-10] (ANSOM), and other novel ANSOM probes such as aluminum bowtie nanoantennas[11, 12]. Our goal was to fabricate the gold bowtie nanoantenna onto AFM tips, since they have proven useful in fluorescence enhancement.

Two approaches to fabricating gold bowtie nanoantennas onto AFM tips in the Stanford Nanofabrication Facility (SNF) and in the Raith facility in Dortmund, Germany will be discussed. In both approaches, the AFM tip is first flattened in order to provide a flat surface for the bowtie nanoantenna to be fabricated. In the first

approach, developed by Arvind Sundaramurthy, E-beam lithography is used to define the bowtie shape, which requires float-coating of an E-beam resist, in addition to the normal E-beam processing steps for a non-conductive substrate. In the second approach, a gold metal film is deposited on an AFM tip and FIB (Focused Ion Beam) milling is used sculpt a bowtie nanoantenna out of the gold. The E-beam approach was found to be too technically challenging, while the FIB approach proved to be relatively simple in fabrication but yielded bowties that did not enhance molecular fluorescence. While a scanning bowtie would be very useful in ANSOM, it has proven difficult to fabricate a highly resonant structure onto an AFM tip.

5.2 Initial Preparation of AFM Tip

The fabrication for both the E-beam and FIB approach begins the same way. In both cases, a Si_3N_4 AFM tip (Veeco) is flattened using a FIB, in order to have a flat area upon which to fabricate the bowtie nanoantenna. Si_3N_4 contact mode AFM tips were chosen because Si_3N_4 is transparent to optical wavelengths and should not interfere with the bowtie's plasmon resonance, unlike the more common Si AFM tips. The AFM tip is coated with a 4nm thick layer of chrome by Tom Carver in the Ginzton cleanroom (Figure 5-1a,c). This layer is necessary because the tip is insulating and cannot be imaged by an electron beam or milled by an ion beam without it. The tip is then loaded into a FEI Strata 235DB dual beam FIB/SEM, in order to flatten it (Figure 5-1b,d). The tip is sculpted to have a 500 nm x 500 nm flat area for lithography, as well as a post (bar) of ~30nm height. This post is useful because ANSOM experiments typically require the AFM tip be brought into contact

with the surface, a process that might damage the delicate bowtie nanoantenna. Since the post is the tallest object on the tip, it will be the first part to come into contact with the sample allowing the bowtie to be close to the sample and yet remain undamaged. From here, the E-beam and FIB fabrication processes diverge.

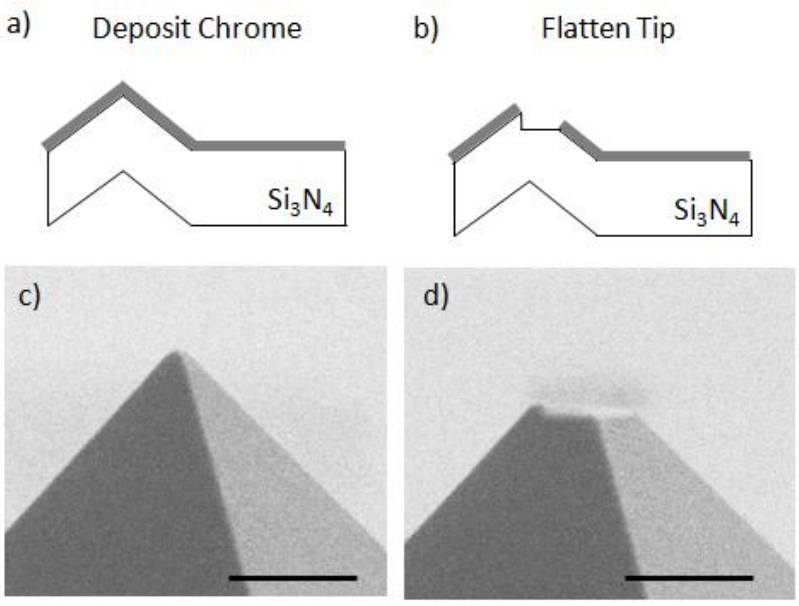

Figure 5-1: Initial flattening of an AFM tip using FIB. a) Schematic of AFM tip before FIB processing. A thin (4 nm) layer of chrome is deposited uniformly on the tip to prevent charging during FIB milling and SEM imaging. b) After FIB milling, the tip is flattened, except for a short (~30 nm) post, which will be used to protect the eventually fabricated bowtie nanoantenna during AFM imaging. c) SEM of Si_3N_4 AFM tip before FIB milling. Scale bar = 1 μm. d) SEM of same Si_3N_4 AFM tip after FIB milling. Scale bar = 1 μm.

5.3 E-beam Lithography Approach

5.3.1 FIB-milled Alignment Marks

In order to use E-beam lithography, alignment marks on the cantilever near the tip are necessary. When performing E-beam lithography, it is important to avoid

directly SEMing the intended write region when it coated in resist, as SEMing develops the resist. SEMing is, however, the only way to orient the sample, so remote alignment marks are used to setup a local coordinate system in order to avoid direct exposure of the tip to the electron beam once it has been coated in resist.

Figure 5-2 is an SEM of the typical alignment crosses milled using a FIB, where the actual tip is just visible at the top of the image. Each line of the cross is 5 μm long and <100 nm wide. When making alignment marks, the goal is to fabricate marks that are easy to locate (hence the 5μm length of the lines) as well as highly precise in their center position (<100nm widths of the lines).

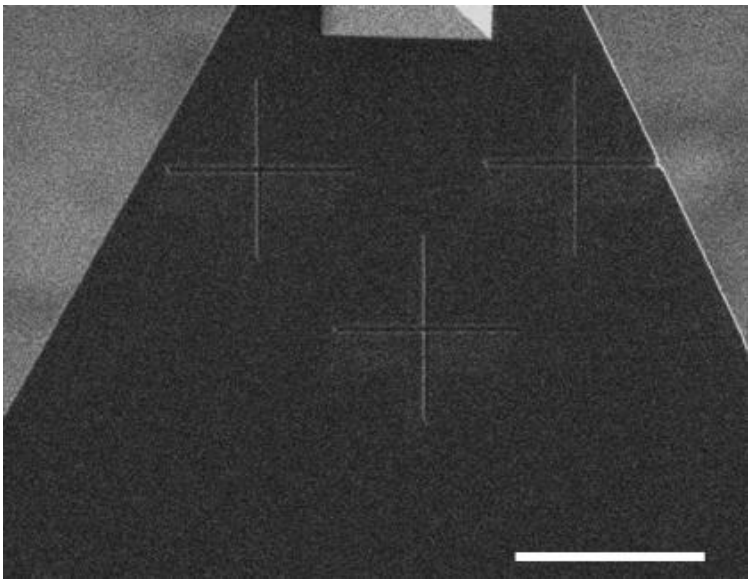

Figure 5-2: SEM of calibration marks milled into an AFM cantilever. Scale bar = 5 μm.

5.3.2 Locating Alignment Marks

Once the tip is flattened and has alignment marks, the FIB is no longer needed. The sample is loaded into the E-beam (without resist and with the chrome layer) in order to measure the distance from the alignment marks to the flattened tip apex. At

this point, taking a quick SEM of the tip apex is necessary and should not harm the sample since there is no resist on the sample to expose. This brief SEMing will deposit a small amount of carbon onto the sample, but not enough to harm the bowtie that will be fabricated there. Once the sample is loaded, each of the alignment marks and AFM tip apex are found by moving the feature into the middle of the image and recording the stage coordinates. This step can be done in local coordinates by setting the tip's flattened apex or one of the alignment marks to be located at (0,0). This measurement step should be done with the Raith150 E-beam and not the FEI FIB, because the FEI FIB is not as accurate for absolute stage measurements. In addition to measuring the x and y coordinates, the Z focus change between the cantilever base and tip apex is measured. The Z focus change is important to measure accurately because the E-beam is sensitive to ~1 μm changes in focus and the distance between the cantilever base and apex is ~3 μm. It is important to be able to precisely focus the beam in order to write bowtie nanoantennas with sharp features and small gaps.

5.3.3 Chrome Etch

Now, the 4nm thick layer of chrome is etched by soaking in CR-14 chrome etchant for ~5 seconds. CR-14 is fairly specific to chrome and will not etch the Si_3N_4 in this short period of time

5.3.4 Float Coating of E-beam Resist

The next step in the E-beam lithography process is to coat the tip in resist (PMMA). Unfortunately, spin coating is not an option because it leaves an uneven layer of resist on an AFM tip (see Chapter 2 for details), so another method must be

used, namely float-coating[13]. Briefly, this procedure (outlined in Figure 5-3) consists of placing the AFM tip into a water bath and then putting one drop of 1% PMMA in toluene onto the surface of the water. The toluene evaporates, leaving behind a smooth layer of PMMA behind on the water surface, since PMMA does not dissolve in water. When the water is pipetted out, the PMMA layer evenly coats the tip and is then baked at 90ºC for 30 minutes to ensure all the water has been baked out.

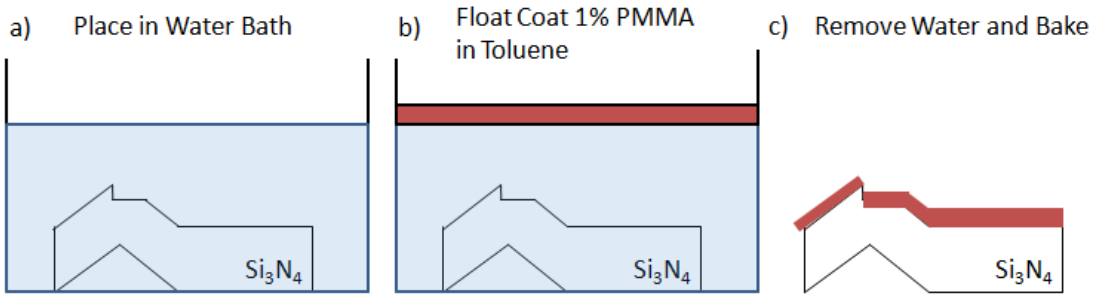

Figure 5-3: Float-coating of resist onto an AFM tip. a) Tip is placed in a water bath. b) 1 drop of a 1% PMMA in toluene solution is dropped onto the water's surface. A thin layer of PMMA forms as the toluene evaporates. c) Water is pipetted out, letting the resist gently rest upon the AFM tip. The tip is baked at 90ºC for 30 minutes to remove any remaining water.

There are two major problems with float-coating, the first of which is demonstrated in Figure 5-4; most of the time, the AFM tip bends during float-coating. The bending can be as extreme as depicted in Figure 5-4, where the tip is no longer even pointing vertically, just slightly bent or, occasionally, not bent at all. The bending is not due to the weight of the resist, but rather due to the tension of the PMMA film. This means that sometimes, with great care and luck, the tip can be gently tapped with tweezers from underneath to break the film and relieve the tension within the PMMA film. While this is a problem, with enough persistence some tips

will survive this step with minimal to no bending. Note that bending alters the change in the focal distance, as well as the change in lateral distance, between the alignment marks and apex tip, so these measurements will be incorrect if significant bending has occurred.

The second problem with float-coating is the irreproducibility in the thickness of the resist. While float-coating forms locally uniform resist films, the thickness over the entire film can change from ~20-200 nm. The dose used in exposing resist is critically dependent upon the thickness, so it is difficult to correctly expose a resist film with unknown thickness. A moderately high line dose, ~360pA/s, is used so that the resist will likely be fully exposed.

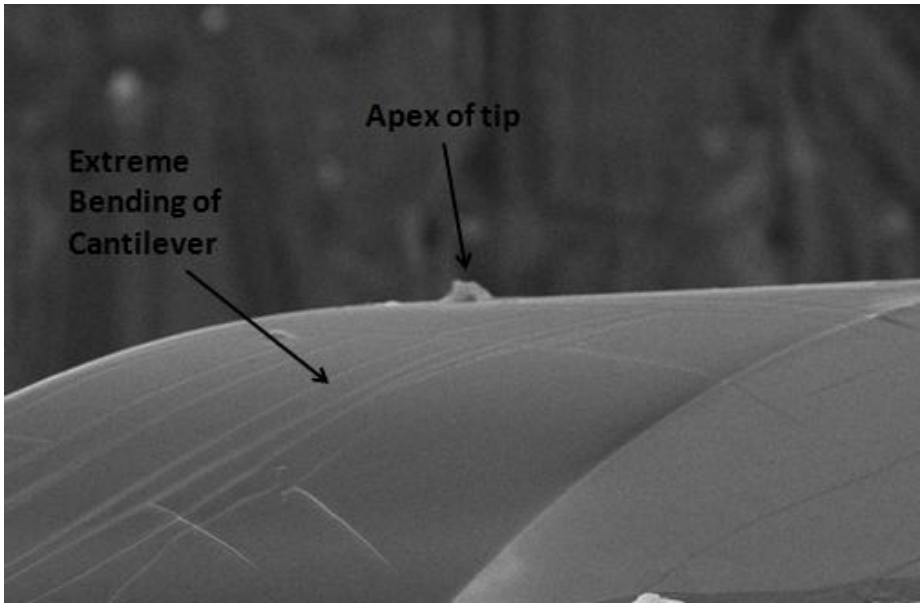

Figure 5-4: SEM showing cantilever bending after float-coating of E-beam resist.

5.3.5 Chrome Deposition

Since the AFM tip is non-conductive, a 4nm thick layer of chrome must once again be deposited onto the AFM tip (Figure 5-5a). Note that this is the second chrome deposition required and that the two chrome depositions cannot be combined, since the bowtie should not be fabricated on top of a chrome layer. This means that the first chrome layer must be etched off, then resist float-coated, and finally a new chrome layer deposited for E-beam exposure.

5.3.6 Standard E-beam Lithography Steps

The tip is now loaded into Raith150 for exposure of bowtie shaped features into the resist (Figure 5-5b). The alignment marks are located to setup a local coordinate system and then the bowtie shape is exposed on the apex of the tip. Directions for using the Raith150 for a bowtie exposure can be found in Appendix A. After the resist has been exposed, the chrome must once again be etched off (Figure 5-5c) in Cr-14 chrome etchant for ~5 seconds. The exposed resist on the tip is then removed by development in 1:4 Methyl Isobutyl Ketone (MIBK):Isopropanol for 35 s followed by soaking for 40 s in pure Isopropanol (Figure 5-5d). Finally the tip is given to Tom Carver for 4 nm titanium sticking layer and 20 nm gold deposition (Figure 5-5e).

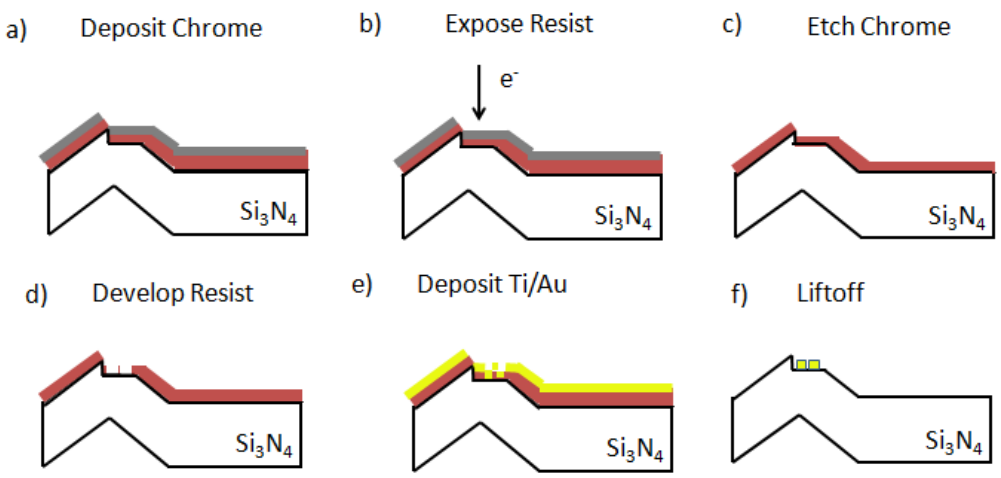

Figure 5-5: E-beam lithography process flow for nonconductive substrate. a) Deposit chrome onto float-coated resist layer. b) Expose resist using Raith 150 E-beam Lithography Tool. c) Etch chrome layer in CR14 chrome etchant to expose resist layer. d) Develop resist in 1:4 Methyl Isobutyl Ketone: Isopropanol for 35 s and Isopropanol for 40 s. e) Deposit 4 nm titanium and 20 nm gold. f) Liftoff resist by various methods described below.

5.3.7 Liftoff

The final step in this process is liftoff (Figure 5-5f), which never fully worked satisfactorily. Normally, liftoff is performed by placing the substrate in acetone and sonicating briefly, but sonication cannot be performed on AFM tips since the cantilevers break. Sometimes, liftoff can be performed by simply soaking the substrate in acetone, but this never worked on the AFM tips. I also tried soaking in heated acetone, heated PG remover, as well as oxygen plasma etching, but was never able to completely remove the non-bowtie shaped metal. Figure 5-6a shows one tip after development and metal deposition, but before lift-off. For this tip, I wrote an array of bowties, with one targeted to the apex of the tip (red lines show this targeting was successful). Figure 5-6b shows this tip after liftoff by soaking in acetone. Most

of the resist is removed, except for the resist near the tip itself – the most important area. A bowtie that was written at the base of the tip is shown in Figure 5-6c. This SEM shows that the array of bowties in the lifted-off region were written and developed successfully. This particular bowtie looks jagged and uneven because when writing the bowtie, the focus was set for the apex of the tip, so this bowtie was written ~3 µm out of focus. Since this bowtie was written out of focus and yet lifted off correctly, the overall dose was chosen to be high enough. It is still unknown why liftoff works well on flat areas when using float-coated resist, but the resist on the tip cannot be lifted off.

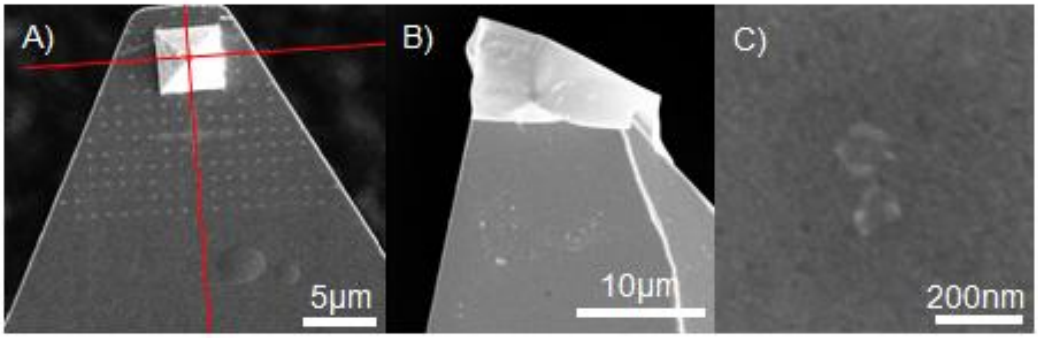

Figure 5-6: SEM's of best attempt at E-beam bowtie fabrication on an AFM tip. a) SEM of an AFM tip after development and metal deposition. An entire array of bowties were written on the cantilever, not just on the tip apex, so the white spots are bowtie-shaped holes in the resist. The red lines indicate the position of the bowtie that was targeted for the tip. b) SEM of the same tip after titanium/gold deposition and liftoff. The gold has peeled off of most of the cantilever and is now draped on top of the tip itself. c) SEM of one of the bowties written on the flat part of the cantilever, next to the tip. This bowtie is misshapen due to writing approximately 3 µm out of focus.

5.3.8 E-beam Fabrication Conclusions

The two main problems in the E-beam process are the bending of the cantilever during float-coating and incomplete liftoff. While the bending problem just makes the

eventual yield of bowtie AFM tips smaller, the liftoff problem was never solved and thus no E-beam bowtie AFM tips were fabricated. A previous graduate student, Arvind Sundaramurthy, did successfully fabricate a few E-beam bowtie AFM tips using this method (Figure 5-7), so this fabrication is possible, but very difficult to reproduce.

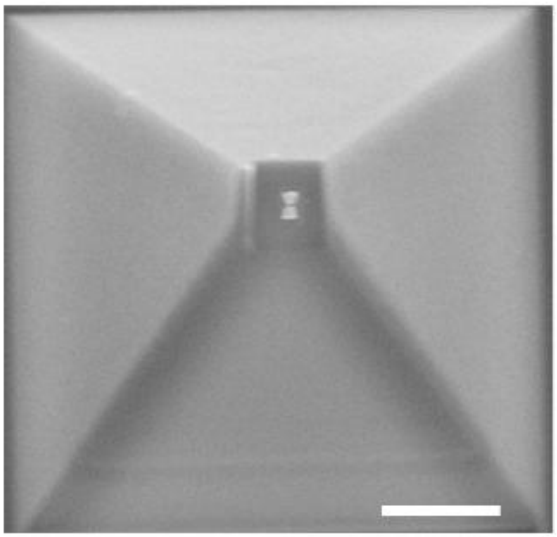

Figure 5-7: SEM of a bowtie on an AFM tip fabricated by Arvind Sundaramurthy using E-beam lithography. Scale bar = 1 μm.

5.4 Focused Ion Beam Process Flow

5.4.1 Introduction

An alternative to using E-beam lithography to fabricate the bowtie nanoantenna, is to instead use the FIB. In this scheme, the entire tip is covered in gold and the FIB removes all the gold in a ~4μm^2 area except for a bowtie-shaped region. This fabrication is much easier, but there is one severe drawback. When the FIB mills, it deposits Ga^{++} ions into the substrate, which alters the optical properties of the bowtie and renders the tips essentially unusable for fluorescence enhancement

experiments. This section will detail the fabrication involved, as well as optical experiments showing the lack of fluorescence enhancement when using FIB bowtie nanoantennas on AFM tips.

5.4.2 Chrome Etch and Gold Deposition

The first step in this process is to etch the conductive chrome layer off of the tip in CR-14 chrome etchant. Calibration marks will not be used, so the chrome is no longer necessary. Next, a uniform layer of 4 nm titanium and 20 nm gold is deposited onto the AFM cantilever (Figure 5-8a). Note that this gold layer serves to make the sample conductive for the FIB milling steps ahead.

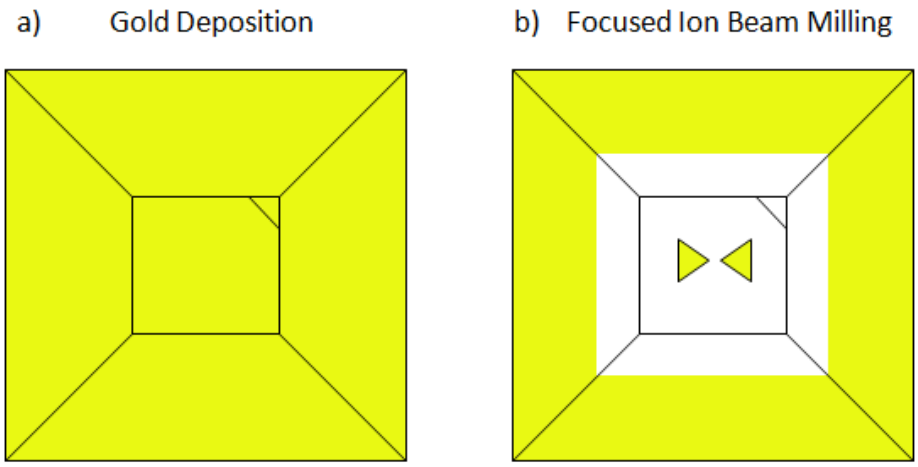

Figure 5-8: Schematic of FIB Process Flow. a) A 4 nm titanium sticking layer followed by a 20 nm gold layer are deposited by Tom Carver in the Ginzton cleanroom. b) The FIB is used to mill away gold in the pattern of a bowtie nanoantenna

5.4.3 Focused Ion Beam Milling

Finally, the tip is loaded into the FIB in order to mill the bowtie shape into tip (Figure 5-8b and Figure 5-9). Appendix B has detailed instructions for using the FIB,

with particular information for writing patterns with small feature sizes, such as the bowtie nanoantenna. The key points to remember are to use a small beam aperture (1 pA current) and to focus and stigmate the beam as well as possible. At Stanford, the FEI Strata 235DB tool is capable of making 30 nm feature sizes, too large for the small gap bowties needed, so the Raith ionLiNE (capable of <10nm features) was used instead in Dortmund, Germany, in collaboration with Dr. Sven Bauerdick and Dr. Jason Sanabia, to mill the small gap bowtie in Figure 5-9. The vertical lines in Figure 5-9 are due to the beam pattern used in the pattern to mill the bowtie nanoantenna and do not correspond to gold metal remaining on the tip.

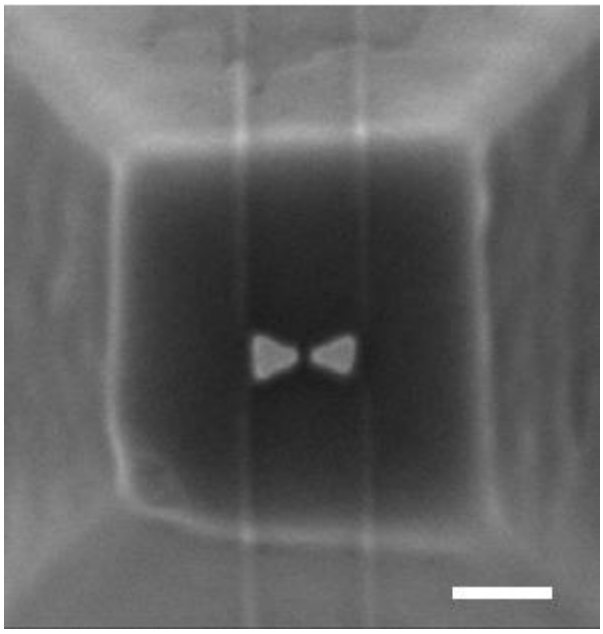

Figure 5-9: SEM of a FIB BOAT fabricated on Raith's ionLiNE FIB tool. Scale bar is 200 nm.

5.4.4 Scattering measurements on flat substrate FIB bowties

Thus far in this thesis, only E-beam bowties have been characterized and shown to be useful for enhancing single-molecule fluorescence. For FIB fabricated bowties, the effects of the ion beam, particularly gallium implantation into the

substrate, on the plasmon resonance and electric field enhancement were unknown. Therefore, in addition to the BOAT fabrication, bowtie nanoantennas were FIB milled on flat quartz substrates (Figure **5-10**a) for scattering studies. Due to the optics used for scattering studies in this thesis (see Chapter 2 for optical setup), it is only possible to measure the resonance for bowties on flat substrates.

The scattering spectra for two bowties with ~25nm gap sizes fabricated with E-beam lithography or FIB milling, are compared in Figure 5-10b. Notice that the peak of the resonance is approximately the same in both cases, but the width of the resonance is much broader for the FIB bowties. This broadening may indicate that while the resonance is located in the same position, the enhanced fields are lower for the FIB fabricated bowtie.

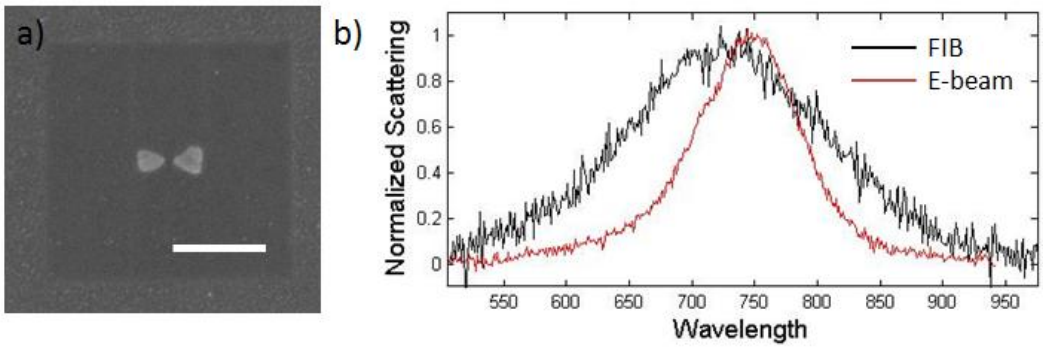

Figure 5-10: Scattering study of FIB-milled bowties. a) SEM of FIB bowtie nanoantenna on a flat quartz substrate with 20nm gap. b) Comparison between scattering spectra for E-beam and FIB fabricated bowties on quartz substrates with similar gap sizes.

5.4.5 Optical Results from FIB Bowties on AFM tips

Ultimately, the best test for whether the FIB bowtie nanoantenna is useful is to see if it enhances the fluorescence of the fluorophore TPQDI, since the application for these tips is apertureless near-field imaging of Raman-active or fluorescent molecules.

In this section, measurements of the enhancement (or quenching) of fluorescence by a FIB bowtie on an AFM tip will be shown.

In order to test for fluorescence enhancement using a FIB bowtie on an AFM tip, a thin film (~30 nm) of TPQDI-doped PMMA was spun onto a clean coverslip and loaded into a confocal microscope. The FIB bowtie AFM tip was then raster scanned above the sample and fluorescence was recorded as a function of bowtie position (Figure 5-11). Since the sample remains fixed, the recorded fluorescence image is the fluorescence as a function of AFM tip position, so if the bowtie is enhancing fluorescence, there will be more fluorescence photons detected when it is scanned through the focal volume of the objective. Since the sample is stationary, the same molecules are excited for the entire tip-scan, which means this experiment relies on the fact that a bulk sample of TPQDI excited with low power shows very little photobleaching over a 5 minute time scale.

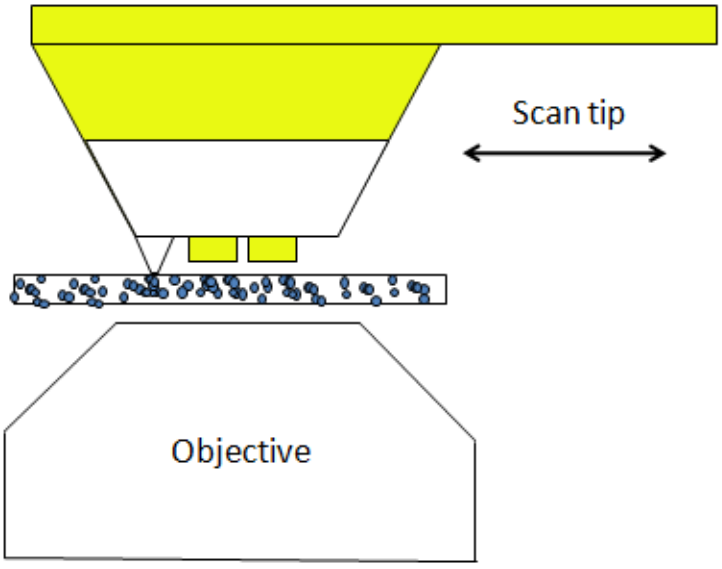

Figure 5-11: Schematic of setup used to test for enhancement of bulk TPQDI fluorescence using a FIB bowtie on an AFM tip. Blue circles are bulk (high concentration) TPQDI molecules.

The above experiment was performed for both a FIB bowtie AFM tip and a sharpened gold coated AFM tip (Figure 5-12a,b). For the FIB bowtie AFM tip, there actually appears to be a slight quenching of fluorescence with the bowtie is scanned over the focus (Figure 5-12c), while there is a definite enhancement seen for the apex of a sharpened gold AFM tip (Figure 5-12d) as expected from similar experiments in the literature.

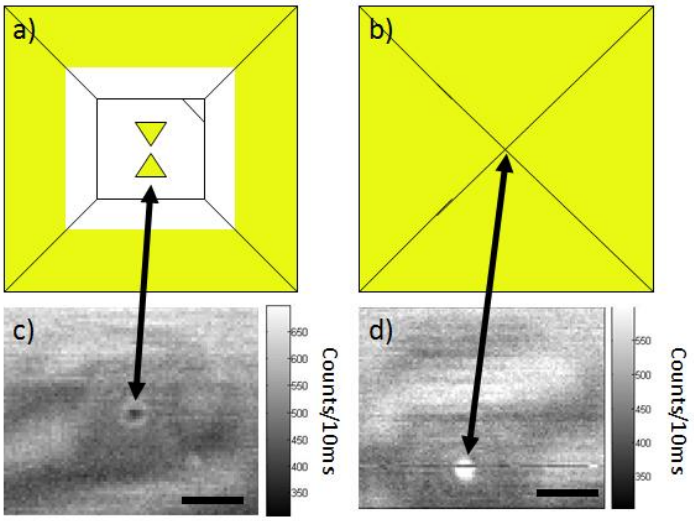

Figure 5-12: Fluorescence enhancement attempt with FIB bowtie on an AFM tip and sharpened gold AFM tip. a) schematic of the FIB bowtie AFM tip. b) Schematic of sharp gold-coated AFM tip. c) FIB bowtie AFM tip was scanned over a bulk TPQDI in PMMA sample. The sample remained fixed, while the tip was scanned, thus imaging the enhancement of fluorescence as a function of tip position. When the bowtie is positioned over the objective focus, the fluorescence is quenched. Scale bar = 1μm. d) When a sharpened gold coated AFM tip is scanned over the sample, an enhancement of fluorescence is measured. Scale bar = 1μm.

Since the FIB bowtie actually quenched instead of enhanced the fluorescence of TPQDI, this approach was abandoned. Aluminum FIB bowtie antennas have been shown to enhance the fluorescence from colloidal quantum dots by a factor of ~3[11, 12]. This enhancement is very low compared to the enhancements measured in this thesis for low quantum efficiency molecules coupled to E-beam fabricated bowties (~1300), and this difference is likely due to the gallium implantation into the substrate and metal that lowers the antenna efficiency in addition to the high QE of quantum dots. Overall, the gold FIB bowtie nanoantenna on an AFM tip does not appear to enhance fluorescence, so the FIB approach should be avoided.

5.5 Conclusions

In summary, two methods were developed to fabricate bowtie nanoantennas onto AFM tips. An E-beam lithography approach, developed by Arvind Sundaramurthy, was initially attempted because E-beam bowties have shown remarkable ability to enhance fluorescence of single molecules. Ultimately, this technique could not be reproduced and thus failed to produce any tips for testing. A simpler strategy involving FIB milling was then attempted and bowtie nanoantennas were successfully fabricated onto AFM tips. Unfortunately, these bowties did not enhance fluorescence of TPQDI, and so they were not usable as ANSOM tips. A highly resonant bowtie nanoantenna would still be very useful ANSOM tip, but as this chapter demonstrates, it is a difficult fabrication problem to solve.

References

1. Synge, E. H. A suggested method for extending the microscopic resolution into the ultramicroscopic range. *Philosopical Magazine* **6**, 356 (1928).

2. Pohl, D. W., Denk, W. & Lanz, M. Optical Stethoscopy: Image Recording with resolution Lambda/20. *App. Phys. Lett.* **44**, 651 (1984).

3. Lewis, A., Isaacson, M., Harootunian, A. & Muray, A. Development of a 500A Spatial Resolution Microscope: I. Light is Efficiently Transmitted Through Lambda/16 Diameter Apertures. *Ultramicroscopy* **13**, 227 (1983).

4. Zenhausern, F., Martin, Y. & Wickramasinghe, H. K. Scanning interferometric apertureless microscopy: optical imaging at 10 angstrom resolution. *Science* **269**, 1083-1085 (1995).

5. Hamann, H. F., Gallagher, A. & Nesbitt, D. J. Enhanced sensitivity in near-field scanning optical microscopy. *Appl. Phys. Lett.* **73**, 1469-1471 (1998).

6. Hillenbrand, R. & Keilmann, F. Material-specific mapping of metal/semiconductor/dielectric nanosystems at 10 nm resolution by backscattering near-field optical microscopy. *Appl. Phys. Lett.* **80**, 25-27 (2002).

7. Hartschuh, A., Sanchez, E. J., Xie, X. S. & Novotny, L. High-resolution near-field Raman microscopy of single-walled carbon nanotubes. *Phys. Rev. Lett.* **90**, 95503 (2003).

8. Bouhelier, A., Beversluis, M. R. & Novotny, L. Characterization of nanoplasmonic structures by locally excited photoluminescence. *Appl. Phys. Lett.* **83**, 5041-5043 (2003).

9. Hamann, H. F., Kuno, M., Gallagher, A. & Nesbitt, D. J. Molecular fluorescence in the vicinity of a near-field probe. *J. Chem. Phys.* **114**, 8596-8609 (2001).

10. Gerton, J. M., Wade, L. A., Lessard, G. A., Ma, Z. & Quake, S. R. Tip-Enhanced Fluorescence Microscopy at 10 Nanometer Resolution. *Phys Rev Lett* **93**, 180801-1 (2004).

11. Farahani, J. N. *et al*. Bow-tie optical antenna probes for single-emitter scanning near-field optical microscopy. *Nanotech* **18**, 125506-125510 (2007).

12. Farahani, J. N., Pohl, D. W., Eisler, H. -. & Hecht, B. Single Quantum Dot Coupled to a Scanning Optical Antenna: A Tunable Superemitter. *Phys Rev Lett* **95**, 017402-1-017402-4 (2005).

13. Zhou, H. *et al*. Lithographically Defined Nano and Micro Sensors using "Float Coating" of Resist and Electron Beam Lithography. *J. Vac. Sci. Technol. B* **18**, 3594 (2000).

Chapter 6 - Lithographic Positioning of Fluorescent Molecules on High-Q Photonic Crystal Cavities

The research reported in this chapter has been previously published in K. Rivoire, A. Kinkhabwala, F. Hatami, W. Ted Masselink, Y. Avlasevich, K, Müllen, W. E. Moerner, J. Vučković, "Lithographic Positioning of Fluorescent Molecules on High-Q Photonic Crystal Cavities" *Applied Physics Letters* **95,** 123113 (2009) (published online, September 23, 2009). Experimental results were measured jointly by K. Rivoire and A. Kinkhabwala from Prof. Vučković's and Prof. Moerner's lab's, respectively. Gallium Phosphide samples were grown by F. Hatami of Prof. W. Ted Masselink's group. The DNQDI molecule was synthesized by Y. Avlasevich of Prof. K. Müllen's group.

6.1 Introduction

Bowtie nanoantennas are not the only nanophotonic structures to alter fluorescence emission. Photonic crystal cavities also act to confine light, but they do so using total internal reflection and Bragg diffraction. In this way, photonic crystal nanocavities confine light into volumes smaller than a cubic optical wavelength with extremely high quality factor Q, producing a strong interaction between light and

emitters located in or near the cavity. These cavities have been used to demonstrate nanoscale on-chip devices and to probe fundamental quantum interactions between light and matter[1-4]. Experiments in this regime, however, are limited by the precision with which cavity and emitters can be spatially aligned and by the spectral range of the emitters that can be coupled to the narrow cavity resonance. Emitters are most often distributed randomly in the photonic crystal slab, and spatial alignment to the photonic crystal cavity occurs by chance. Recently, several techniques have been developed to position emitters with respect to cavities; these techniques rely primarily on either a mechanical transfer process to bring an emitter to the surface of the cavity[5, 6] or the fabrication of a cavity at the location of a previously detected emitter[7, 8]. Neither method is easily scalable to arrays of cavities and emitters, or achievable with conventional semiconductor fabrication processes. Here, we demonstrate coupling of near-IR fluorescent molecules to cavities with quality factors above 10,000 and show that we can selectively position these molecules on top of a nanocavity using conventional lithographic techniques.

6.2 Sample Fabrication and Preparation

Typically, photonic crystal cavity resonances are fabricated too far in the infrared to overlap with a fluorophore's absorption and emission spectra, but advances in the growth and lithography of gallium phosphide have allowed the fabrication of high quality (Q) factor photonic crystal cavities, up to 12,000, with resonances in the near-IR from 735 nm-860 nm[9]. For this experiment, a near-IR fluorescent molecule-doped polymer film is float-coated on top of high quality photonic crystal

nanocavities. A lithographic polymer (photoresist) is used, so that the molecules can be selectively positioned onto the location of the cavity by using a lithographic technique to remove unwanted molecules.

Coupled photonic crystal cavity-emitter systems studied so far are primarily based on gallium arsenide and silicon materials, which absorb strongly at wavelengths shorter than the electronic band gap of the material. This precludes the use of emitters such as organic molecules, which typically have resonances at visible and near-IR wavelengths. Research in photonic crystals operating at these shorter wavelengths has focused on materials such as GaN[10] and Si_3N_4 [11, 12]. These materials have a lower refractive index than GaAs or Si (n~2.4 for GaN and n~2.0 for Si_3N_4 compared to n~3.5 for GaAs and Si), which limits the size of photonic band gap and has generally led to low experimental quality factors of up to a few thousand, although designs with higher quality factors (Q up to 1 million) have been proposed[13]. It has previously been demonstrated[9] that photonic crystal cavities with quality factors up to 1,700, limited by fabrication inaccuracy, could be fabricated in gallium phosphide (GaP), a III-V semiconductor with n ~ 3.5 and indirect band gap at 550 nm. The high index of the material enables a large photonic band gap and cavities with high quality factor, while the large electronic band gap prevents absorption in the near-IR and part of the visible.

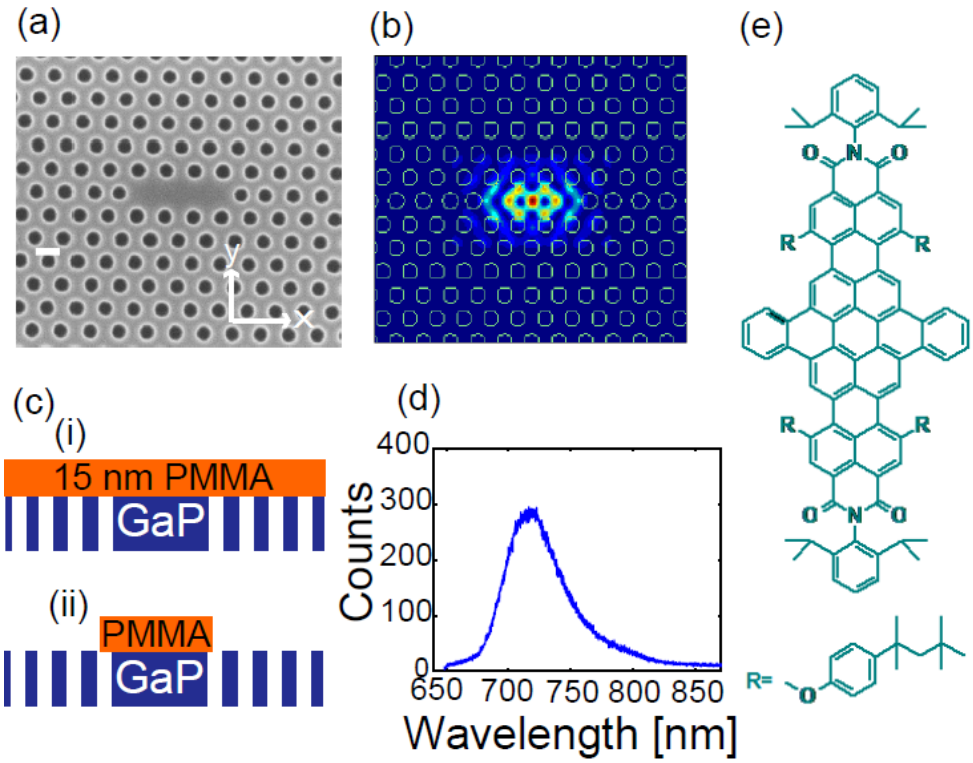

Figure 6-1: a) SEM image of a fabricated photonic crystal cavity in GaP. Scale bar indicates 200nm. b) FDTD simulation of electric field intensity of the fundamental cavity mode. The mode is primarily y-polarized. c) Schematic illustrating fabrication procedure. (i) DNQDI/PMMA is float-coated over the entire structure. (ii) DNQDI/PMMA is lithographically defined over cavity region. d) Bulk fluorescence emission spectrum of DNQDI when excited with a 633 nm HeNe laser measured with a confocal microscope and spectrometer. The molecule has a peak in its absorption at this excitation wavelength. e) Chemical structure of DNQDI molecule. (After Ref. [17])

Our cavity is a linear three-hole defect (L3)[14] fabricated in a 125-nm gallium phosphide membrane grown by gas-source molecular beam epitaxy. A scanning electron microscope (SEM) image of a fabricated cavity and the simulated electric field intensity of the fundamental high-Q cavity mode are shown in Figure 6-1a,b. Cavities are fabricated as described in Ref [9]. The molecule we use is

dinaphthoquaterrylene diimide (DNQDI), which was chosen for its broadband emission over the desired wavelength range, 700 nm-850 nm, good photostability, and high fluorescence quantum efficiency (QE = 40%)[15]. The structure of the molecule and its emission spectrum are shown in Figure 6-1. To couple DNQDI to photonic crystal cavities (Figure 6-1c), the molecule was dissolved into a solution of 1% poly(methyl methacrylate) (PMMA) in distilled toluene. In standard lithographic processing, this solution is then spun onto a surface, leaving behind a smooth, thin film of dye-doped polymer resist. However, spinning onto an uneven surface, such as a photonic crystal membrane, causes unwanted aggregation of the dye-doped PMMA. Instead, the solution was float-coated[16], whereby the photonic crystal sample is submerged into a water bath and a single drop of the dye-doped PMMA in toluene solution is dropped onto the surface of the water bath. The drop quickly disperses across the surface leaving a locally uniform layer of hydrophobic dye-doped resist floating on top of the water bath. The water is then pipetted away, allowing the PMMA layer to gently rest on top of the photonic crystal sample. The sample is baked at 90°C for 30 minutes to ensure that all the water is fully evaporated. The concentration of DNQDI in the PMMA layer is approximately 5 molecules/100 nm^2.

6.3 Optical Characterization of High Q Cavity Modes

We first characterize cavities passively prior to depositing molecules. We probe cavity resonances using cross-polarized normal-incidence reflectivity with a tungsten halogen white light source[9]. The cross-polarization configuration is used to obtain a sufficient signal-to-noise ratio to observe the cavity resonance above the

reflected background uncoupled to the cavity. A typical reflectivity spectrum is shown in Figure 6-2a, showing the multiple resonances of the L3 cavity; the fundamental mode is denoted with a black box. The spectrum of the fundamental mode (Figure 6-2b) is fit to a Lorentzian, giving a quality factor of 10,000. The improvement in quality factor from Ref.[9] is due to better fabrication.

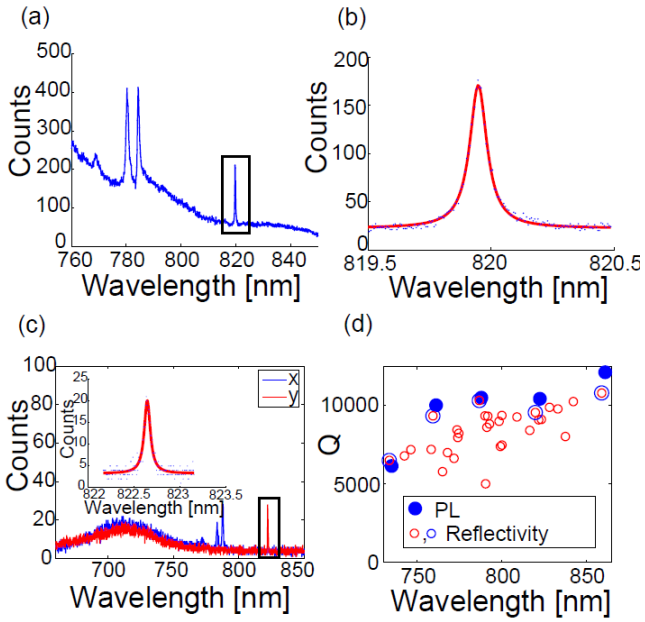

Figure 6-2: a) Cross-polarized reflectivity measurement of a cavity. The box indicates fundamental cavity mode. b) Reflectivity spectrum of high quality factor fundamental cavity mode [box in (a)]. Spectrum shows additional peaks at shorter wavelengths from higher order, but lower Q, cavity modes. Solid line shows Lorentzian fit with quality factor 10,000. c) Fluorescence collected using a confocal microscope (approximately diffraction-limited collection) and spectrometer from the same photonic crystal cavity in (a) and (b) after molecules are deposited on cavity. X-polarized emission is shown in blue; Y-polarized emission is shown in red. Inset: Fluorescence measurements of fundamental cavity mode (black box). Line indicates Lorentzian fit with Q = 10,000. d) Quality factors measured for high-Q cavity mode from reflectivity (open circles) before molecule deposition and fluorescence after molecule deposition for structures with lattice constant a and hole radius r/a tuned so that the fundamental cavity resonance shifts across the fluorescence spectrum of the molecule. Blue open

circles indicate reflectivity measurements for the cavities that were also measured in fluorescence (blue closed circles). (After Ref. [17])

6.4 Fluorophore-Cavity Coupled Fluorescence Emission Spectra

After characterizing the structure initially, a molecule-doped polymer film is float-coated on top of the entire sample. We measure fluorescence from the molecule (Figure 6-2c) using a 633-nm helium-neon excitation laser in a confocal microscope setup. When measuring fluorescence from the cavity region (collected from an approximately diffraction-limited area) of a photonic crystal cavity, we observe sharp polarized resonances identical to those in our reflectivity measurements, demonstrating the molecules are coupled to the cavity modes. From confocal images taken from the cavity (Figure 6-3a), <10% of the emission is from molecules coupled to the cavity region, but spectra of these coupled molecules are still visible over background from uncoupled molecules since molecules coupled to the cavity emit only at a few wavelengths. The quality factor of the fundamental mode is measured to be 10,000, indicating that deposition of molecules onto the membrane does not degrade the properties of the cavity, in agreement with finite difference time domain simulations for a thin (<40 nm-thick) layer of PMMA. It is worth noting that even though the bulk emission spectrum of the molecule does not show much emission at the longest wavelengths, nevertheless there are molecules emitting there, an effect which can be observed when the molecular emission is coupled to the cavity.

After deposition of molecules, we observe a small (several nm) red-shift in the cavity resonance, as expected from simulations. With no DNQDI/PMMA present, only background counts are detectable over the entire spectral range. We vary the spatial periodicity of the photonic crystal holes and hole radius to tune the fundamental cavity resonance through the fluorescence spectrum of the molecule. We measure high cavity Q factors up to 12,000 via fluorescence (Figure 6-2d) across a range of more than 100 nm, from 735 nm-860 nm. The cavity Q is higher at longer wavelengths, where we fabricate most of our cavities, as fabrication imperfections are reduced because the feature sizes are larger. Small differences in cavity Q measured with reflectivity versus fluorescence (Figure 6-2d) are primarily due to fit error.

6.5 Lithographically Defining Molecule Position over Photonic Crystal Cavity

Since the molecules are doped into PMMA, an E-beam lithography resist, it is straightforward to selectivity expose and develop the polymer film using E-beam lithography[18] so that molecule-doped PMMA remains only at the location of the photonic crystal cavity (Figure 6-1c). While float coating deposits resist uniformly over a small region, PMMA thickness variations were observed from one coating to the next, so electron beam doses were varied for different cavities on one sample. Figure 6-3a shows a scanning confocal image of photoluminescence from a photonic crystal cavity coated with DNQDI-doped PMMA before patterning. The fluorescence is flat to within 3.5%, with slightly more emission from the cavity region, likely a result of enhanced outcoupling from molecules coupled to the cavity mode.

Using the Raith150 E-beam lithograpy tool, it is possible to expose an area of resist based upon alignment marks located on the sample. During the initial electron-beam lithography step that defines the photonic crystals, alignment marks were also written. After photonic crystal fabrication and float coating of dye-doped resist, the sample is then reloaded into the Raith150. Depending upon the size of the alignment marks, this second write can be aligned to the initial photonic crystal write to within 20 nm. In this way, all of the unwanted resist can be selectively exposed, leaving the cavity's resist untouched. A simple development step removes the E-beam exposed resist and leaves behind a photonic crystal with the cavity region coated in fluorescent molecules. Figure 6-3a,b are confocal fluorescence images of a cavity before and after electron-beam exposure and development, measured with the same excitation power. There is still strong emission from molecules coupled to the cavity after exposure, though diminished by the exposure process, but there is no emission from the nearby areas. The contrast in Figure 6-3b is higher, showing that by removing the molecules, the background signal from molecules not located over the cavity is much lower. Figure 6-3c shows a PL spectrum (Q=4500) measured on the same cavity after localization of the resist to the cavity, demonstrating that the remaining molecules are still spectrally coupled to the photonic crystal cavity. An atomic force microscope image (Figure 6-3d) confirms that DNQDI-doped PMMA from Figure 6-3b is localized to the cavity and is 12 nm in height and 700 nm by 400 nm laterally. The AFM image shows a misalignment of approximately 300 nm between the cavity region and the lithography defined DNQDI/PMMA region. With optimization of the overlay process, it should be possible to reduce this error to less than 50 nm.

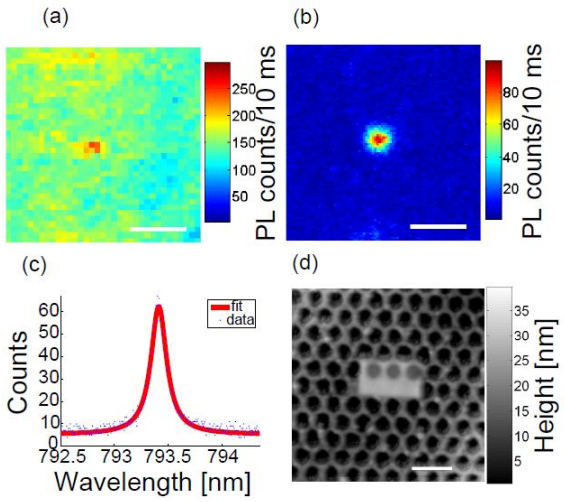

Figure 6-3: Aligning molecules to a photonic crystal cavity. a) Scanning confocal image of fluorescence from DNQDI-doped PMMA float-coated onto a photonic crystal membrane. Pixel size is 200nm and scale bar indicates 2 μm. b) Scanning confocal image of DNQDI fluorescence after E-beam lithography is used to remove all molecules, except for the ones coating the cavity region at the center. The same imaging laser power as in (a) was used. Pixel size is 80nm and scale bar indicates 2 μm. c) Fluorescence spectrum from the fundamental mode of photonic crystal cavity after selective removal of molecules by E-beam lithography. d) Atomic force microscopy image showing localization of DNQDI-doped PMMA to the cavity region. PMMA thickness is 12nm. Scale bar indicates 500nm. (After Ref. [17])

6.6 Conclusions

In conclusion, we have demonstrated the coupling of fluorescent molecules to photonic crystal cavities with resonances in the far-red and near-infrared wavelengths and quality factors up to 12,000. By exposing and developing the molecule's polymer host using E-beam lithography, we have also been able to localize the molecules to the cavity region exclusively. Our results show that molecules can be coupled to high

quality factor photonic crystal cavities as well as localized to the nanoscale cavity using standard lithographic techniques.

References

1. Noda, S., Fujita, M. & Asano, T. Spontaneous-Emission Control by Photonic Crystals and Nanocavities. *Nature Photonics* **1**, 449 (2007).

2. Englund, D. *et al*. Controlling Cavity Reflectivity with a Single Quantum Dot. *Nature* **450**, 857 (2007).

3. Yoshie, T. *et al*. Vacuum Rabi Splitting with a Single Quantum Dot in a Photonic Crystal Nanocavity. *Nature* **432**, 200 (2004).

4. Altug, H., Englund, D. & Vuckovic, J. Ultrafast Photonic Crystal Nanocavity Laser. *Nature Physics* **2**, 484 (2006).

5. Barth, M., Nusse, N., Lochel, B. & Benson, O. Controlled Coupling of a Single-Diamond Nanocrystal to a Photonic Crystal Cavity. *Opt Exp* **34**, 1108 (2009).

6. Barclay, P., Santori, C., Fu, K. -., Beausoleil, R. G. & Painter, O. Coherent Interference Effects in a Nano-assembled Diamond NV Center Cavity-QED System. *Opt Exp* **17**, 8081 (2009).

7. Hennessy, K. *et al*. Quantum Nature of a Strongly Coupled Single Quantum Dot-Cavity System. *Nature* **445**, 896 (2007).

8. Thon, S. M. *et al*. Strong Coupling through Optical Positioning of a Quantum Dot in a Photonic Crystal Cavity. *Appl. Phys. Lett.* **94**, 111115 (2009).

9. Rivoire, K., Faraon, A. & Vuckovic, J. Gallium Phosphide Photonic Crystal Nanocavities in the Visible. *Appl. Phys. Lett.* **93**, 063103 (2008).

10. Choi, Y. -. *et al*. GaN Blue Photonic Crystal Membrane Nanocavities. *Appl. Phys. Lett.* **87**, 243101 (2005).

11. Barth, M., Kouba, J., Stingl, J., Lochel, B. & Benson, O. Modification of Visible Spontaneous Emission with Silicon Nitride Photonic Crystal Nanocavities. *Opt Exp* **15**, 17231 (2007).

12. Makarova, M., Vuckovic, J., Sanda, H. & Nishi, Y. Silicon-based Photonic Crystal Nanocavity Light Emitters. *Appl. Phys. Lett.* **89**, 221101 (2006).

13. McCuthceon, M. & Loncar, M. Design of a Silicon Nitride Photonic Crystal Nanocavity with a Quality Factor of One Million for Coupling to a Diamond Nanocrystal. *Opt Exp* **16**, 19136 (2008).

14. Akahane, Y., Asano, T., Song, B. & Noda, S. High-Q Photonic Nanocavity in a Two-Dimensional Photonic Crystal. *Nature* **425**, 944 (2003).

15. Avlasevich, Y., Muller, S., Erk, P. & Mullen, K. Novel Core-Explanded Rylenebis(Dicarboximide) Dyes Bearing Penatcene Units: Facile Synthesis and Photophysical Properties. *Chem. -Eur. J.* **13**, 6555 (2007).

16. Zhou, H. *et al*. Lithographically Defined Nano and Micro Sensors using "Float Coating" of Resist and Electron Beam Lithography. *J. Vac. Sci. Technol. B* **18**, 3594 (2000).

17. Rivoire, K. *et al*. Lithographic Position of Fluorescent Molecules on High-Q Photonic Crystal Cavities. *Appl. Phys. Lett.* **95**, 123113 (2009).

18. Martiradonna, L., Stomeo, T., De Giorgi, M., Cingolani, R. & De Vittorio, M. Nanopatterning of Colloidal Nanocrystal Emitters Dispersed in a PMMA Matrix by E-beam Lithography. *Microelecton Eng* **83**, 1478 (2006).

Chapter 7 – Conclusions

7.1 Conclusions

Fluorescence is an important technique used throughout biology and so understanding how molecule-light interactions can be altered using nanophotonic structures is an important field of study. This thesis has shown that molecular fluorescence can be controlled using the bowtie nanoantenna as well as the photonic crystal cavity.

Chapter 3 discussed the exceptionally large enhancement of a single molecule's fluorescence caused by coupling the molecule to a lithographically-fabricated gold bowtie nanoantenna. When an initially low QE fluorescent molecule is positioned in the gap of a bowtie nanoantenna with its transition dipole moment oriented correctly, its fluorescence is increased roughly 1,300-fold. This enhancement was found to be due to an increase in the absorption of light by the molecule, as well as a to shortening of the molecule's lifetime leading to an overall increase in the QE. This result is useful in fields which require single-molecule sensitivity in highly concentrated samples.

The above work is extended in Chapter 4 to show that enhancements of fluorescent molecules in liquid environments are possible. It was found that single-molecule FCS experiments could be performed on relatively high concentrations of molecules. The only molecules that had measurable enhancement were ones that

adhered to the surface near the bowtie nanoantenna. FCS experiments showed that the photobleaching time scaled inversely with the excitation intensity. These results suggest that experiments on enzymes bound to a surface that act on fluorescently-tagged substrate molecules at high concentrations are possible with bowtie nanoantennas.

Chapter 5 takes a different approach from the previous chapters. Instead of randomly positioning molecules around the bowtie nanoantenna, the goal of this work was to fabricate a bowtie nanoantenna on the end of a scannable AFM tip, so that the bowtie could be positioned precisely above a molecule. The fabrication of a resonant bowtie nanoantenna onto an AFM tip proved difficult to achieve with E-beam lithography due to problems with liftoff. Bowtie nanoantennas were eventually fabricated onto AFM tips using FIB milling, but these antennas were not resonant and did not enhance the fluorescence of the molecule TPQDI, likely due to gallium implantation from the FIB milling. Chapters 3 and 4 show that if fabricated successfully, a bowtie nanoantenna AFM tip could be a useful device for studying nanoscale emitters and enhancing their fluorescence thus extending the ANSOM and related near-field imaging technique.

Finally, Chapter 6 considers a very different nanophotonic structure: the photonic crystal cavity. A lithographic approach to positioning molecules on the cavity was developed, whereby a dye-doped polymer film is float-coated onto the entire photonic crystal and E-beam lithography/development removes all dye-doped resist everywhere except the photonic crystal cavity region. These molecules were shown to be spectrally coupled to the photonic crystal cavity. By successfully

positioning molecules lithographically on top of the cavity region, molecules are attractive candidate for future quantum optics experiments on single nanoscale emitters with well-defined structure.

7.2 Future Outlook

The bowtie nanoantenna has been shown to be a very useful structure for enhancing optical emission, whether it arises from fluorescence[1] or Raman scattering[2]. This thesis has shown that bowtie nanoantennas can be used to perform single-molecule experiments in crowded situations, whether in solid or solution environments. Many biological systems, such as DNA replication and RNA translation, require high fluorophore-tagged substrate concentrations in order for the enzymes to perform well and to replicate biologically relevant behavior. At the present time, research groups and start-up companies, such as Pacific Biosciences, use zero-mode waveguides (ZMG) to sequence DNA[4], but ZMG's have only been shown to enhance the fluorescence of single molecules by factors up to 25[5]. Bowtie nanoantennas could potentially replace zero-mode waveguides since they show much higher fluorescence enhancements. When a fluorescently-labeled substrate molecule binds to biological machinery (e.g. an enzyme) located within the gap of the bowtie nanoantenna, then the fluorophore is significantly enhanced compared to the other very weakly emitting molecules not located in the gap region but still within a diffraction-limited laser focal spot. Thus, the bowtie could provide a contrast enhancement device to monitor enzyme activity optically and in real-time.

A second possible use for a single molecule coupled to the bowtie nanoantenna is as a single-photon source. Single-photon sources are single emitters that can only emit a single photon upon each absorption event. By coupling a molecule to the bowtie nanoantenna, the fluorescence from the molecule is increased up to a factor of 1,300 and the lifetime is shortened by a factor ~20. This means that the bowtie-molecule system could potentially emit photons very quickly, because the excited state lifetime is shortened. This system could be very useful in quantum cryptography applications where single-photon sources ensure security of encrypted data.

In summary, this thesis has shown that the bowtie nanoantenna and photonic crystal cavity are very useful structures in the field of fluorescence research, especially in the single-molecule regime. Bowtie nanoantennas could potentially aid experiments that need single-molecule sensitivity in crowded environments, while the lithographic approach to defining molecule on a photonic crystal cavity gives a new approach to solve a problem that has plagued the photonic crystal community.

References

1. Kinkhabwala, A. *et al*. Large Single-Molecule Fluorescence Enhancements Produced by a Gold Bowtie Nanoantenna. *Nat. Photonics* **3**, 654 (2009).

2. Fromm, D. P. *et al*. Exploring the chemical enhancement for surface-enhanced Raman scattering with Au bowtie nanoantennas. *J. Chem. Phys.* **124**, 061101 (2006).

3. Eid, J. & et. al. Real-Time DNA Sequencing from Single Polymerase Molecules. *Science* **323**, 133-138 (2009).

4. Aouani, H. *et al*. Crucial Role of the Adhesion Layer on the Plasmonic Fluorescence Enhancement. *ACS Nano* **3**, 7 (2009).

Appendix A - EBL using Raith 150

A.1 Writing Bowtie nanoantennas with Raith 150

1. Load Samples

- Remove the stage from the vented system and load samples.
- Replace stage and click "Load Sample" button.
- Important: be sure to squeeze door until the pump engages – otherwise you will get a load lock error and have to call James Conway or a Raith champion to proceed.

2. Initial Setup

- Drive stage to home position? → click "yes"
- Reset coordinate system? → click "yes"
- Enter sample name → Name your sample
- Set Column → 10 KV
- Set Aperture → 10 μm
- Set Working Distance → 5 mm
- Set stigmation & aperture alignment to database values? → click "yes"
- Note that these are the settings for bowtie nanoantennas on glass. If larger apertures/column voltages are used, the writes will be faster but the feature size will suffer.

3. Measure Beam Current

- Drive sample to correct Z position by setting Z position in "Stage Control" to 20mm in Absolute & XYZ and then clicking GO!
- Click "go to Faraday cup on Holder."
- Start the beam on the left computer

- Start imaging on the right computer
- Open control panel on right computer
- Make sure that in detectors tab: Signal A = InLens
- Move until centered on the cup (black hole)
- Click Measure Current → should be ~0.01 nA for 10μm aperture at 10kV

4. Setup sample coordinate system

- On left computer's microscope control box: set mag to "1000X, 100μm" – make sure NOT to select "100x, 1000μm"!
- Check database values, click Set
- Go to your sample by going to correct clip (clip 1-6)
- Start imaging, move to lower left corner of coverslip
- Set origin correction, click Adjust
- Set angle correction using 2 points on the bottom of the sample
- Note that setting the origin and angle correction will help if you need to image your sample after measuring it optically – otherwise it will be difficult to locate the bowties by SEM blindly.

5. Set up the electron beam – Gun Align

- Move to a spot near where we want to write, but still ~1mm away.
- Click Apertures Tab
- Click emission mode (near gun align button)
- Click gun align button
- Go to imaging mode 4
- Open crosshairs, center the crosshairs in the circle
- Click normal mode

6. Setup the electron beam – Aperture Align

- Focus sample and burn calibration spot
- First, attempt to focus on dirt on the sample. If there is no dirt in the nearby area, try burning a really long calibration dot by pressing the crosshair button with the center mouse button and focus on that

- Move to magnification high enough to see 100nm features
- Burn a new calibration dot.
- Turn on focus wobble
- Optional - use reduced raster scan area, often helpful in stigmation
- Click aperture align
- If the aperture is misaligned, the dot will move as the focus is wobbled in and out of focus. Move the x and y scrollbars until image stays centered in focus wobble (it will still streak though due to astigmation, but the center of mass of the spot will stay in the same position)
- Turn off focus wobble

7. Setup the electron beam - Astigmation

- Click "Stigmation"
- Burn a new calibration dot
- Move the x and y scrollbars until the spot appears small and sharp. You will need to alternate between x-stigmation, y-stigmation, focus and burning new calibration dots in order to get a <20nm calibration dot.

8. Align Writefield

- Burn a bright spot in a recognizable place (away from any other calibration dots)
- Open new positionlist
- Go to Scan Manager Box -> Align write field procedures → manual → "100WF -Manual 5um mark" and drag to new positionlist
- Add 10-15% to contrast on right computer
- Start scan
- CTRL+left click will drag the mark onto the burned spot. Do this 4 times
- Accept new align writefield values.

9. Level the sample using three points sample leveling

- Pick 3 points close to the write area, type coordinates for 3 points into U/V boxes

- For each of the 3 points: focus and burn dots, tick 1st tickbox, go back to first burned spot, click adjust, go to next point.
- Repeat, go through all points again, until they are all in focus.
- Check that the sample is leveled well, by attempting to burn a calibration dot somewhere in the intended write region. If a dot cannot be burned easily, redo this step.

10. Set Doses

- Exposure window → Open dose calculator
- Set doses: area = 110, line = 300, dot = 0.01
- Set stepsize (1.6nm)
- Calculate dwelltime by clicking on calculator
- Note – this needs to be done after measuring the beam current (step 3), otherwise it will incorrectly calculate the dwelltime.

11. Make sure the focus is set for the write.

- Adjust UVW Window → Adjust W → click Read, then adjust

12. Write

- Setup up position list with your patterns
- On position list: Scan all!

Appendix B - Focused Ion Beam Lithography with FEI Strata

This appendix contains instructions for running the FEI Strata dual beam FIB, as well as additional tips for patterns with small features (<50nm). Please note that these instructions are not a substitute for the required training sessions with a FIB trainer. Check the latest training protocol to see current requirements for use of and training on the FEI Strata.

B.1 Start-up

1. Log in

- Log into CORAL with your CORAL id and password. Enable the FIB.
- Log in to the FIB computer with your user id and password.

2. Check Vacuum status

- Check that the Vacuum and High Tension (HT) hardware buttons are lit. This ensures that the vacuum's turbopump is operational.

3. Turn on Ion Source

- Check that the ion source is on (button is colored yellow). If it is off (button colored gray), turn on the ion source by clicking the ion source button to warm up. Emission will fluctuate for a few minutes, but should stabilize at 2.1 – 2.3 µamps.

- The extractor is always set to 12.00 kV, but the suppressor can be changed by the user from -2150 to 2150V. If the emission is not stable between 2.1 – 2.3 µamps, slowly adjust the suppressor to compensate. If the suppressor is at its maximum value and the current is still too low, the source needs to be heated – contact a trainer or qualified user to heat the source. The FIB can still be used if the current is only slightly before 2.1 µamps, but make sure to let someone know if needs to be heated.

4. Load sample

- Choose OM in "detectors" menu. In RH start up window, choose "Vent", then "OK". Venting takes 3 – 5 minutes until the front door of the microscope can be opened.
- When vented, insert your sample:

  a) wear gloves

  b) make sure set screw is not engaged when you place your sample in the mount. Tighten the set screw gently (barely finger-tight, DO NOT OVERTIGHTEN)

  c) adjust the top of the sample to 5 mm from the lens (use eucentric height adjuster, aka. "elephant ear")

  d) watch OM image while closing the chamber door to make sure the sample does not touch the lens
- While holding the door firmly closed via the push bar, click on "pump" command. Keep pressure on the door for a few seconds; tug to check the seal.
- Click "cancel" on the "Confirm holder settings" dialog box.
- Wait until "Vac OK" message appears at the bottom of the startup page, about 3 – 5 mins.

5. Bring up electron and ion HV:

- Set electron and ion beams to 5 kV and 30 kV, respectively.
- Electron spot size is normally set at 3.
- Turn on HV for electron and ion beam by pressing "HV" buttons.

6. Set initial height

- Click very top left blue "Start/freeze scan" button in order to start SEMing.

IMPORTANT: When the scanning begins, the "e-beam confirm focus" window pops up. DO NOT CLICK "OK" ON THIS WINDOW UNTIL YOU OBTAIN A SEM IMAGE AND FOCUS AS INSTRUCTED (see following). This tells the computer how far your sample is from the lens.

- With "primary beam – E" icon highlighted, choose either the SED or CDM-E detector. During your session, feel free to test out both detectors for your sample and use the one that gives the best images.
- BEFORE ADJUSTING FOCUS, adjust your contrast/brightness knobs to give you an image. This is a general rule: if there is no image, make sure the contrast brightness settings are at reasonable values.
- Focus it as you move up to the 5000 – 8000X magnification range. Focus well, and the free working distance "FWD" (bottom of the screen) will now read the focal length of the objective lens, which equals the true distance from the sample to the bottom of the lens. Click "OK" on the pop-up window to calibrate Z to FWD.
- At this point, the SEM capabilities are set up for basic use. Translate to your sample using the joystick, mouse, and/or stage table, reconfirm Z if necessary, and you can perform any SEM imaging you need.

7. Set eucentric height

- Move to desired location on sample and click Z=FWD button.
- Eucentric height is about 5mm for this machine. On the workpage, raise the sample to 5mm and refocus if necessary.
- At 10 – 15KX, place a recognizable feature on the center crosshair.
- Tilt the sample a few degrees and re-center the feature (vertically with respect to the screen) using the "Z" knob on the stage door (not using the joystick or mouse!).

- Increment up a few more degrees and repeat. Continue (you can increase the size of the increments) until you get to 52º (perpendicular to the ion beam). Check that the feature is vertically centered at 0º and 52º.

8. Obtain ion-beam image, adjust electron/ion-beam coincidence

- After setting the eucentric height, and while still at 52º, select a relatively non-destructive ion beam aperture. The 1pA aperture can make features as small as ~30nm, while the 10pA aperture is limited to ~50nm. For bowtie nanoantennas, particularly in gold, which mills easily, the 1pA aperture was used to achieve the highest resolution.
- Check that your ion beam and electron beam mags are coupled.
- At 10 – 20KX, center a recognizable feature while still in e-beam mode.
- Choose "primary beam – I" icon and adjust contrast/brightness and focus.
- DO NOT MOVE THE STAGE! Instead, re-center the feature using the beam shift knobs (shifts the beam NOT the stage). This will align the ion beam and electron beam images

9. Proceed with your sample

B.2 Focusing and Stigmating the Electron and Ion beams

To obtain a good image and ion etching/deposition results, you must stigmate and focus both the electron and ion beams properly. This takes practice. As you learn how to operate the instrument, make sure you are learning these procedures well as they will determine the smallest feature size possible with the FIB.

Focusing and astigmatism corrections should be made at least one magnification step above where you want to take a final image. These procedures are

identical for both beams. Be aware of possible beam damage as you align, so you may want to adjust these away from your area of interest.

1. Focusing

- Use the hardware knobs or right-click and drag the mouse.
- Be aware of the sensitivity of the coarse and fine focus knobs, as one or the other will make more sense depending on your magnification.
- If you are grossly out of focus, reset the focal length to something that makes sense (near 5mm if you mounted the sample properly) and work from there. This is particularly helpful if you are zoomed out completely and the focus changes quickly.

2. Astigmatism

- If the out-of-focus image is streaky, and the streakiness changes direction 90º on either side of focus, there is astigmatism. Astigmatism also causes a loss of resolution at focus.
- Important - The specimen should be at the center of focus before beginning. This means that there is no streakiness in the image – it is uniformly blurry. This will make the stigmating the beam much easier.
- Adjust the stigmators one at a time to obtain the sharpest image.
- After adjusting the X and Y stimators once, re-focus and check for streakiness. Iterate between focus and X/Y stigmators as needed. If necessary, start at a lower mag and repeat the adjustment at the higher mag. Check your final focus.

3. Aperture alignment

- If the image moves as you change focus, focus as best you can, then choose the lens alignment icon.
- Focus wobble will be engaged, causing the focus to wobble back and forth through the center of focus.

- Click and drag on the crosshairs in the pop-up window to minimize image movement.
- Deselect the lens alignment icon, and check that the image no longer sweeps.

B.3 Milling with the Ion Beam

1. Setup Ion beam for imaging

- Choose the appropriate aperture for your feature.
- Adjust contrast/brightness, focus, and coincidence (you may have to work very quickly if you use a large aperture).
- Freeze the image or grab a 1–Ion beam frame.

2. Setup Pattern

- Select the pattern shape(s) from the icons along the menu bar and draw what you want to mill. If complicated patterns are required, contact experienced users for ways to draw patterns offline in Matlab.
- On the work page, select serial (sequential) or parallel milling.
- Make sure "ion beam" is selected as the beam you will use (and is the primary beam).
- Choose the appropriate material resource file. The si.mtr file can generally be used regardless the actual material. The actual depth will need to be calibrated for any material.
- Adjust the milling dimensions as required; the computer will determine the approximate milling time.
- Grab a 1-I frame again to check the setup.
- Click "start/stop patterning" icon to begin the mill. You can take 1-E and 1-I frames as you mill.

B.4 Pt deposition with the Ion Beam

1. Setup Ion Beam for imaging (as described for milling)

2. Turn on Pt heater and insert GIS needle

- Turn on the Pt heater and allow it to warm up (indicator becomes red) before use.
- **Make sure you are at eucentric height** and insert the Gas Injection System (GIS) Pt needle. If you are above eucentric height, then the needle will hit the sample! Inserting the needle may cause a small shift in the image (both location and contrast/brightness), so check pattern positioning after inserting.

3. Choose appropriate ion beam aperture

- Use the following rule to choose the ion beam aperture

$$2 * \text{Area}_{\text{pattern}}(\mu m^2) \leq \text{Aperture size (pA)} \leq 6 * \text{Area}_{\text{pattern}}(\mu m^2)$$

4. Retract the needle

- **Make sure to retract the needle** when you are finished depositing. Do not translate or change tilt with the needle inserted.

B.5 Shutdown

1. Turn off GIS sources

- Make sure any GIS needles are retracted and their heaters are turned off.

2. Return to home settings

- Return to a 10pA ion beam aperture.
- Return sample tilt to 0º.
- If using "UHR" mode, return to "SRH" (search) mode.
- Set both x and y to 0.

3. Turn off CDM-E detector

- Make sure that contrast and brightness for CDM-E detector are zero. This detector needs to be turned off in this way to reduce wear. Check that it is off

even if you did not use this detector – sometimes it is used by accident or a previous user forgot to turn it off

- Select SED detector. This detector can be left with its contrast/brightness settings on.

4. **Turn off beams**

- Turn off electron and ion high voltage by deselecting "HV" for both.
- Leave the ion source on if the next user will be on within 4-6 hrs; else turn off the ion source.

5. **Vent the chamber. Select OM.**

6. **Remove your sample.**

7. **Pump the chamber**

- Make sure you obtain the "Vac OK" message. If the chamber is not pumping down correctly, do not leave it pumping indefinitely or you will damage the turbopump.

8. **Select SED to turn off the OM.**

9. **Log out of the system.**

10. **Clean up after yourself as you leave the room.**

11. **Disable the FIB from CORAL.**

Appendix C - Confocal microscope operation

This chapter is an updated version of a guide previously published by Dave Fromm in his Ph.D. thesis[1].

C.1 Introduction

The following guide will provide instructions to enable a new microscope user to use the modified Topometrix microscope system in all of its modalities. The user is encouraged to consult the Topometrix User's Manual, as there is a wealth of information available there. This appendix will attempt to clarify the manual, where applicable, and provide caveats learned throughout the development of this instrument. Despite its supposedly commercial nature, this instrument is not easy to use and only two or three of these units were ever manufactured. Therefore, this instrument should be thought of as completely home-built. Several components have been modified from original parts, but, as there is no service offered for this instrument, this is not important. If there are any serious issues, the user is encouraged to talk to Dr. Stefan Kaemmer at Veeco, who is one of the systems original designers

Despite these warnings, this instrument is incredibly versatile and offers stable mechanical components that can produce excellent AFM images concurrently with

optical images. This platform serves near-field and far-field imaging experiments well.

C2. Input Optics

Figure C-1 shows the microscope and its various components in its entirety, which can be broken up into the following general components: input optics, microscope parts, output optics, and AFM parts. The optical parts will be discussed here, with AFM operation discussed later. Figure C-2 shows the important confocal microscope input optics, discussed here.

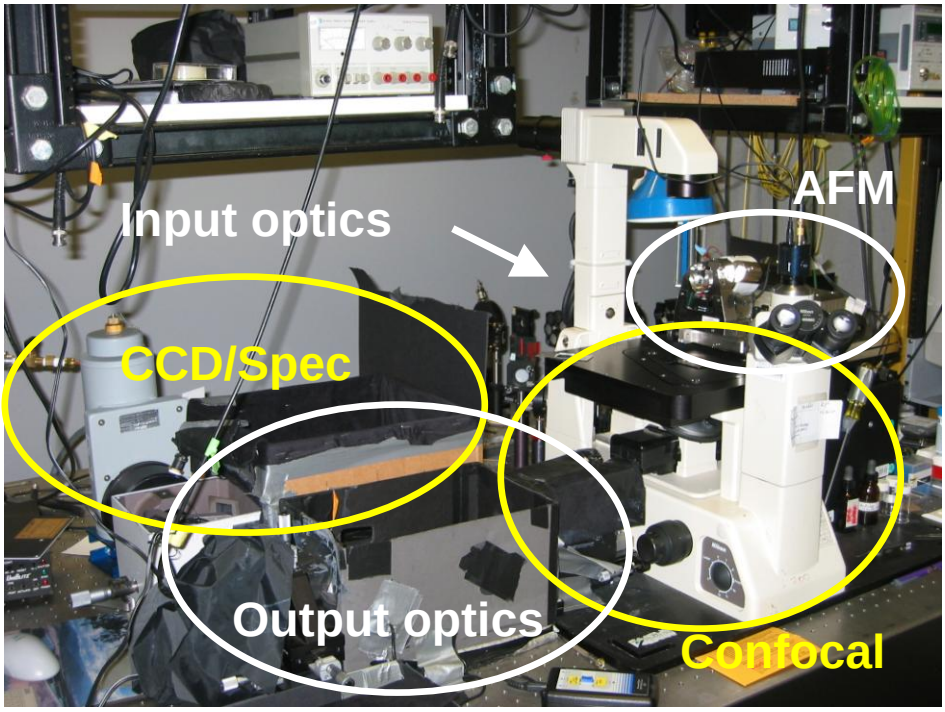

Figure C-1: General microscope view. Note several components, including input optics, output optics, AFM head, the microscope, and the CCD/Spectrometer.

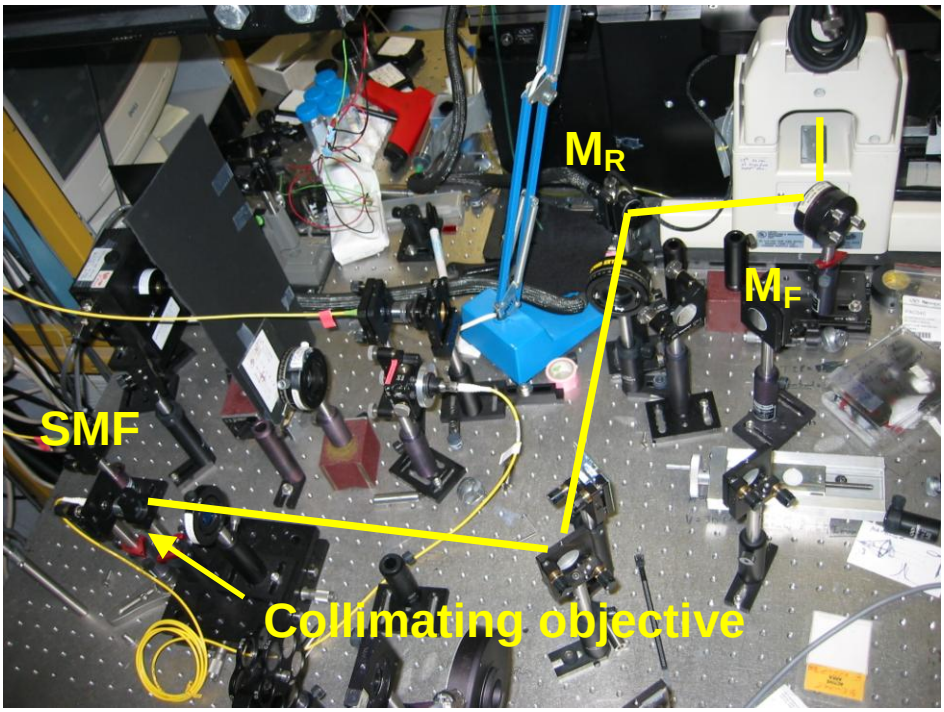

Figure C-2: Input optics for confocal microscopy, including the single-mode fiber (SMF), which is a spatial filter; the collimating objective (NA 0.18); the rear mirror (M_R) and the final mirror (M_F).

C.1.1 Gaussian Beam Profile

When creating a confocal excitation beam path, it is important to have some sort of a *spatial filter* to produce a clean, diffraction-limited spot before entering the microscope. Note that taking great care in producing a clean focal spot at the sample both lowers background (noise) and increases signal, both of which are important for single-molecule microscopy.

For laser diodes, the emission is often a "cat eye" shape, far from the ideal Gaussian beam shape. The most widely used method for producing a clean beam is sending the beam through a single-mode fiber (SMF in Figure C-3). Laser couplers are available in the lab that have a built-in lens (L1 in Figure C-3). The core of a SMF

is small (typically 1.5 – 3 μm in diameter) and the output should be perfectly Gaussian. You can check this by imaging the output onto an index card or beam profiler. If the beam is distorted, then either the fiber is dirty or damaged. The end facets of the SMF can be cleaned dragging a MeOH coated lens tissue over the surface of the fiber. If one end of the fiber is slightly damaged, you can still use it – just make sure the perfect end is the fiber output (to microscope). Coupling efficiency will suffer, but generally plenty of power is available for confocal experiments. Finally, the mode output of the fiber (labeled on the fiber end) is important to consider: the IR fiber currently installed is good for ~ 700 – 900 nm, but has low transmission in the visible.

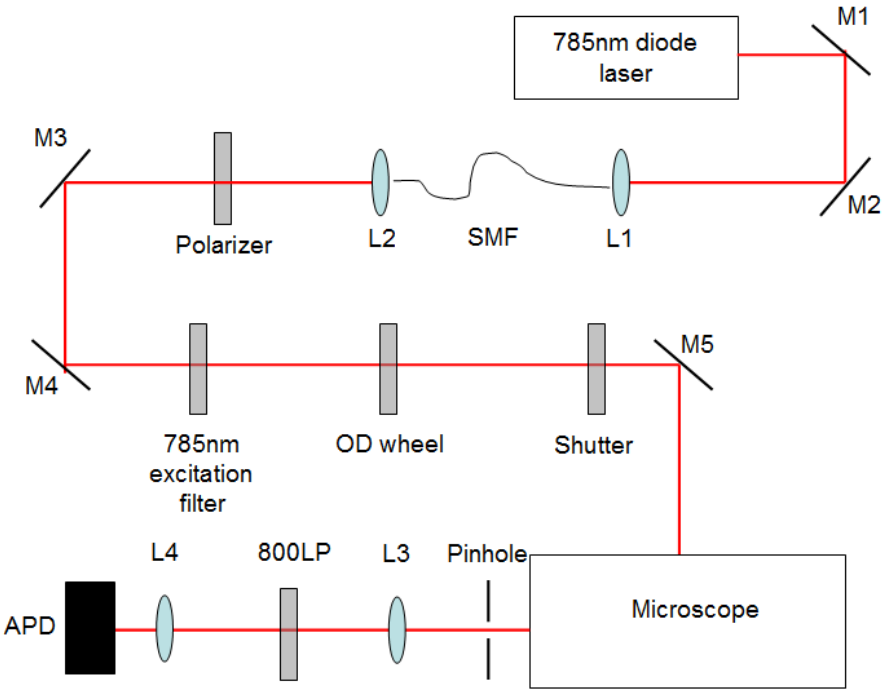

Figure C-3: Schematic of typical optics used for a confocal microscope. A single-mode fiber (SMF) is used to produce a Gaussian beam profile for the excitation path, followed by additional optics that control the beam's polarization, power and spectrum. The beam path is a confocal setup because the

emission pathway is focused through a pinhole, allowing for z-sectioning. An emission filter ensures only fluorescence reaches the detector.

SMF's are delicate optical components, so care should be taken when using them. Do not kink the fibers at all, because they will break! They are not cables, and must be treated with care – the maximum diameter of curvature that one should impart on a SMF is ~ 8". For excess fiber, bundle it up and tie-wrap it together, tying it to the racks out of the way. Also, be sure the keep the ends capped when not in use in order to prevent dust from accumulating on the end faces.

After the beam exits the SMF, it needs to be re-collimated using a lens. An objective is currently used (L2 in Figure C-3). It is important for NA of the objective lens should match that of the SMF, which is about 0.1 – 0.2 for most fibers. The output beam should be perfectly collimated, which should be checked by shooting the beam across several meters of free-space (mirrors help here) and imaging the spot on a card or beam profiler. Make sure there are no foci in the beam, that the intensity profile is perfectly symmetrical (if not, the output of the fiber is tilted with respect to the objective) and that it is Gaussian in shape. It is helpful to take a beam stop and put an index card on it with a mark signifying the height of the fiber output (which should be equal to the microscope input height for ease of alignment). Use this beam stop to center the height of the output from the collimating objective and after reflecting off of each successive mirror, letting the beam shoot across the table to make sure you are perfectly level.

When you cannot use a fiber (e.g. using the pulsed laser, since fibers broaden the pulse-width), a 500 – 800μm pinhole also works as a spatial filter. Shoot a

collimated laser beam into this pinhole and let the beam diffract out from there. You can typically get ~ 25% of the laser through this pinhole (depends on pinhole size and laser beam used). This output beam will need to be allowed to slowly diffract out to a large enough diameter to overfill the back aperture of the microscope. While only pseudo-collimated, this technique produces an excellent confocal spot.

C.1.2 Beam Size

Once the beam is Gaussian and collimated, it should also have a beam diameter that is **greater than or equal to** the back aperture of the microscope objective used. If this condition must be satisfied in order to obtain diffraction-limited images. By choosing the collimating objective wisely (NA = 0.18 is currently used), the beam will have the correct size already, but a telescope can be built to magnify the beam if necessary.

C.1.3 Excitation Filter

Diode lasers do not emit at a single wavelength, but rather have a spectrum sharply peaked at the desired wavelength. The tails of this spectrum are weak in comparison to the peak, but for single-molecule spectroscopy every photon that leaks into the emission pathway counts and these background photons will overwhelm the fluorescence signal. You will need to filter the laser to a narrow excitation band by buying the appropriate laser line pass filter (such as 785nm excitation filter shown in Figure C-3) from Chroma Engineering or Omega Optical. In addition, if a fiber is used in the excitation beam path, a laser line pass filter will reject Raman scattering

from the fiber, which is particularly important when working far from the optimal fiber wavelength.

C.1.4 Polarization

For any imaging system, it is important to know and control the polarization of the excitation beam path. The easiest polarization to work with is linear and can be achieved with a linear polarizer (labeled polarizer in Figure C-3). Linearly polarized light that is polarized horizontally or vertically with respect to the table will bounce off of dichroic mirrors and preserve its polarization. Half wave plates can be used to rotate the polarization and quarter wave plates can be used to create circularly polarized light, but be careful: dichroic mirrors will not preserve the polarization of circularly polarized light or light polarized along other axes! Great care is needed to excite a sample with perfectly circularly polarized excitation.

C.1.5 Alignment into Microscope

Two mirrors are used to couple light into the back of the microscope, because the beam needs to enter in a perfectly straight line. These two mirrors allow one to "walk" the beam, if it is coming in at an angle. The mirror closest to the microscope (M5 in Figure C-3) is the one that is used for angular adjustment of the beam, and the previous mirror (M4 in Figure C-3) is used for positional beam adjustment. If further mirrors are used, only the final two mirrors should be used for the final beam alignment. Figure C-4 shows images of the beam in various states of alignment. To accomplish this walk, use the following method:

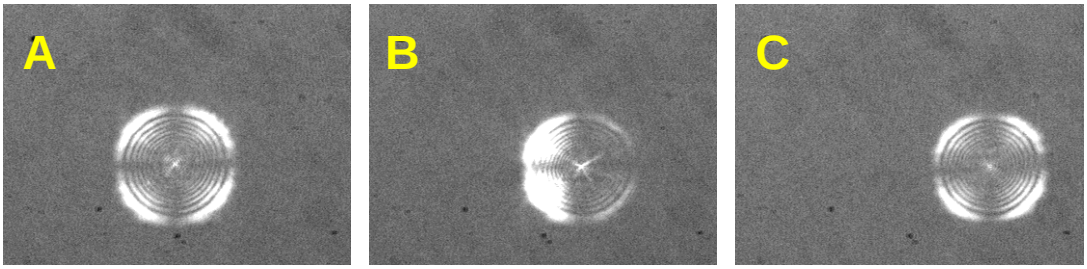

Figure C-4: Alignment of the confocal beam using the Genwac CCD camera. (a) The beam is centered in intensity, but off of the ideal optical axis (need to walk beam using both mirrors). (b) Mirror M4 adjusted to move beam closer to ideal position, but now is going in at an angle. (c) Adjust Mirror M5 angle to fix angle and achieve properly aligned beam.

1. Center beam intensity: use CCD camera, such as the Genwac. Defocus the beam slightly. The beam should have nice and symmetrical intensity. Its position may or may not be in the center of the screen. If a dichroic mirror is used (especially with linearly polarized light), the beam intensity appears to have a "cloverleaf" appearance. This is an artifact of the polarization dependence of the coatings on the dichroic. Don't worry about it – the beam is actually quite clean. The intensity should still have symmetric intensity across the mirror planes, regardless of its shape. This problem is not seen with a silvered mirror beamsplitter.

2. Center beam position: monitor on CCD again. Assume beam is only too far left (perfectly centered in vertical axis). Using mirror M4 (Figure C-3), first move beam away from the optimal position, so that the beam intensity becomes uneven. You want to move it a maximum of one-half the defocused spot size. Then, center the beam up with mirror M5 (Figure C-3). The beam will have moved closer to the center

of the optical axis. Repeat as necessary until the axis is completely centered. Then, do the orthogonal optical axis.

3. Check the centering of the beam by focusing through the focus center. The beam position should remain perfectly centered and concentric. If not, the beam is tilted and step (2) should be repeated.

C.2 Output Optics

Figure C-3 and Figure C-5 show the important output optics for a confocal setup. This section will review the optics necessary for a confocal setup, in particular alignment of the confocal pinhole, choosing the right emission filters, and aligning an avalanche photodiode (APD).

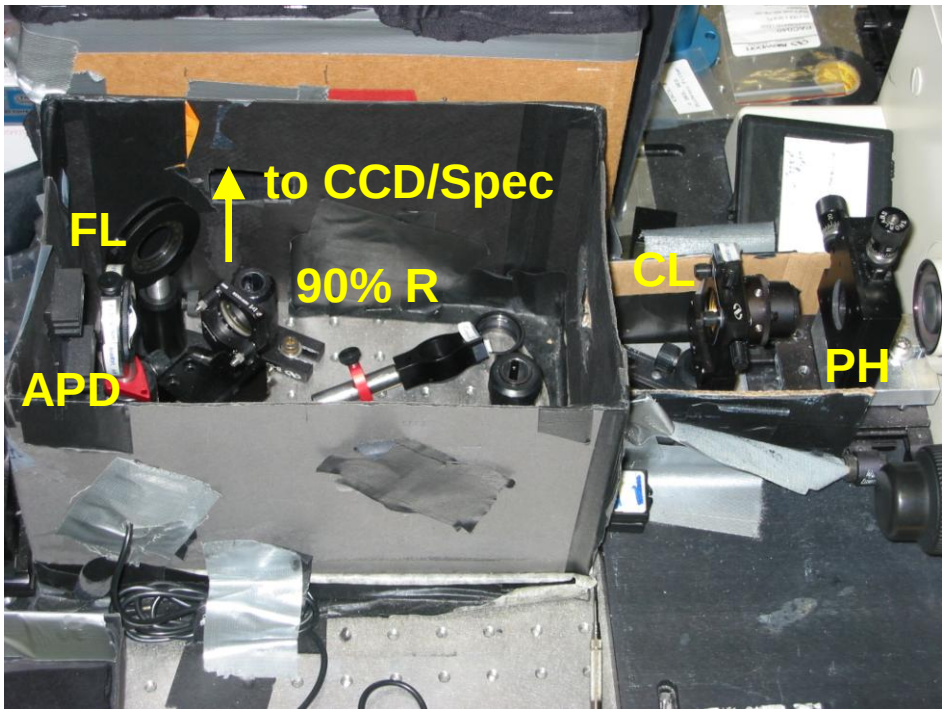

Figure C-5: Confocal microscope output optics. Note the pinhole (PH), placed at the microscope image plane, the collimating lens (CL), the 90% reflector (flips in and out), the focusing lens (FL) for the APD detector.

C.2.1 Confocal Pinhole

The diameter of the confocal pinhole (Pinhole in Figure C-3) determines the amount of z-confinement - a smaller pinhole rejects more background (i.e. scattering) but hurts signal transmission. Typically, a 75-100 μm pinhole is best, particularly in the infrared where spherical aberration and the long wavelength slightly enlarge the image spot.

Alignment of the confocal pinhole is the most critical aspect of confocal alignment. Since the microscope has a fixed tube length, the beam is converging just after the exit port of the microscope. If working in the infrared, it is best to align the pinhole to this beam using a visible laser (for instance, the 633nm HeNe on the setup) first. If the infrared is aligned to the same position as viewed on the Genwac camera, then the alignment will be close after the initial alignment with the visible laser. In order to align the beam initially, use an index card or power meter to measure the beam after the pinhole. Walk the X and Y axes of the pinhole until the power is maximized. The output should be very symmetrical and extremely sensitive to the focus of the objective lens. Make sure to check that you have found the real maximum (not a local maximum) by going well past the maximum signal position in each direction. The Z-position of the pinhole is not nearly as sensitive as the X and Y-positions, but should be adjusted to ensure that the light is maximized through the pinhole when the microscope beam is focused through the eyepiece (or on the

Genwac). This places the pinhole properly at the microscope image plane, which is formed by the microscope tube lens (inside microscope chassis).

C.2.2 Collimating the Emission Signal

Following the pinhole, there is a lens (f = 50.8 mm achromat) to re-collimate the beam. This lens is fairly simple to align and shouldn't need to be adjusted often.

C.2.3 Emission filters

Depending on the emission filters (usually bought from Omega Optical or Chroma Engineering), multiple long pass emission filters may be necessary to reject laser light at the proper frequency. The further the filter's turn on is red shifted from the laser, the fewer filters, perhaps only 1, are needed.

C.2.4 Aligning the Avalanche Photodiode (APD)

There is a lens (f = 50.8 mm achromat) that focuses the fluorescence signal onto the APD chip. The APD is mounted on an X/Y/Z stage to center the beam onto the chip (approximate size 200 μm X 200 μm). Align the beam by using back-reflected light from a glass coverslip. First, roughly align the APD stage (with the APD off!) such that the beam is close to the chip (cover up the chip with an index card to be safe). Again, if working in the IR, this is best to do with a visible laser that is closely aligned to the IR beam path, so that the IR does not have to be visualized. Once the alignment is close, switch to the IR source, attenuate the laser, turn on the APD and finish aligning. **(ATTENUATE THE LASER LIGHT, OD > 8). DO NOT ALLOW COUNTS ON APD TO EXCEED 10^6 s^{-1}!**

Both Perkin Elmer (PE) and MPD current produce APD's. The PE APD has better quantum efficiency (QE) in the infrared, but has poor timing resolution (instrument response function width = 500ps), than compared to the MPD PDM series APD (instrument response function width = 50ps). Currently a PE APD is installed on 8A back and, when properly shielded, it has approximately 200-300 dark counts/sec.

C.2.5 Spectrometer Path

This path is activated by flipping up a remote mirror. Currently there is a mirror mounted in this flipper, but a 90/10BS can be inserted, which sends 10% of the light to the APD (fast time resolution information) and 90% of the light to the spectrometer (slow spectral information. The next section is devoted to spectrometer alignment.

C.3 Alignment of CCD/Monochromator

C.3.1 Introduction

This section describes the proper alignment and optics used for the CCD/Spectrometer attachment, shown in Figure C-6. The monochromator is a Jarrell-Ash Monospec 18. This device is chosen because it is easy to use and has high throughput (50% is possible with certain gratings). This spectrometer sacrifices absolute resolution for transmission. There is also an Acton spectrometer available in the lab, which is not currently in use. This newer spectrometer is very similar to the Monospec 18, but since it is made by Acton, it is easier to use and computer controlled. Also, since Acton actively supports this spectrometer, new gratings can easily be purchased.

C.3.2 Input mirror

The first optic in the spectrometer beam path is a broadband reflective mirror (M1) , which is good for 400 – 1000 nm. It is mounted on a translation stage that enables translation of the beam across the input slit of the monochromator.

C.3.3 Focusing lens

The next component in the beam path is a f = 16 mm camera lens (FL in Figure C-6), which is used because it is highly color-corrected. This focuses the beam through the entrance slit of the monochromator. The focal length of this lens is matched to perfectly fill the grating of the monochromator. This can be observed by sending a visible laser through the system and placing an index card on the grating mount (be careful to avoid contact with the grating, which is extremely fragile). The beam should be round, have a Gaussian profile, and centered on the grating, filling the entire active area.

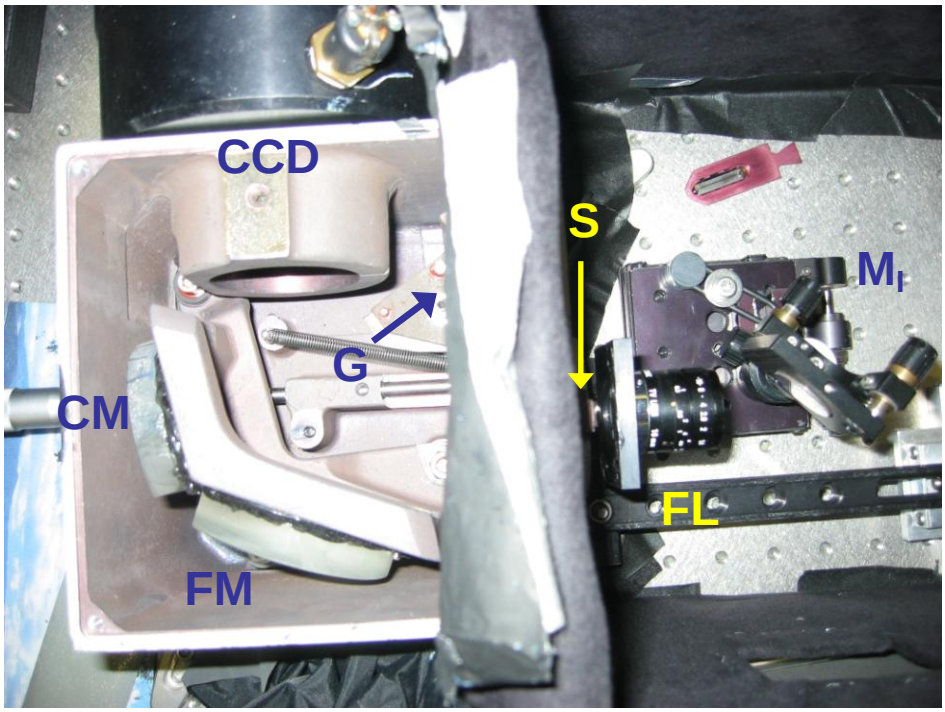

Figure C-6: Optics in the CCD/Spectrometer assembly. Note the input mirror (M_I), mounted on a translation stage, the focusing camera lens (FL), the entrance slit (S), the collimating concave mirror (CM), the grating (G), focusing concave mirror (FM) and the CCD camera, located at the exit focal plane of the monochromator.

C.3.4 Entrance slit

A 150 μm slit (S in Figure C-6) is used (aligned vertically) on the input to the spectrometer. For initial alignment, remove this slit and have the beam properly fill the grating (see above). Then add the slit and re-align to achieve the same condition. Measure the power through the slit (ideally, > 95% transmission is possible).

C.3.5 Concave mirror

This is a collimating mirror (CM in Figure C-6) and directs a collimated beam onto the grating.

C.3.6 Grating

The grating (G in Figure C-6) is the dispersive element of the monochromator. The grating is mounted (with 5 minute epoxy) onto a mounting bracket. This is a kinematic mount that can be adjusted so that the dispersed beam hits the center of the CCD camera (vertical adjustment). Further, two specs are important for the grating: the blaze (the peak operating wavelength) and the groove spacing (more grooves disperse light more quickly). This is a ruled grating, and replacements may still be vailable from Genesis Labs (1-970-241-0889). To ensure optimal throughput, it is important to operate near the blaze wavelength (the general rule is to work between 2/3 and 3/2 of the blaze wavelength). The number of grooved rulings describes a tradeoff between resolution and the spectral range provided on the detector. Using the LN-cooled Princeton Instruments camera (512 pixels, pixel ~ 18 μm) the following is observed:

Pitch	Blaze	Typical Spectral range	Approx. Resolution	Used for
150 grv / mm	500 nm	400 – 1000 nm (600 nm)	4 nm	scattering
300	400	500 – 800 nm (300 nm)	2	fluorescence
600	1000	850 – 1000 nm (150 nm)	1	Raman

Table 1: These are the gratings currently available for the Monospec18 spectrometer. The higher the pitch, the better the resolution and the smaller wavelength range available in the spectrum.

It is important to exercise great care when handling gratings! If they are scratched or dirty, they CANNOT be cleaned or touched in any way. Keep them in their protective case!

C.3.7 Focusing Concave Mirror

This mirror (FM in Figure C-6) focuses the collimated beam at the exit port of the monochromator.

C.3.8 Exit port

Instead of a slit, a CCD detector chip is placed here to create a real-time image of all spectral lines simultaneously. The WinSpec software sums all vertical pixels into a single pixel value, making an array with 512 pixel values, calibrated by using an appropriate pen lamp source (e.g. Hg, Xe) and laser sources. The CCD camera has a housing that slides back and forth in this mounting and is held in place with a set screw. You must minimize the width of the calibration lines on the camera by changing the focal position and you should make the lines as symmetrical as possible by rotating the camera to properly align the input slit and the pixel array axes. Any C-mount camera can be attached to the exit port by using the black C-mount adapter that I machined (located in Rm 8a). Popular calibration lines are given here:

Hg lamp (visible)	Xe lamp (IR)
404.66 nm	823.2 nm
435.84	828.0
546.1	840.9
577.0	881.9
579.0	895.2

C.3.9 Camera

CCD cameras vary widely in their performance. Currently, a liquid nitrogen cooled slow-scan camera is used. This camera is cooled to -120 ºC by filling with

liquid nitrogen in order to minimize dark counts. **During cool down of this camera, ensure that the software controlling the camera, Winspec, is running, the shutter to the camera is closed, and the camera is actively collecting data**. This ensures that the camera is not damaged during cooling. The read-out time of this camera is slow compared to the cameras for wide-field imagine in the lab, requiring 0.37 sec. / frame. While other cameras are faster, and can be used, they tend to have higher dark counts. Be careful when using CCDs with high gains, making sure that the gain is linear across the spectral range used (this is especially problematic in scattering experiments covering a large spectral range).

C.3.10 Final alignment

With the CCD camera attached, use the back-reflected laser beam **(attenuated to safe levels for the detector!!!)** to maximize signal on the camera. You may have to remove the slit to see maximum signal levels, and then put the slit back in and realign, adjusting: (i) the input mirror angle and position, (ii) the focusing camera lens, (iii) camera angle and focal position, (iv) grating angle to image the desired spectral range, (v) grating mounting bracket vertical adjustment should be adjusted to ensure that the beam is focused on the center of the CCD chip.

C.3.11 Final comments

The alignment of the CCD/spectrometer system is clearly the most arduous task in this setup. However, once adjusted, this path should only require re-alignment upon changing the grating or substantially altering the laser wavelength. The only

adjustment that should be done regularly is calibrating the X-axis of the spectrometer readout using the pen-lamp, a task that takes just minutes.

C.4 Software

C.4.1 Introduction

There are 2 programs on 2 separate computers that are needed to acquire confocal images using the Topometrix microscope. First, a LabVIEW program is run on computer WEM16, which integrates the number of counts from the APD into 10ms (or longer) bin times. This computer then sends out an analog signal proportional to the number of counts measured to the AFM controller. The AFM controller, which controls stage movement, is run by WEM12. This computer uses the Topometrix software to move the stage and build up images from the APD counts that WEM16 collects and processes in real-time.

C.4.2 Using Bin APD counts LabVIEW Program

A relatively simple LabVIEW program, "Bin APD Counts.vi" was written using LabVIEW version 8.6 on WEM16. LabVIEW is notorious for having poor compatibility between different versions of its software, so avoid updates to LabVIEW on this computer. This program is not very complicated, however, and can be fairly easily be rewritten in a new version, especially by a user familiar with LabVIEW. To run this program on WEM16, simply click on the "Bin APD Counts.vi" file located on the desktop or here: C:\Users Backed Up\Anika\Labview programs\Bin APD photons.vi. This program is commented in the Labview file, so this section is just devoted to use of the code. A screen capture of the front panel of the program is seen

in Figure C-7. Note that when using LabVIEW, the program can be altered, so avoid adding or deleting any of the options on the front panel unless you save a backup copy and have experience with LabVIEW programming.

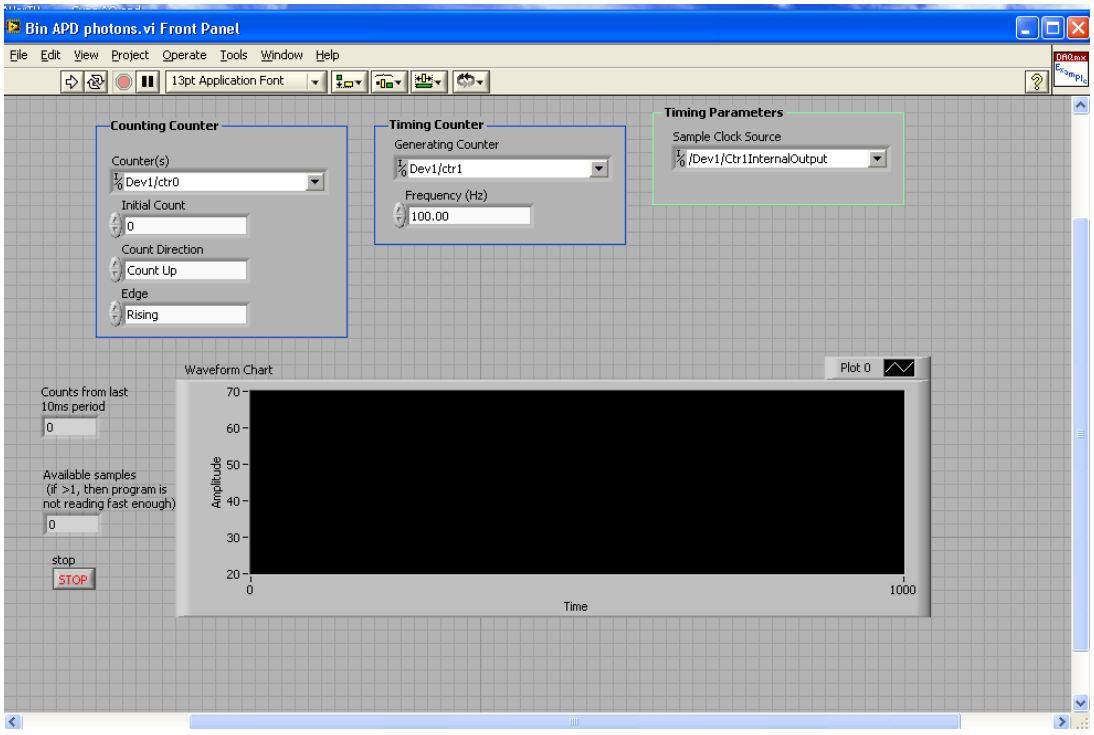

Figure C-7: Screen capture of Bin APD photons program front panel.

In order to run the program, simply click on the white arrow located at the top of the program – just as any LabVIEW program starts. The program will begin drawing out a time trace that corresponds to the number of counts per bin time. Depending on what other processes are running on the computer, this program may run slowly. To check whether the program is running slowly, watch the "Available samples" output number. If this number is zero, then the computer is reading the

output from the counters as quickly as they are being generated, but if this is a non-zero value, then the computer is not updating fast enough. Avoid using this computer for other tasks while collecting data and this program will work well.

The most important input to this program is the Frequency (Hz) input. The user can choose any bin time desired using this input. In Figure C-7, it is currently set for 100Hz, which corresponds to 10ms bin times and is the fastest this computer can handle reliably. The program then takes the number of photons for a specific time interval and divides by 100. This number is then converted into an analog voltage that is sent to the AFM controller in order to build up an image. Note that when the image is formed by the AFM software, it will plot the voltages it receives, which are a factor of 100 smaller than the actual number of photons collected by the APD. Since +10 V is the greatest voltage that can be sent, the user should ensure that the number of photons does not exceed a value that will produce a >10V signal. Any value 10V will just be plotted at +10 V. When using an APD and 10ms bin times, this limits the photon rate to 1,000 photons/10ms or 100,000 photons/s, which is a good limit to keep in mind anyway, since significantly more photons than this will damage the APD.

There are two ways to stop the program. By pushing the red stop sign, located near the white arrow at the top of the page, the program stops and no data is recorded – this is useful for aligning, taking confocal scans, or anytime that the time trace does not need to be kept. Alternately, there is a red "STOP" button located towards the lower left corner of the screen. If this button is pressed, the program stops and asks where to save the acquired time trace.

C.4.3 Topometrix Software for Confocal Scanning

The previous section described collecting data from the APD, but now the user still needs to create a confocal scan, which is achieved using the Topometrix AFM head program. This program is opened from the desktop of WEM12 and is called "SPMLab602". When this program is opened, click the AFM tip button that is set off from the other buttons in the top right corner of the screen. This will open a dialog box that allows you to choose a stage. For confocal scanning, the stage (not the AFM tip) should be scanned, so select scanner LX149707 and press "ok". The computer will ask if you want to energize high voltage for the 50μm Tripod scanner, so press "Engage". Now the stage is active – remember the stage is VERY delicate. **Do NOT press down on the stage with any force or you will easily damage it!** The program is now open and setup for AFM scanning, but different settings are needed for confocal scanning. Go to Setup → Acquire. Make sure that the "Fwd" and "Rev" checkboxes are only clicked for IN1 – this is where the analog signal from the LabVIEW program is sent. Since this is an AFM program, it will scan every line in the forward and reverse direction. This is a useful feature for AFM scanning because you need that information to judge if a feature is real, but it is not necessary for confocal scanning. Unfortunately, there is not a way around it, so the user will just have two images of the same object at the end of the scan.

Now the program is set to collect data from WEM16. Press the button with 3 yellow arrows to start a scan. Of course, the LabVIEW program "Bin APD photons.vi" needs to be running and collecting data, otherwise the Topometrix program will just plot 0 for the entire image. The scan range, scan rate, and resolution

should all be set to acquire data at the rate the LabVIEW program is binning it. That means, if the LabVIEW program has 10ms bins, the Topometrix program settings should yield 10 ms/pixel. One set of conditions for a 10 ms bin time is: Scan Range = 20 μm, Scan Rate = 20 μm, Resolution = 100, which yields 10 ms bin times and 200 nm x 200 nm pixels. These settings could be altered to yield a 100nm pixel size by doubling the resolution and halving the Scan Rate.

Images are saved into a format specific to the Topometrix program, but this program should not be used for data analysis because it tends to crash. Export the files to .txt format and import them into Matlab for analysis.

C.5 Scanning stages

C.5.1 Piezoelectric Scanner

There are two stages for the Topometrix AFM system: the tripod (sample) scanner and the tip scanner (only used for AFM). Typically, the sample is scanned, though the tip can be scanned as well for AFM only operation. You CANNOT scan both at the same time. This would require a second controller box (an option if careful tip positioning is needed; the ECU+ controller). The tripod scanner is known as LX149707 (tripod scanner, 50 μm range) and the tip scanner is referenced in the software as X089704 (Accurex scanner, 100 μm range). There are dozens of other scanner files in the Veeco SPM Lab 6.02 software, but only these are used. However, you can control other stages with this controller if you want (i.e. the PI closed loop stage has a driver file); this is just a note for future experiments.

Both of these scanners are closed-loop piezo stages, meaning that the piezos are completely linear in their movement, and that you can return to a known position (clicking around on the screen). This is done by a capacitive sensor that reads out the extension of the piezo stack. A servo loop in the controller monitors this and adjusts the voltage to the piezo (between 0 – 100 V) to achieve the desired position. You need to calibrate these sensors and make sure they are linearized using software control. The stage has been linearized by previous users and the stage files are saved in the following directory: c:\programfiles\Veeco\SPMLab6.02\scanners.

Another important file is c:\programfiles\Veeco\SPMLab6.02\stages.ini. It must refer to the stages that you intend to use. Because this version software is much newer than the Lumina scanner system that we have, you need to make sure that it knows what the Lumina is (and its two scanners, the tripod and the tip scanner). This file is backed up on floppy disk as well as saved on 2 computers:

WEM01\Users\Anika\Backups\Very Important Software\WEM 12\VEECO\SPML602

WEM16\Users Backed Up\Anika\ Very Important Software\WEM 12\VEECO\SPML602

The computer running the topometrix software has had its hard drive crash at least twice. Check the hanging file for information about installing software onto a new hard drive should the current hard drive fail.

C.5.2 Calibration and linearization of stages

Occasionally, it is important to ensure that the stage is appropriately linearized. You need to minimize the cross-talk between the X- and Y- axes in the stage file, and

this should be checked for each scan range that you intend to use. I typically do the 50 μm, 20 μm, 10 μm, and 5 μm files. If you scan smaller, the amount of non-linearity is difficult to see, anyway.

The Topometrix instruction book gives a great walk-through on this process, in p. 7-2 through 7-18. I will not repeat them here, except to say that it's important to set up the grating that you scan in AFM mode quite square with respect to X and Y, else there will be a lot of cross-talk. Finally, make sure to note which stage files are changed (discussed in the instructions). Before doing any recalibration, it is important to save a copy of the stage calibration file in a safe spot so that if you need to go back to it, you can.

C.5.3 Hardware signals in/out of ECU+ controller

The AFM and NSOM signals go from the head unit through a thick multi-pin cable and plug into a PC board that is mounted on the optical table. This board then goes out to the respective inputs in the ECU+ controller. The two APD channels are brought in through IN 1 and IN2, respectively. These inputs are whatever you want, provided they are voltages (-10 to 10 V range). To get the APD signals (TTL or NIM pulses), you must bring these pulses into a NI board that serves as an integrator (i.e. how many pulses do you see within a 10 ms time). The architecture of the controller unit is quite open and fairly intuitive; it's simple to get signals in/out of this box.

References

1. Fromm, D. Improving the Size Mismatch Between Light and Single Molecules using Metallic Nanostructures. *Stanford Ph. D. Thesis* (2005).